Development of a Solid Content Sensor Based on Low-level X-ray Sources

by

Bo Yu

A thesis submitted in partial fulfillment of the requirements for the degree of

Master of Science

in
Photonics and Plasmas

Department of Electrical and Computer Engineering
University of Alberta

Abstract

The focus of this thesis is to develop a solid content sensor based on low-level X-ray sources to monitor the settling process of FFT (Fluid fine tailings) in oil sands tailings ponds and provide calibration data for a light scattering sensor built for the same purpose.

In this study, high-resolution spectrometry based on a CdTe (Cadmium Telluride) detector was used to measure the X-ray attenuation by FFT samples with solid content at different wt% (weight percent). Two experiment setups were designed for a 0.9 μCi ^{241}Am and a 1 μCi ^{133}Ba source. Based on the considerations of measurement performance and licensing regulations, the 1 μCi ^{133}Ba source was finally selected for further development, and the monitoring parameter was based on the intensity ratio of 31 keV and 81 keV peak.

Mass attenuation calculations were used to verify the experimental results. Comparison of the calculated and measured X-ray / gamma (γ) ray transmission results shows the experimental results are between the upper and lower limits formed by photoelectric absorption and total attenuation cross-sections. GEANT4, a Monte Carlo based simulation code, which calculates the transmission of radiation through matter, was used to simulate the results of this study. The experimental results and simulated results are in good agreement. The effect of measurement error of FFT chemical composition, measured via ICP-MS (Inductively Coupled Plasma Mass Spectrometry), was evaluated to be within ± 2 wt% in solid content. This simulation predicted transmission results within several percent by considering all the geometry factors of the real setup. The transmission is sensitive to chemical composition which should be determined by ICP-MS composition analysis for accurate predictions.

An inexpensive detection system based on Lutetium-yttrium oxyorthosilicate (LYSO) fluorescent crystals and Multi-pixel photon counters (MPPC) was developed and characterized with the 1 μCi ^{133}Ba. It was found that such an inexpensive detector system can work effectively and should offer a viable technique for carrying out solid content analysis of settling ponds in the field.

Preface

The experiment setup, method, and data of the 0.9 μCi ^{241}Am source were published as B. Yu, W. Wang, F. Goncalves, P. Dhandharia, A. Sedgwick, A. Junaid, M. Gupta, R. Fedosejevs and Y.Y. Tsui, "Measuring Solid Content in Fluid Fine Tailings (FFT) Using a Low-Level X-ray Radiation Source", in International Oil Sands Tailings Conference 2018, Edmonton, Alberta. I was responsible for the experiment setup design, data collection and analysis. W.Wang assisted with measuring the sample density shown in this thesis, and also built the original version of the GEANT4 code for ^{241}Am. P. Dhandharia applied the pH adjusting method for mitigating the settling of NRCAN kaolin and carried out the observation for 2.5 wt% NRCAN kaolin shown in Chapter 2. R. Fedosejevs assisted with the experiment setup design, and was involved in the conception of the project as were supervisors with Y.Y. Tsui and M.Gupta. All authors contributed to manuscript editing. Canadian Center for Isotopic The ICP-MS measurements for all the samples were carried out by the Earth Sciences Facility at the University of Alberta. In Chapter 6, the LYSO detector was built and tested by Talwinder Kaur Sraw. I was responsible for building the ADC circuit and collecting the data shown in this thesis. The conception of this detector was proposed by R. Fedosejevs. Additional experiments, calculations, and simulation results, and analysis are my original work.

Acknowledgements

First and foremost, I appreciate Professor Dr. Tsui and Professor Dr. Fedosejevs for offering me the opportunity to study in University of Alberta and join this project. I have gained lots of valuable knowledge and practice on photonics and oil sands industry. Thanks to Professor Dr.Gupta, she is always passionate to offer me suggestions and instructions. I also treasure the help from my lab mates: Wei Wang, Dr. Talwinder Kaur Sraw, Dr. Priyesh Dhandharia, Yu Wan, Dr. Tulika Srivastava, Andrew Longman, Ruoheng Zhang, Yilong Feng, and Jiangwen Zhang.

Thank you to Dr. Junaid and Andrea for providing the samples, and sharing ideas and techniques in this project.

Most components in experiment setup were built by the ECE machine shop. Thank you to Reiner Schwarze and other machinists for your patience and outstanding skills.

Thank you to Dr. Guangcheng Chen in Earth and Atmospheric Sciences Dept. for the accurate ICP-MS measurements on the chemical compositions of the samples and patience for explaining the principles of this technique.

Thanks to Dr. Xiaoli Tan, Lisa Brandt, Brittany Mackinnon in Institute for Oil Sands Innovation (IOSI) lab for the access and trainings to use all the equipment for sample characterizations.

Finally, I would like to thank all my family and friends, especially my girlfriend, Yixue Jiao, for their love and support, standing by me at all the difficult moments and applauding for me when I earn an achievement.

Financial support of this work was provided by the Natural Sciences and Engineering Research Council of Canada, the Institute of Oil Sands Innovation, and the Canada's Oil Sands Innovation Alliance.

Contents

List of Tables

List of Figures

List of Abbreviations

FFT: Fluid fine tailings

ICP-MS: Inductively coupled plasma mass spectrometry

wt%: Weight percent

IAEA: International Atomic Energy Agency

NIST: National Institute of Standards and Technology

BGO: Bismuth germanate

LYSO: Lutetium-yttrium oxyorthosilicate

HPGe: High purity germanium

CdTe: Cadmium telluride

CNRL: Canadian Natural Resources Limited

MPPC: Multi-pixel photon counter

ADC: Analog-to-digital converter

TTL: Transistor-transistor logic

PCB： Printed circuit board

1. Introduction

Alberta's oil sands has the third largest oil reserves in the world, after Venezuela and Saudi Arabia [1], accounting for 9.6% of global proven reserves [2]. It is estimated that the total in place bitumen reserves are over 1.7 trillion barrels [3], of which approximately 165 billion barrels can be recovered using existing technology [1].

Oil sands mining has recently been a pillar of Canadian economy, but some environmental challenges also arise in this industry. One of them is tailings produced after aqueous extraction of bitumen. The inventory of oil sands tailings is fairly large and keeps increasing. By the end of 2013, the total amount of fluid fine tailings (FFT) stored in the tailings ponds in Canada is about 975.6 Mm^3 and the tailings ponds water covers a total area of approximately 88 km^2. [1] The government has taken measures to mitigate the impact of oil sands tailings on the environment. Government regulations, such as the Alberta Energy Regulator's Directive 085 outlines the requirements for tailings pond closure [4]. The weight percent (wt%) of solid content, as an alternative to bulk density used by industry is a key parameter representing the settling state of the FFT, and the success of consolidation [5].

The common techniques used to determine the solid content wt% in FFT include gravimetric determination [6], Dean Stark [7][8], and toluene washing [9]. The procedures of gravimetric determination are very complicated and require operators with good chemical background and experiment skills. The labor expense is high, and efficiency is low. Dean Stark and cold wash are time-consuming and generate waste that contains organic solvent and bitumen. These laboratory techniques all rely on samples manually collected at various tailings pond depths, which is onerous, not real time and easily affected by sampling errors.

X-ray and gamma (γ) ray attenuation have been widely used for measuring physical properties of soils and building materials such as attenuation coefficient, density, moisture, and porosity in the last decades [10]-[20]. This technique has also been applied in identifying the regime of two-phase flow in pipelines [21][22]. Most of these applications rely on high intensity sources, which are expensive and potentially harmful. The cost of permit and supervision are very high. Due to safety and expense concerns,

they are not suitable for tailings ponds applications that require several sources at different depths. However, with proper sample thickness and measurement time, comparable performance can also be achieved by using low-level X-ray sources, and the cost and risk can be much lower.

This project is focused on developing an inexpensive, efficient, and dependable solid content sensor to monitor the settling of fluid fine tailings in oil sands tailings ponds based on low-level X-ray sources. This solid content detector will also provide data calibration for another detection system based on light scattering. The solid content detector will be calibrated with necessary data measured in the laboratory before it is implemented. Once installed in the tailings pond, it requires little maintenance. The following chapter introduces the theory of X-ray attenuation, sources, monitoring parameters, detection system, and data processing method. Chapter 3 gives the detailed geometry of the experiment setup, preliminary tests, and the experimental results. Chapter 4 introduces two modeling methods, mass attenuation calculation and GEANT4 simulation. Chapter 5 focusses on the comparison between the experimental and simulated results. Chapter 6 shows the performance of a homemade inexpensive detection system in a big settling tank. Chapter 7 gives a summary of the current research and devices developed, and proposes future directions.

2. Background and Methods

2.1 Beer-Lambert Law

The attenuation of X-rays / γ-rays passing through an absorber can be calculated using the Beer-Lambert law as shown in Equation 2-1:

$$I=I_0\exp(-\mu_m\rho x) \quad \textbf{(Equation 2-1)}$$

where I_0 is the incident intensity of X-rays / γ-rays, I is the transmitted intensity after attenuation by a material of thickness x(cm), ρ is the mass density and μ_m ($cm^2 \cdot g^{-1}$) is the mass attenuation coefficient of the absorber at the energy of the incident photons. The variation of the solid content wt% and density of the oil sands tailings will lead to a variation of the mass attenuation coefficients, which will be reflected by the change of transmission of X-rays / γ-rays.

2.2 General Design of Experiment Setup

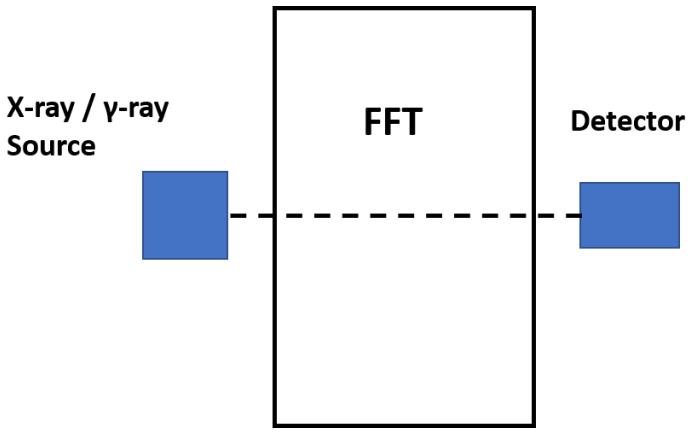

Figure 2-1 – Schematic of the general design of experiment setup

The general design of the experimental setup is shown in Figure 2-1. The source and the detector are placed at opposite sides of an FFT container. The intensity of transmitted X-rays / γ-rays decreases as the solid content in the FFT increases. The source, detector, and dimensions of FFT container were studied in this thesis. Two experiment setups were built according to the general design, and they will be described in Chapter 3.

2.3 X-ray and Gamma Ray Sources

A radioactive isotope is an unstable atom that has excess nuclear energy. Some of the excess energy can be emitted as gamma rays from the nucleus, as it releases or captures an electron, or it releases an alpha or beta particle. These are some of the decay processes of the radionuclide.[23]

X-rays are generated by the creation of inner shell vacancies and the subsequent rearrangement of the atomic shells. The vacancies are produced by orbital electron capture by the nucleus and internal conversion. [24] Gamma rays are emitted by an excited nucleus when it passes to a lower energy state. The excited nucleus is usually formed in the processes of alpha or beta decay. [25] In this thesis, sources that emit both X-rays and gamma rays are called "X-ray sources". Sources that only emit gamma rays are called "gamma ray sources".

Nuclide	Half-life (Day)	Possible Energy	Emission Probability
27-Co-60	1925.23	1173.228	0.9985
		1332.492	0.999826
55-Cs-137	1.099×10^4	661.657	0.8499
56-Ba-133	3848.7	30.625	0.340
		30.973	0.628
		80.9979	0.329
		356.0129	0.6205
63-Eu-152	4941	39.5229	0.208
		40.1186	0.377
		121.7817	0.2841
95-Am-241	1.5785×10^5	13.90	0.1303
		17.81	0.1886
		20.82	0.0481
		59.5	0.3578
95-Am-243	2.692×10^6	13.761–13.946	0.0705
		16.109–17.992	0.0818
		74.66	0.672

Table 2-1 – Half-life, emission energy and probability of nuclides that are possibly suitable for solid content detector development

The ideal source for this application should have two peaks. The peak with lower energy provides high sensitivity to the variation of the solid content in measured tailings. Another peak with higher energy should not be attenuated much and serves as a monitor of the strength of the radiation source. The monitoring parameter can be defined as the intensity ratio of the two peaks. The initial ratio of the two peaks will not change even if

the strength of the source decreases as time goes by due to the decay of the nuclides. However, the decrease of the strength reduces the counting rate of the detector and decreases the measurement accuracy. The half-life of the nuclides should be as long as possible because the detection system is designed to work for several years without replacement once implemented in the tailings pond. The radiation source should be able to provide enough emission of X-rays / γ-rays during the whole life of this instrumentation. Several radiation sources with half-life longer than 3 years were selected for comparison according to the data from IAEA [26], as shown in Table 2-1. The ^{60}Co and ^{137}Cs are gamma sources widely used in industry, but they only have one or two high energy gamma peaks with high emission probability, which are not sensitive to the variation of the solid content in the slow-settling tailings. The ^{133}Ba, ^{152}Eu, ^{241}Am and ^{243}Am all have a lower energy peak and a higher energy peak. The energy values of ^{241}Am lower peaks are quite similar to those of ^{243}Am, and the ^{241}Am source is much easier to be obtained since it is the radiation source used in smoke detectors. Compared with peaks of ^{152}Eu around 40 keV, ^{133}Ba has a characteristic peak around 31 keV with much higher emission probability. ^{241}Am has a half-life around 432 years, and that of ^{133}Ba is 10.54 years, which are both satisfactory. After these considerations, an ^{241}Am source from a smoke detector and a commercial 1 μCi ^{133}Ba were used for experiment.

2.3.1 ^{241}Am and ^{133}Ba Sources

The ^{241}Am source was detached from a smoke detector. This radiation material is wrapped with a back shield but without a collimator. From the manufacturer's label, the strength of the source is 0.9 μCi, but this value needs to be further verified. In this thesis, it will be named as " 0.9 μCi ^{241}Am source " for convenience. A 10 μCi ^{241}Am commercial source (Stuart Hunt & Associates, Ltd.) was bought to verify the performance of the 0.9 μCi ^{241}Am source. The radiation material is sealed in a Ø 1 mm spot at the center of a small acrylic glass sheet, and the dimension of this sheet is 23.5 mm ×11 mm × 2 mm. The radiation material of the 1 μCi ^{133}Ba commercial source (Spectrum techniques, LLC.) was pipetted within a Ø 0.25" well in a Ø 1" plastic disk. The size of the finally pipetted area is unknown and varies in shape and volume due to manufacture factors.

Source holders were designed and built for these three sources to fix the positions and adjust the geometry in experiment. The drawings are shown in Appendix B. The spectra measured with only air between the source and the detector using these 3 sources are shown in Figure 2-2 (a), (b) and (c).

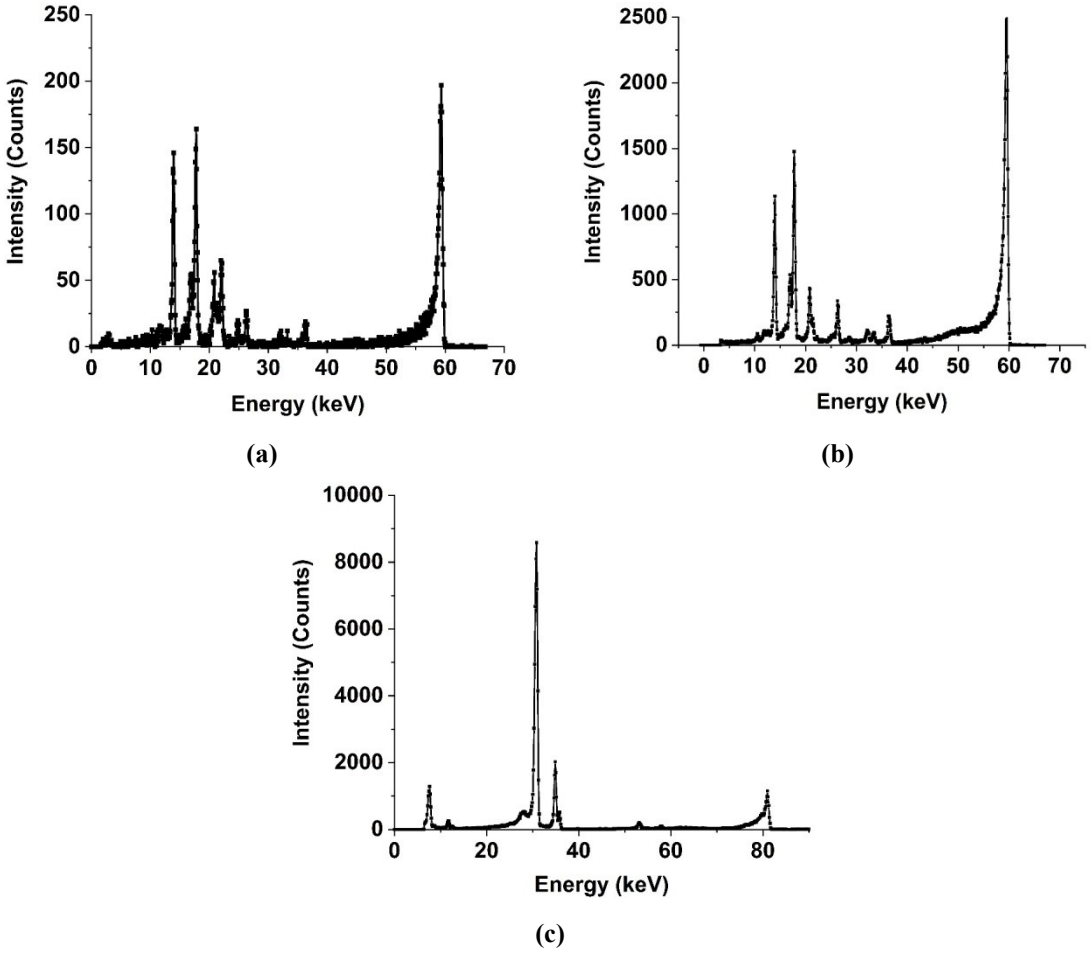

Figure 2-2 – Measured spectra using a CdTe detector (a) 0.9 µCi ^{241}Am source emission spectrum; (b) 10 µCi ^{241}Am source emission spectrum; (c) 1 µCi ^{133}Ba source emission spectrum (< 100 keV); (The distance between the detector element surface and the center of the ^{241}Am sources is 28.8 mm; for the 1 µCi ^{133}Ba source, this distance is 15 mm)

The radiation energy and emission probability of the X-rays and gamma rays from two sources are also listed in Tables 2-2 to 2-5. These data were obtained from IAEA [26], which were used for energy calibration and calculations shown in the following chapters in this thesis. It is seen from Figure 2-2 (a) and Table 2-2 that the 17.8 keV photon energy has the highest emission probability among the X-rays of ^{241}Am in the low energy range. The 13.9 keV photon energy could be more sensitive to the variation of solid content due to its lower energy though the emission probability is lower than that at 17.8 keV. A

comparison was done for the X-rays of ^{241}Am to determine the lower energy peak in the intensity ratio and the results will be shown in Chapter 3. The 59.5 keV gamma ray peak, a byproduct of alpha decay of ^{241}Am [27], has the highest emission probability and energy among all the peaks of ^{241}Am, which is the most suitable peak to be the reference signal for the intensity ratio. The intensity ratio of 17.8 keV and 59.5 keV peaks was selected for preliminary tests of ^{241}Am. For ^{133}Ba X-rays, the peak formed by 30.625 keV and 30.973 keV photon energies has the highest emission probability, and no other suitable peaks are in the low energy range. Thus, the peaks around 31 keV can be selected as the lower energy peak. These two peaks can be regarded as one peak since they are close to each other. According to the emission probability shown in Table 2-3**,** the energy of X-ray photons was calculated to be 30.85 keV using an approximation shown as Equation 2-2. The approximate value was used in calculations and simulations to define the energy of the X-rays. This peak will be mentioned as 31 keV peak in the additional sections of this thesis for convenience.

$$30.625*0.34/(0.34+0.628) + 30.973*0.628/(0.34+0.628) \approx 30.85 \text{ keV} \qquad \textbf{(2-2)}$$

For ^{133}Ba, the peak with the similar role to 59.5 keV of ^{241}Am is 81 keV, which is a byproduct of electron capture of ^{133}Ba [28]. The energy is not too high, and the emission probability is close to that of 59.5 keV of ^{241}Am. Thus, the intensity ratio of 31 keV and 81 keV peaks was determined to be the monitoring parameter for ^{133}Ba.

Nuclide	**Origin**		**Energy (keV)**		**Emission probability per decay**	
			E_x	**Uncertainty**	P_x	**Uncertainty**
95-Am-241	N_P	Ll	11.89	±0.02	0.00848	±0.00010
		Kα	13.90	±0.02	0.1303	±0.0010
		Kβ_η	17.81	±0.02	0.1886	±0.0015
		$K\gamma$	20.82	±0.02	0.0481	±0.0004

Table 2-2 – X-rays from ^{241}Am

Nuclide	**Origin**		**Energy (keV)**		**Emission probability per decay**	
			E_x	**Uncertainty**	P_x	**Uncertainty**
56-Ba-133	Cs	L	3.80-5.70	N/A	0.160	±0.008
		Kα_2	30.625		0.340	±0.004
		Kα_1	30.973		0.628	±0.007
		$K\beta_1'$	34.92-35.26		0.182	±0.002
		$K\beta_2'$	35.82-35.97		0.046	±0.001

Table 2-3 – X-rays from ^{133}Ba

Nuclide	Energy (keV)		Emission probability per decay	
	E_x	Uncertainty	P_x	Uncertainty
95-Am-241	26.3446	±0.0002	0.0240	±0.0003
	33.1963	±0.0003	0.00121	±0.00003
	59.5409	±0.0001	0.3578	±0.0009

Table 2-4 – Gamma rays from ^{241}Am

Nuclide	Energy (keV)		Emission probability per decay	
	E_x	Uncertainty	P_x	Uncertainty
56-Ba-133	53.1622	±0.0006	0.0214	±0.0003
	79.6142	±0.0012	0.0265	±0.0005
	80.9979	±0.0011	0.329	±0.003
	276.3989	±0.0012	0.0716	±0.0005
	302.8508	±0.0005	0.1834	±0.0013
	356.0129	±0.0007	0.6205	±0.0019
	383.8485	±0.0012	0.0894	±0.0006

Table 2-5 – Gamma rays from ^{133}Ba

2.4 Detector

Many kinds of detectors can be used for X-ray and gamma ray detection. There are semi-conductor detectors such as HPGe, Si and CdTe, and scintillators such as NaI (TI), BGO, and LYSO. The semi-conductors have good efficiency and high energy resolution, but they produce very small output signals. A preamplifier with good shielding is required to generate pulses with little noise. To further reduce the thermal generation of charge carriers, a cooling system is also necessary.[29] The scintillators provide much lower detection efficiency and worse resolution compared with semi-conductors, but they require a much simpler pulse shaping circuit. A multi-pixel photon counter [30] can work with the scintillator to generate pulses. The pulses can be amplified directly by a pulse shaper with wide band and low impedance. [31] The main purpose of this thesis is to gain more scientific understanding on X-ray attenuation technique for solid density measurement, optimize the experimental parameters and verify the experimental results using simulation, which requires spectra with high accuracy and resolution. The measurement errors caused by the instrument should be assessed and minimized. The data should be consistent and repeatable. In this case, most of the characterization work presented in this thesis was done by using the XR-100T CdTe detector from Amptek. An inexpensive LYSO detection system was also developed for future implementation in

tailings ponds. The results obtained by using this detection system are shown in Chapter 6, which will be introduced later.

The CdTe detector is XR-100T from Amptek, Inc. The detection area of this detector is 3mm × 3mm. The thickness is 1 mm. It has very good detection efficiency in the energy range focused by this study. As shown in Table 2-6 [32], for 17.8 keV, 31 keV, and 59.5 keV the detection efficiency is nearly 100%. For 81keV, it still has 80.9% photoelectrical absorption, and the scattering effect is only 2.7 %. However, from the spectra measured by this detector, it was seen that 59.5 keV and 81 keV were not in symmetrical Gaussian shape but a Gaussian shape with a long tail sloping down to the low energy area below the peak. This phenomenon is called “hole tailing effect”, which is caused by charge trapping. The thermal equilibrium in a semiconductor is disturbed when excess charge is generated. The recombination of free charges occurring at trapping sites leads to a new equilibrium. The lifetimes for free charges in Si and Ge are several millisecond long since there are few trapping sites. The lifetime is much longer than the transit time, so the trapped charges in the charge collection process is negligible. However, compound semiconductors such as CdTe have more trapping sites than Si and Ge, which leads to a much shorter lifetime of free charges and reduces the charge collection efficiency. The tail below the energy of the main peak is formed by the pulses with low charge collection efficiency. The charge collection efficiency can be deduced from the risetime of the pulse. The maximum pulse heights are most probable seen at the shortest risetimes. With increasing risetime, the pulse height decreases and the probability decreases. [33] A built-in function of amplifiers used to reject pulses with low charge collection efficiency according to the risetime will be introduced in the following section.

Energy (keV)	Total Interaction	Photoelectric Interaction
12	97.79%	97.79%
15	98.57%	98.57%
20	98.95%	98.95%
25	98.95%	98.95%
26.711	99.09%	99.09%
30	99.16%	99.16%
31.814	99.16%	99.16%
35	99.16%	99.16%
55	98.63%	98.46%
60	97.47%	97.03%
80	83.60%	80.90%

90	73.55%	69.54%
100	63.55%	58.64%
125	44.02%	37.23%
150	30.85%	24.13%
600	4.84%	0.64%
800	4.00%	0.33%
1000	3.49%	0.21%
1022	3.45%	0.20%
1250	3.08%	0.13%

Table 2-6 – Interaction probabilities between photons of different energy and 1 mm CdTe detector. This table does not include the effective depth due to hole tailing effect.

2.5 Signal Processing System

2.5.1 Amplifier

The amplifier is used to amplify and shape the pulses from the pre-amplifier into Gaussian shape and pass them to Multichannel Analyser (MCA) for digitization. The PX2CR from Amptek was used for pulse height analysis in this thesis, which is not only an amplifier with adjustable gain but also a power supply for the detector. It provides a high bias voltage for the CdTe detector to build a strong electric field for charge collection. It also has a function called "Rise time discrimination" (RTD) to improve the resolution of a peak by rejecting long rise time pulses with low charge collection efficiency. In this method, all pulses with a risetime exceeding some threshold are rejected, therefore, all pulses which contribute to the tail are rejected. When RTD is on, the tail disappears and the peak width decreases, which means the counting efficiency is decreased but the resolution is improved. According to the mechanism of RTD, the main peak area will not be disturbed. The counts entering the main peak will remain the same no matter RTD is on or off. In this thesis, all the results were obtained by keeping the RTD off to achieve the highest counting efficiency. For modeling convenience, the intensity of each peak was calculated by mainly using the main peak area for such peaks with long tails.

The gain of the amplifier is adjustable from 1 to 10. For all the measurements done by using this amplifier in this thesis, the gain was adjusted to be 10, but this amplifier has gain drift. The drift is usually caused by two factors. One is manual error, and the other is temperature variation. The gain of the PX2CR amplifier is adjusted manually by rotating a knob on the front panel. Experiment results for one set of samples like kaolin of

different concentrations usually require one day to be finished. If the amplifier gain was changed during the break between two sets of measurements, it cannot be recovered to the original position with 100% precision. After long time measurement, the gain of the amplifier will also drift due to temperature increase, which changes the centroid of a peak to a minor extent and causes 1 or 2 channels shift for the peaking channel. This issue can be avoided by reducing the measurement time. However, for low radiation sources, longer measurement time is always necessary to improve the accuracy. In this case, the energy scale needs to be calibrated for each spectrum according to the peak channel number, which ensures that the determined peak area in each spectrum is always in the same energy range.

2.5.2 Multi-channel Analyzer

The multi-channel analyzer separates the pulses from the amplifier into different channels according to the pulse height in volt. A corresponding relationship is built between voltage and channel number. Each channel accumulates counts with a different pulse height during measurement. After further calibration, the channel number scale can be transformed to an energy scale. The MCA-8000A from Amptek was used as the multi-channel analyzer in this thesis.

The MCA-8000A has two peak detection modes. One is “First peak mode”. In this mode, the multi-channel analyzer records a peak when the pulse exceeds the threshold voltage set. Before this peak falls to the threshold again, if there is second peak occurring, the second peak will also be recorded as a count. This mode is designed for nuclear instrumentations where two counts may occur closely in time domain and are both valid. The other mode is “Absolute peak mode”. In this mode, when the analyzer detects a peak, if there is a second, or third or fourth peak that occurs before the first peak returns to the threshold, the highest peak will be recorded. This mode is usually used for particle sizing analysis, where the highest peak is the interested one. [34][35] The “First peak mode” was selected for this study as our application is a typical nuclear counting application.

The full voltage scale of MCA-8000A can be selected to be 5 V or 10 V. The channel number is also selectable from 256 to 16384. These two parameters can be selected along with the gain value of the PX2CR amplifier to make the spectrum spread to the full scale

with reasonable resolution and include interested energy range. In this study, 5 V and 1024 channels were used for ^{241}Am, and 10 V and 1024 channels were selected for ^{133}Ba.

In Amptek's digitization processors, real time is the time during which the measurement is made, which is also called measurement time. Live time is the time during which the detection system is open to pulses. At very high counting rate, if the multichannel analyzer is busy digitizing a previous pulse, a new pulse that reaches the circuit might not be analyzed. In this case, the digitization system is not open to the new pulse, and the live time becomes shorter than the real time. In this study, the measurement time was counted in real time, however, this does not affect the results much as the highest counting rate is around 9 counts per second, and the live time is only 0.04 s shorter than the real time for a 30-minute measurement.

The MCA communicates with the host computer via RS232 serial interface. The ADMCA software (Amptek) can display the real-time spectrum and save the received data after measurement. There are 128 different memory groups in the MCA. The acquired data are also saved in the memory. The MCA can work alone without the host computer. When it is connected to the host computer again, the spectrum in the most recently accessed group is transferred and displayed.

2.6 Data Processing

2.6.1 Peak Search

The peak channel number is an important reference when calibrating the spectra. Preliminary tests were performed to study the peak search method. For some peaks with high counting rate and in good shape, the peak channel is obviously where the highest value is. However, when measuring higher concentration samples with lower counting rates, such as 30 wt% and 40 wt%, peak shapes become more irregular due to much lower counting rate. It is difficult to determine which channel corresponds to the intensity peak. In this case, a peak searching method was proposed and applied to all the spectra. Due to the line broadening effects caused by the detection system, counts in the peak area follow a Gaussian distribution [36]. The raw spectrum was first smoothed by a window of 10 data points, and then the peak area was fitted into a Gaussian function to determine

the peak channel number. The result was rounded to the nearest integer. The peak channel number also indicates whether there is a gain shift. Then, the spectrum can be calibrated, and the energy range of the peak area can be determined.

The spectra shown in Figure 2-3 are the same ones as shown in Figure 2-2(a) and 2-2(c). A multiple peak least squares error Gaussian function fit was applied for the 16.9 keV and 17.8 keV peak regions of 32 channels. They were fitted with two Gaussian functions separately to form a cumulative fit peak. They have an equal constant component, y_0, which can be regarded as the background level for this smoothed spectrum. For 16.9 keV and 17.8 keV, the peak channel numbers were determined to be 266 and 278. For 31 keV, 11 channels were used for Gaussian fit, the channel of the highest value, 6 channels to its left, and 4 channels to its right, and the peak channel number was 235. For 59.5 keV and 81 keV, the peaks have a long scattered tail, so the whole peak cannot be fitted with a Gaussian function. However, the main peak area still has a Gaussian shape. To make comparison with simulation, the main peak area was selected and fitted with Gaussian functions. The result peak channel numbers for 59.5 keV and 81 keV are 910 and 600. For 81 keV, 9 channels were selected for the fit, the channel of the highest value, 4 channels to its left, and 4 channels to its right.

2.6.2 Spectrum Calibration

For ^{241}Am sources, the peak channel numbers of 17.8 keV and 59.5 keV were used for calibration. For the 1 μCi ^{133}Ba, 31 keV and 81 keV were used. A linear relationship was built between energy and channel number. The calibration functions from the spectra shown in Figure 2-3 are listed in Table 2-7, where y is the energy in keV, and x is the channel number. The slope of the calibration function is the response function (keV / Channel) of the spectrometer system. The calibrated spectra from Figure 2-3 are shown in Figure 2-4. The counts in the shaded area (selected peak area) are then added up to calculate the peak intensity.

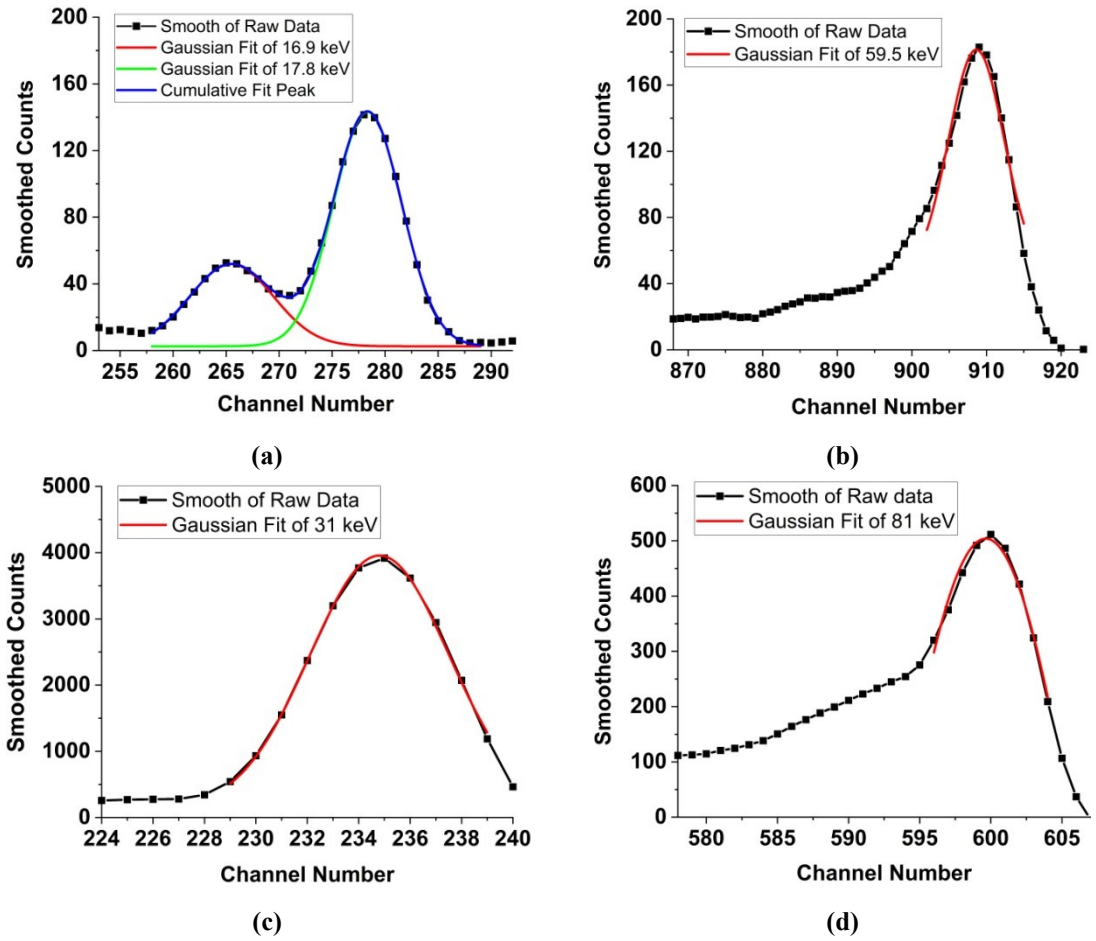

Figure 2-3 – (a) Multiple Gaussian function fit for two overlapped X-ray peaks, 16.9 keV and 17.8 keV. (b) Gaussian function fit for the peak area of 59.5 keV peak. (c) Gaussian function fit for 31 keV peak. (d) Gaussian function fit for 81 keV peak. The spectra are parts of the whole spectra shown in Figure 2-2 (a) and (c)

Source	Calibration Function
^{241}Am	y = 0.066x – 0.572
^{133}Ba	y = 0.137x – 1.438

Table 2-7 – Calibration functions for ^{241}Am and ^{133}Ba spectra shown in Figure 2-3, where y is the photon energy in keV and x is the channel number.

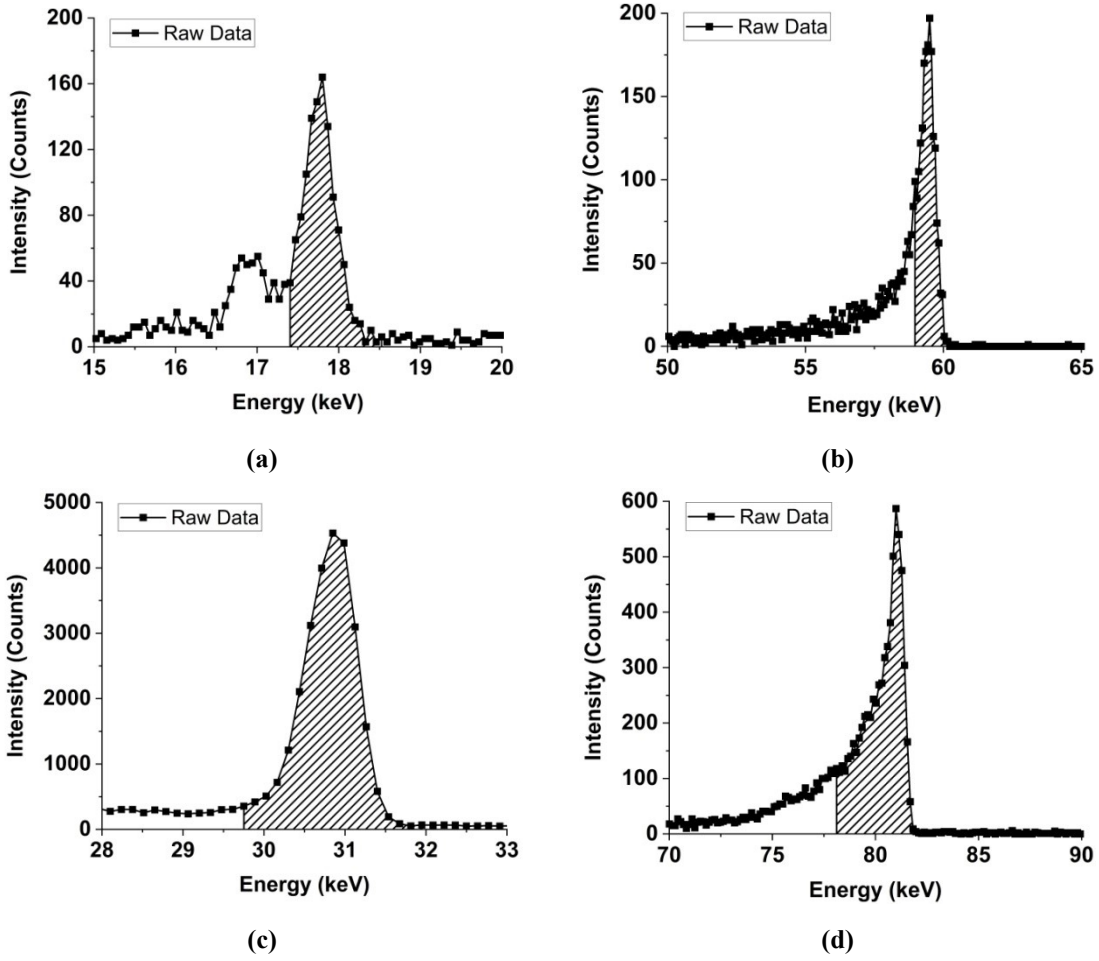

Figure 2-4 Energy range selected to calculate the intensity of (a) 17.8 keV, (b) 59.5 keV, (c) 31 keV, and (d) 81 keV lines. The spectra are parts of the whole spectra shown in Figure 2-2 (a) and (c)

2.6.3 Background Subtraction

The 17.8 keV peak has neighboring peaks on the higher energy side, which produce hole tailing tails that form an additional background under the peak area. This background is a character of a specific radiation source, geometry, and detection system, which does not affect the measurement much. However, it can generate a discrepancy when the experimental results are compared with calculations and simulations using monoenergetic peaks. For comparison with theoretical studies, the background in the experimental results was estimated and subtracted. The average counts per channel in the 10 channels at higher energy above the peak area was defined as average background (counts/channel) since it is closest to the peak area from the higher energy side. This average background was multiplied by the number of channels of the peak area and subtracted from the peak

area. For the 17.8 keV, 31 keV and 81 keV peaks, the same background subtraction method was used. There is no significant higher peak above 59.5 keV, so no background was subtracted.

2.6.4 Data Normalization

The average transmitted intensity and the standard deviation of 5 repeated measurements were calculated for analysis. The intensity measured is the counts of X-rays / γ-rays passing through the empty container plus a certain sample and being captured by the detector. All components of the experimental setup always remain unchanged except the chemical compositions of the samples in the container. In other words, it can be regarded that the variation of sample concentrations in the container leads to the variation of X-ray / γ-ray attenuation. Thus, the intensity measured using each concentration was divided by the intensity measured using an empty cuvette or container to give a normalized transmission factor. The normalized transmission is a useful parameter as allowing calculation of sample absorption using the Beer Lambert Law. Assuming A is the transmitted intensity for a sample with certain wt%, and B is the transmitted intensity for the empty container, then A/B is the normalized transmission fraction, f, as shown in Equation 2-3a. The standard deviation of the normalized transmission was calculated according to the error propagation theory, Equation 2-3b. The standard deviation of A and B are σ_A and σ_B. The covariance σ_{AB} is always zero in this study since the measured intensity for each concentration is independent, so Equation 2-4 is the final equation used for standard deviation calculation.

$$f = \frac{A}{B} \quad \textbf{(2-3a)}$$

$$\sigma_f \approx |f| \sqrt{\left(\frac{\sigma_A}{A}\right)^2 + \left(\frac{\sigma_B}{B}\right)^2 - 2\frac{\sigma_{AB}}{AB}} \quad \textbf{(2-3b)}$$

$$\sigma_f \approx |f| \sqrt{\left(\frac{\sigma_A}{A}\right)^2 + \left(\frac{\sigma_B}{B}\right)^2} \quad \textbf{(2-4)}$$

2.7 Sample Characterization and Preparation

2.7.1 Sample Density

The density is an important parameter for both calculations and simulations. Sample density was measured using small polystyrene cuvettes. The outer dimensions of the

cuvette are 12.5 mm × 12.5 mm × 45 mm. The inner dimensions are 10 mm × 10 mm × 45 mm. Two sides of this cuvette are polished and have a measuring window. The top edge of this window was used as a mark line for calibration. The volume of the measuring cuvette was first calibrated by using distilled water and a balance. First, the mass of an empty cuvette was measured by the balance. Then, the cuvette was filled with distilled water to the mark line. After that, the mass of distilled water was measured by the balance. The volume of water was calculated assuming the density of distilled water to be 1 g/cm^3. Finally, the cuvette was filled with sample to the mark line and measured by the balance, and the mass of the sample was obtained. The density was calculated by dividing the sample mass by the water volume. The data are shown in Table 2-8. The measurement error was estimated to be at most ± 0.008 g/cm^3. (The water volume is 3.25 ± 0.02 ml. The maximum mass of sample is 4.287 ± 0.001 g.)

Sample	Weight percent of solid content			
	10%	20%	30%	40%
NRCAN Kaolin	1.065	1.148	1.236	1.310
BASF G90 kaolin	1.059	1.145	1.224	1.319
NAIT-FFT-1	1.056	1.133	1.200	1.281

Table 2-8 – Measured sample density (± 0.008 g/cm^3)

2.7.2 Inductively Coupled Plasma Mass Spectrometry

Inductively coupled plasma mass spectrometry (ICP-MS) creates ions by atomizing and ionizing the sample using a high temperature inductively coupled plasma. The ion beam is focused and guided into a mass analyzer by a set of electrostatic lenses called ion optics. Then, the ions are separated by the mass analyzer according to their mass-charge ratio (m/z) and measured by a detector.[37] ICP-MS was used to obtain the chemical compositions of the samples. There are two sample digestion methods available for ICP-MS measurement. One is Na_2O_2 digestion, and the other is mixed acid (HF, HNO_3 and HCl) digestion. When the Na_2O_2 digestion is used, the wt% of Na cannot be measured due to the residual Na after the digestion. When the mixed acid digestion is used, Si cannot be characterized as it is vaporized. An investigation was made to determine which digestion method should be used for kaolin and FFT samples.

In oil sands tailings, while the quartz settles rapidly, clay and fine solids (together called fluid fine tailings or FFT) can take decades to settle on their own.[38] Clay is the main component of FFT. There are also some fine quartz (SiO_2) and residual bitumen particles. Kaolin and illite are the main clay components in FFT.[39] From the chemical formulas of kaolin ($Al_2Si_2O_5(OH)_4$) and illite ($(K, H_3O)(Al,Mg,Fe)_2(Si,Al)_4O_{10}[(OH)_2,(H_2O)]$) [40], it is known that Na is not part of the normal composition of clay. Using the mixed acid digestion methods, the wt% of Na in 6 different tailings samples was measured to be 0.186 % ± 0.02 %. The measured results and chemical composition of clay indicate Na is not a main chemical composition of FFT-1. Thus, the Na_2O_2 digestion method was used before ICP-MS measurement. The main metal element (wt % > 0.4 %) composition of FFT-1 obtained by ICP-MS was used for further calculations and simulations, and Na was not considered.

NRCAN Kaolin and BASF G90 Kaolin are in powder form and were directly measured. The original FFT-1 sample is a liquid sample directly collected from tailings ponds at CNRL's Albian site. The solid content wt% is 41.2 wt%. The dried powder of this sample obtained from Dean Stark was pulverized and measured by ICP-MS. The bitumen in the sample was removed by Dean Stark. Estimation for the mass fraction of oxygen and hydrogen was done because the ICP-MS device cannot measure the wt% of H and O. According to the chemical formulas of clay and quartz, the non-metal elements only contain O and H. For FFT-1, based on the analysis above, it is reasonable to make an estimation that the unknown 56% non-metal elements are oxygen (O) and hydrogen (H). The ratio of the atomic number of H and O is 1:2.25 and 1:2 for kaolin and illite respectively according to the chemical formulas. This atomic number ratio can also vary in different mining areas. However, no matter what the wt% of each chemical composition in the clay group is, the calculated results show the wt% of H is between 1.59 wt% ~ 1.79 wt%. In this thesis, 1.59 wt% was used for calculations and simulations according to the kaolin formula. Then, the remaining 56.9 wt% was determined to be oxygen. This estimation will cause little effect on the evaluation of the attenuation property of the FFT since the range of H is relatively small and contribution to the overall weight is small. The calculated values are shown in Table 2-9.

If the sample contains elements that can produce high energy X-ray fluorescence, it may affect the experimental results. X-ray fluorescence (XRF) is the emission of characteristic "secondary" X-rays from a material that has been excited by being bombarded with high-energy X-rays or gamma rays. Among all the elements shown in Table 2-9, Fe has the highest X-ray fluorescence energy around 6.4 keV when ionized [41], which is well below the lowest X-ray energy studied by this thesis, 13.9 keV. Thus, X-ray fluorescence causes little effect on this application.

Six ICP-MS results of CNRL-6 FFT were used to estimate the error of the ICP-MS measurement. The relative standard deviation (%) of the weight percent for each element was calculated, as shown in Table 2-10. The RSD can be used to estimate the upper and lower boundary of the wt% of each element. The increase of the wt% of other elements will decrease the wt% of oxygen and hydrogen based on the estimation. This result was used to evaluate the influence of chemical analysis error on the results of simulation, which will be shown and discussed in Chapter 5.

Element	Sample		
	NRCAN Kaolin	BASF G90 Kaolin	FFT-1
Al	22.0803	20.2974	10.5178
Si	23.3937	22.0959	25.4928
Fe	0.520250	0.651316	1.86135
Ca	0.396126	0.264105	0.731621
K	0.410898	0.130686	1.95710
Ti	0.212448	0.408370	0.438089
Mg	0.115035	0.0217410	0.534096
H	1.15365*	1.52894*	1.59260*
O	41.3349*	54.6016*	56.8746*

* Calculated Value.

Table 2-9 – Chemical Compositions from ICP-MS (wt%)

Element	Al	Si	Fe	Ca	K	Ti	Mg
Average	11.2374	25.9021	2.5832	0.372944	1.91252	0.515054	0.52720
Std. dev.	0.5251	0.7203	0.1379	0.130400	0.10364	0.041122	0.03485

RSD (%)	4.67	2.78	5.34	34.97	5.42	7.98	6.61

Table 2-10 – Error analysis on 6 ICP-MS results of main metal composition of CNRL-6 FFT (wt%)

2.7.3 Settling Observation

Before the X-ray attenuation experiment, a settling observation was done to observe the sample settling rate. The settling rate of kaolin is dependent on the pH of the solution. The lowest settling rate of kaolin was at pH 8 ~ 10 according to the measurement made by L Besra et al. [42]. The pH of the original NRCAN kaolin solution was measured to be around 4. To mitigate the settling effect of NRCAN kaolin, 2~3 drops 1M NaOH were added to 2.5 wt% kaolin solution to adjust the pH to be 8 ~ 10. Observation showed this method was effective. As shown in Figure 2-5, with NaOH, no visible settling was seen for 30 minutes, which is enough for measurements using ^{241}Am sources. For 10 wt% BASF kaolin, no visible settling was observed in 30 minutes, as shown in Figure 2-6. The solution was homogenous and stable without showing any layers. It indicates that the attenuation experiment can be carried out up to 30 minutes without significant settling effect. From the observation test for 10 wt% FFT-1, after 10 minutes, it was seen that only an extremely thin layer was on the bottom of the cuvette, as shown in Figure 2-7. However, after 30 minutes, the settling particles formed a much thicker layer, which possibly affects the experiment results seriously. To mitigate the settling effect, a data collection method was used for 30-minute attenuation experiment, FFT-1 solutions were mixed every 10 minutes by a glass rod to mitigate the settling effect. When the sample to be tested was being mixed, the data collection was paused. It was restarted after the mixture to accumulate data for the next 10 minutes without being interfered with.

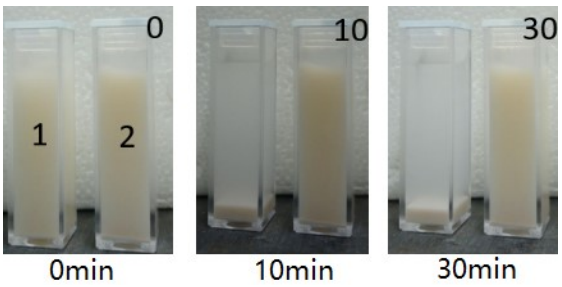

Figure 2-5 – Settling observation on 2.5 wt% NRCAN kaolin solution with or without adding NaOH (1. 2.5 wt% NRCAN Kaolin; 2. 2.5 wt% NRCAN Kaolin + 2~3 drops of 1M NaOH)

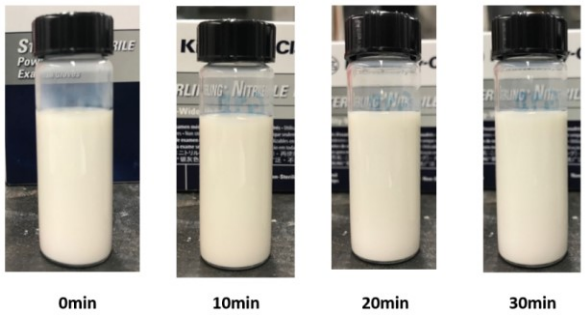

Figure 2-6 – Settling observation on 10 wt% BASF G90 kaolin solution for 30 minutes

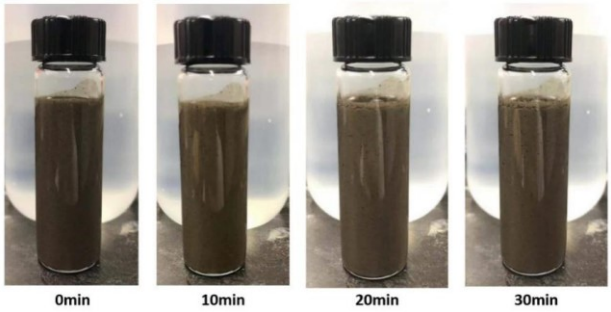

Figure 2-7 – Settling observation on 10 wt% FFT-1 solution for 30 minutes

2.7.4 Sample Preparation

The original NRCAN kaolin and G90 kaolin powder were dissolved in distilled water to make solutions with different wt% including 10 wt%, 20 wt%, 30 wt% and 40 wt%. 2~3 drops 1M NaOH were added to NRCAN kaolin solutions to adjust the pH to be between 8 and 10. The original liquid FFT-1 sample was diluted with distilled water into the same concentrations as those of the kaolin solutions.

2.8 Summary

In this chapter, based on Beer-Lambert law, the general design of the experiment setup was proposed. ^{241}Am and ^{133}Ba were chosen to be the radioactive sources for attenuation experiment after comparing several common ones. An Amptek XR-100T CdTe detector was used to build a detection system with other signal processing stages. A series of data analysis issues related to calibration and background analysis were discussed, and corresponding solutions were proposed. Density measurements were done to obtain sample densities at different concentrations. ICP-MS with Na_2O_2 digestion was used to obtain the chemical compositions of the kaolin and FFT-1 samples. Estimation for wt% of H and O was carried out for the samples based on the ICP-MS results and standard

weight ratios expected for clay samples. These values of composition are used for calculations and simulations to be presented in the following chapters. Settling phenomenon was observed for some samples. Mitigation methods were applied, and good performance was seen.

3. Experimental Results and Discussion

3.1 Preliminary Tests

3.1.1 Sample Thickness

The polystyrene cuvettes used for measuring the sample density were used as sample containers for preliminary tests of the 0.9 μCi ^{241}Am, so the sample thickness for ^{241}Am sources is 1 cm. This sample thickness gave good results, and the 1 cm cuvette was used as the sample container for ^{241}Am measurements. The results will be shown in the results and discussion section (3.3.1). However, a 1 cm gap may not be sufficient to guarantee the homogeneity of the sample inside and outside the measured zone and to allow good flow of sample through the measurement volume for real settling ponds measurements. The sample thickness was increased for the 1 μCi ^{133}Ba source since the higher energy of the 31 keV X-rays allows larger penetration depths through the samples. At the beginning of the experiments with ^{133}Ba, to obtain similar performance to the 0.9 μCi ^{241}Am source with increased sample thickness, tests were carried out with different sample path lengths. The spectra were processed without subtracting the background. The intensity ratios were all normalized by assuming the value for water to be 3. Two FFT samples from CNRL (wt% of solid content: 18.2 wt% and 31.5 wt%) were measured by the 1 μCi ^{133}Ba source. Between the source and the detector, 2, 5, 6 and 7 cuvettes, with 1 cm path length each, were put side by side to form different sample thicknesses. The measured zone was filled tightly by cuvettes without extra space. The measurement time is 10 minutes. As shown in Figure 3-1(a), the error bars of 2, 5 and 6 are acceptable. It is seen that the results of 5 and 6 cuvettes of 31.5 wt% sample are quite close to the normalized ratio of 0.9 μCi ^{241}Am at 30 wt% FFT-1, and the sensitivity is even higher for 6 cuvettes, which indicates the acceptable sample thickness can be up to 50 mm or 60 mm. A new sample cell was made from acrylic square tube with dimensions of 43 × 43 mm, allowing for even higher weight density samples to be measured accurately. The preliminary results obtained by using the square acrylic tube were satisfactory, so it was selected to be the sample container for the ^{133}Ba measurements. It is seen that with this thicker cell the intensity ratio of 31 keV to 81 keV peaks is a good monitoring parameter for solid content in FFT.

3.1.2 Measurement Time

Using a measurement time for the 0.9 µCi ^{241}Am of 10 minutes, the partial spectrum for 40 wt% FFT-1 is shown in Figure 3-2. It is seen that the 17.8 keV can be fitted with a Gaussian function even at the lowest counting rate. The error bar is also acceptable, as shown in the results and discussion given later. The measurement time for the 1 µCi ^{133}Ba was 10 minutes in the preliminary tests. After subtraction of the background, the error bars of the normalized transmission of 81 keV are a bit too large, as shown in Figure 3-3. To obtain more accurate results to allow for more accurate comparison to the simulated results, the measurement time was increased to 30 minutes. The data quality was significantly improved, as shown in the results and discussion part.

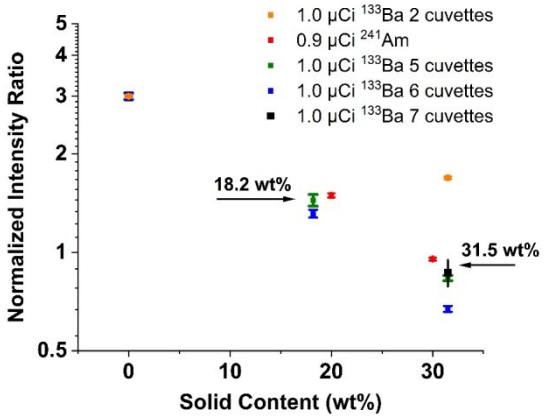

Figure 3-1 – Normalized intensity ratio of ^{241}Am (20 wt% and 30 wt% FFT-1) and ^{133}Ba for 18.2 wt% and 31.5 wt% CNRL samples, using different total sample thicknesses for ^{133}Ba.

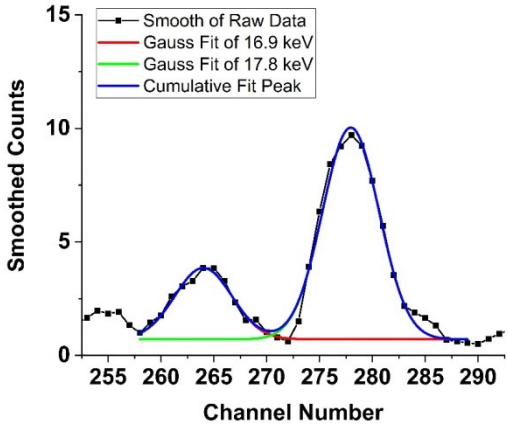

Figure 3-2 – Multiple Gauss fit for two overlapped X-ray peaks, 16.9 keV and 17.8 keV in a 40 wt% FFT-1 spectrum obtained by using the 0.9 µCi ^{241}Am source and 1 cm cuvette in 10 minutes.

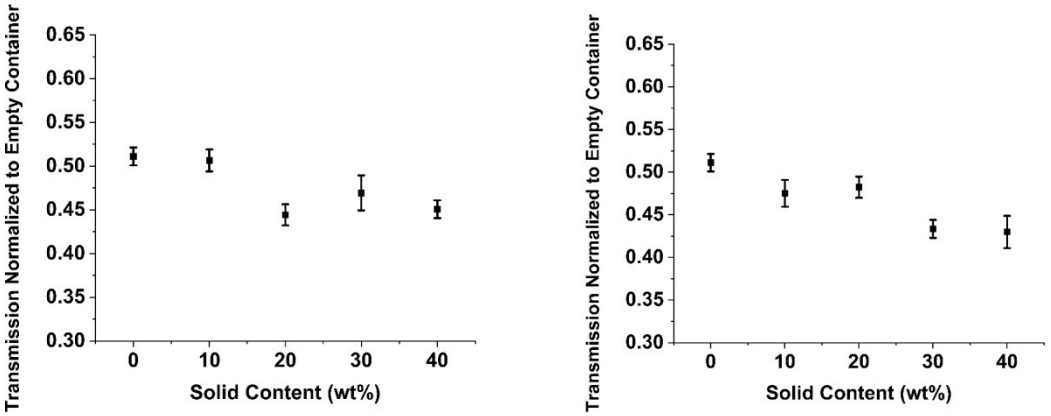

(a) G90 kaolin **(b) FFT-1**

Figure 3-3 – Normalized transmission of 81 keV for (a) G90 kaolin and (b) FFT-1 measured by using the 1 µCi ^{133}Ba source in 10 minutes (The sample thickness is 43 mm)

3.1.3 Energy Comparison for ^{241}Am

There are many X-ray peaks in ^{241}Am spectra that possibly can be used as peaks for monitoring. The spectra were processed to determine the performance of each peak. The measurement was repeated 5 times to obtain average intensity and the error bar of the average. As a preliminary test, background subtraction was not performed. A second order polynomial fit was performed for the intensity versus weight percent for each energy of 13.9 keV, 17.8 keV and 20.8 keV in the linear scale. The intensity and fitted curves were finally plotted in the logarithmic scale to make the lower intensity easy to be read, shown in Figure 3-4. The fitted curves describe the ideal relationship predicted by experimental data between the peak intensity and solid content wt%. The slope of the intensity curve was calculated for each wt% and divided by the intensity measured using a 1 cm cuvette with distilled water, and then multiplied by 100%. The absolute value of this percentage was defined as “slope rate” to evaluate the performance of X-rays with different energy. The slope rates of the intensity curves fitted in the linear scale were shown in Figure 3-5. Higher slope rate means the X-ray energy has higher sensitivity to the variation of solid content wt%. With the lowest energy among the three peaks, the 13.9 keV peak has the highest slope rate versus concentration below 25 wt% for both sets of samples. However, the slope rate almost reaches 0 for 40 wt% NRCAN kaolin and FFT-1, which indicates that the sensitivity of 13.9 keV at higher concentration is very poor since most photons are attenuated and only the background is left. The 20.8 keV has the best performance above 25 wt%, but it has the lowest slope rate below 25 wt%,

shown as overlapped error bars for water and 10 wt% kaolin and FFT-1. The 17.8 keV shows better performance than 20.8 keV does below 25 wt%, and it has a higher slope rate than 13.9 keV above 25 wt%. According to the data from IAEA (Table 2-2), the 17.8 keV also has the highest emission probability among the three lines. In conclusion, high emission probability and the reasonable sensitivity in a wide wt% range make 17.8 keV the most suitable peak to monitor the solid content when ^{241}Am sources were used. The monitoring parameter of ^{241}Am sources was finally determined to be the intensity ratio of 17.8 keV and 59.5 keV.

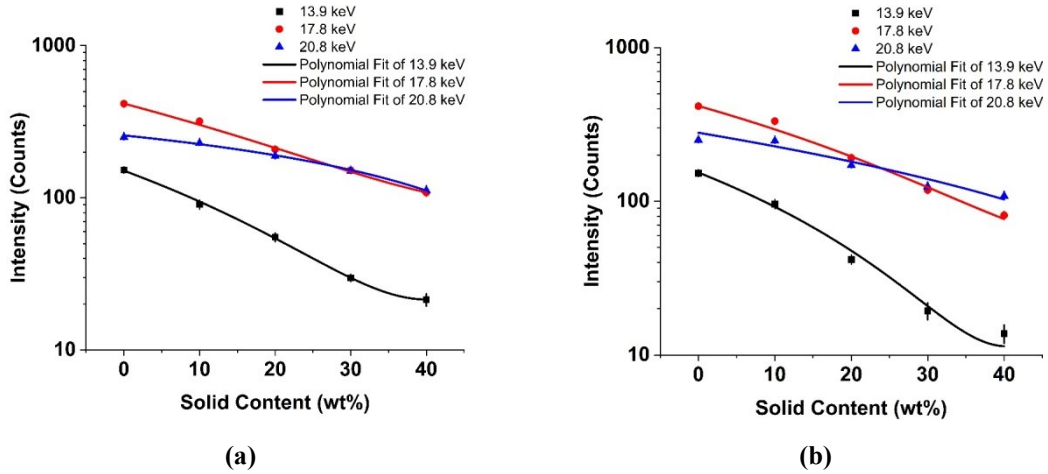

Figure 3-4 – Transmission normalized to empty cuvette value for 13.9 keV, 17.8 keV and 20.8 keV for samples of different concentrations. The results were processed using a fixed energy range without background subtraction. (a) NRCAN kaolin (b) FFT-1.

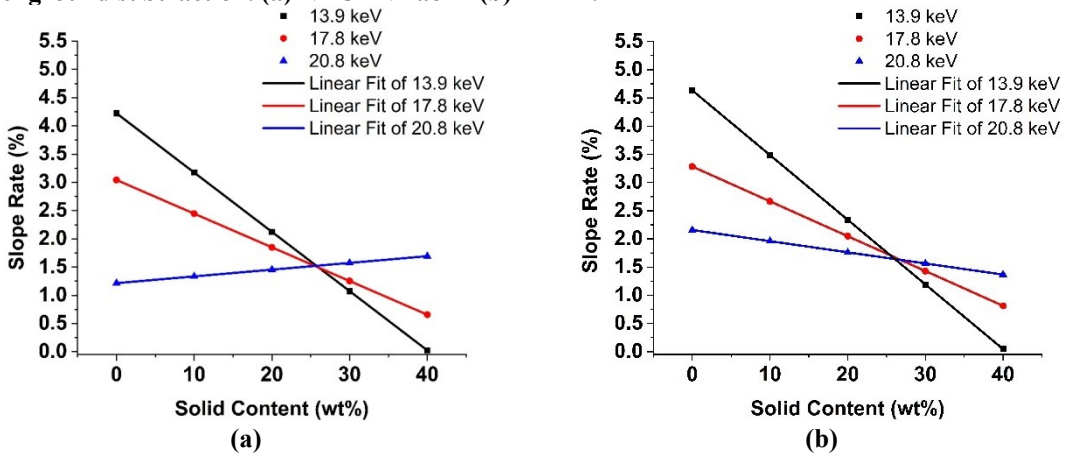

Figure 3-5 – Slope rate of the normalized transmission of 13.9 keV, 17.8 keV and 20.8 keV (a) NRCAN kaolin (b) FFT-1

3.2 Geometry of Experiment Setup

The measurement holder for the ^{241}Am sources was made from a bulk aluminum block. There are slots where sources with holder, sample container, and detector can be fitted

and fixed, as shown in Figure 3-6. At both sides of the cuvette in the X-ray / γ-ray transmitting direction, two 2 mm thick aluminum block was built to hold the cuvette. On the sheet at the source side, a circle hole of Ø 8 mm was to enable the transmission of X-rays / γ-rays. The 2 mm aluminum sheet can block most of the 17.8 keV counts, which also limits the cone angle. On the sheet at the detector side, the diameter of the hole is 10 mm, which is the same as the width of the sample. The 0.9 μCi ^{241}Am source was sealed in a plastic disc and then mounted in a polyvinyl chloride (PVC) source holder. The 10 μCi ^{241}Am source was placed in a similar source holder. The setup was designed to ensure the center of the detector probe and the center of the source were aligned. The distance between the center of the radioactive material and the detector element surface is 28.8 mm for both sources. The sample dimensions are 10 mm × 10 mm × 32 mm when cuvette is filled up to its marked scale.

The experimental setup for the 1 μCi ^{133}Ba source consists of a source holder, a sample container and the Amptek detection system, as shown in Figure 3-7. The material of the sample container is acrylic. The dimensions of this container are 43 mm × 43 mm × 100 mm (inner dimensions), and 46 mm × 46 mm × 100 mm (outer dimensions). About 166 mL solution was filled in the container and made the height of the top surface reach the mark at around 90 mm, which guarantees the parameters of the setup geometry are constant for different samples. The source was placed at 15 mm to the left container surface, and the detector was placed at 8 mm to the right surface. The distance between the source center to the detector element surface is 70.3 mm. The source and detector were aligned to the center of the sample vertically and horizontally.

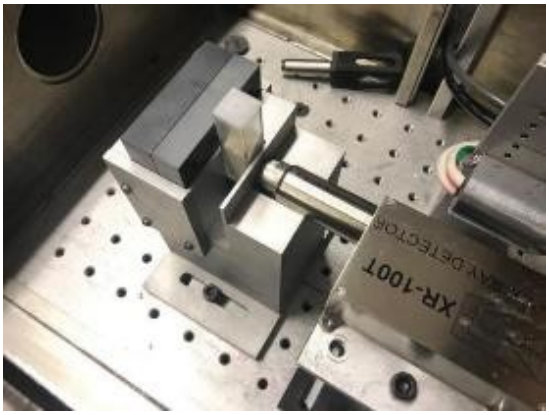

Figure 3-6 – ^{241}Am experiment setup

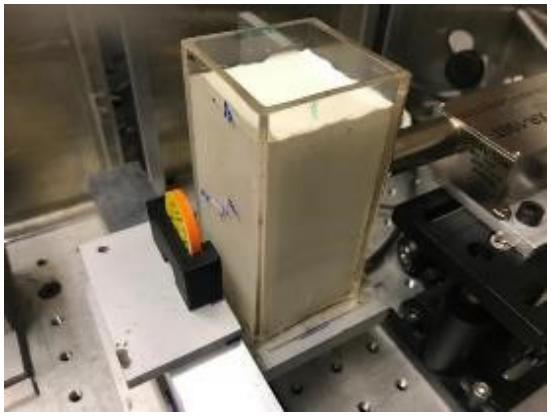

Figure 3-7 – ^{133}Ba experiment setup

3.3 Results and Discussion

3.3.1 ^{241}Am Sources

The results for the 0.9 μCi ^{241}Am source are shown in Figures 3-8 to 3-10. The intensity of transmitted 17.8 keV X-ray photons constantly decreases with the increase of solid content. The intensity of 59.5 keV also shows a decreasing trend; although, the error bars of 10% NRCAN kaolin and 10% FFT-1 samples are overlapped with that of water. However, this does not contribute a large error to the intensity ratios, shown in Figure 3-10. The variation of ratio with wt% is very clear for both NRCAN kaolin and FFT-1 samples from 0 wt% to 40 wt%. The results show that at least ± 5 wt% resolution on solid content can be achieved. However, the sample thickness used here is only 1 cm, which may not be sufficient for the real tailings ponds measurements to ensure homogeneity of the samples inside and outside the measured volume.

The results of the 10 μCi ^{241}Am source are shown in Figures 3-11 to 3-13. Compared with the 0.9 μCi ^{241}Am source, the trend of the intensity of 17.8 keV and 59.5 keV, and intensity ratios is similar, but the intensity of each peak is around 10 times higher as the strength increases. Theoretically, the intensity ratio and be calculated according to Table 2-2 and 2-4 and will not change with the strength of sources as the nucleus is always ^{241}Am and the spectra were processed using the same energy ranges. However, the radioactive material is sealed in different containers or structures such as ceramic beads, plastic disks or mixed with gold and silver particles for safety concerns. The strength of the real source, and intensity of each radiation peaks will be affected by the packaging. The shape of some peaks will also be distorted to some extent as photons are scattered by the sealing material. In this study, the intensity ratio of the 10 μCi ^{241}Am source is lower than of the 0.9 μCi ^{241}Am source at each wt%.

In order to check the measured counts against the theoretically expected counts an absolute calibration of the source emission was carried out in air. The distance between the center of the radioactive material in the sources and the Be window of the detector is 27.5 mm. The detector element is located 1.27 mm behind the 0.1 mm thick Be window. The minimum transmission of 17.8 keV and 59.5 keV through this Be window is 99.52 % and 99.72 %, (total attenuation), which is negligible. The distance between the center of

the ^{241}Am sources and the surface of the detection element is 28.8 mm. The emission probability for 17.8 keV and 59.5 keV are 0.1886 and 0.3578. The detection efficiency (η) of 1 mm CdTe detector for 17.8 keV and 59.5 keV are 0.9878 and 0.9749, (photoelectric absorption), calculated according to Table 2-6 by interpolation. The activity (A_c) of the 0.9 μCi and 10 μCi source is 33300 Bq (decay/s) and 370000 Bq, respectively. The sources are assumed to be point sources. The area of the detector element can be regarded as a part of the radiation sphere with a radius (r) of 28.8 mm. The area of the detector element is 9 mm^2. The theoretical counts (I) in 10 minutes can be calculated using Equation 3-1.

$$I = A_c * E * \eta * [\, 9/(4\pi r^2) \,] * 600 \qquad \textbf{(3-1)}$$

	0.9 μCi		10 μCi	
	17.8 keV	**59.5 keV**	**17.8 keV**	**59.5 keV**
Theoretical	3221	6030	35786	67005
Experimental	1108	4002	10927	61409
Transmission	0.344	0.664	0.305	0.916

Table 3-1 – Theoretical and experimental values of 17.8 keV and 59.5 keV for 0.9 μCi ^{241}Am and 10 μCi ^{241}Am. The experimental data was measured by using Amptek XR-100T CdTe detector with a distance of 28.8 mm between the sources and the detector element surface for 10 minutes.

As shown in Table 3-1, the theoretical and experimental intensity values of 59.5 keV peak are quite close for 10 μCi ^{241}Am, though the experimental value is a little bit lower possibly due to the scattering effect. For 17.8 keV, the experimental value is around 30% of the theoretical one. In the schematic from the source manufacturer shown in Figure 3-14(a), the radioactive material was incorporated in an organic ion exchange bead or in ceramic, which possibly attenuates a large number of 17.8 keV photons but causes little attenuation to the 59.5 keV. The 17.8 keV of the 0.9 μCi ^{241}Am source has similar attenuation caused by the sealing structure shown in Figure 3-14(b), but the 59.5 keV is attenuated more than that of the 10 μCi ^{241}Am according to Table 3-1. One possible explanation for this discrepancy is that the actual strength of the ^{241}Am source from the smoke detector is lower than 0.9 μCi, and the transmission of 59.5 keV should be much higher than the calculated value.

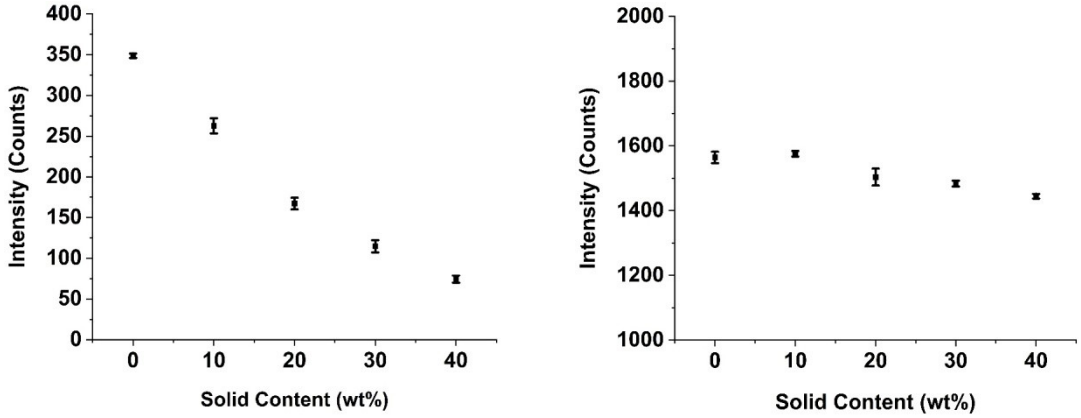

(a) 17.8 keV **(b) 59.5 keV**

Figure 3-8 – Measured 17.8 keV and 59.5 keV intensities for NRCAN kaolin using 0.9 µCi ^{241}Am

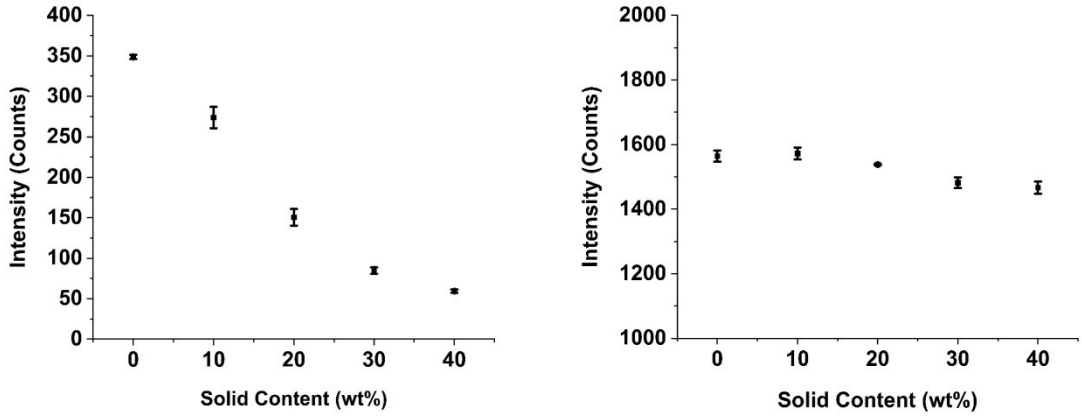

(a) 17.8 keV **(b) 59.5 keV**

Figure 3-9 – Measured 17.8 keV and 59.5 keV intensities for FFT-1 using 0.9 µCi ^{241}Am

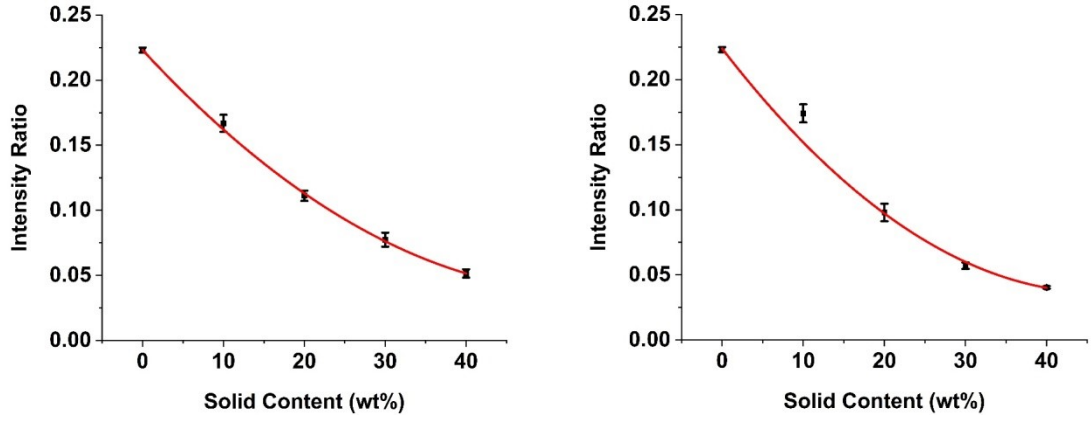

(a) NRCAN Kaolin **(b) FFT-1**

Figure 3-10 – Measured intensity ratio of 17.8 keV and 59.5 keV for (a) NRCAN kaolin and (b) FFT-1 using 0.9 µCi ^{241}Am. The red solid lines are second polynomial fits of data points.

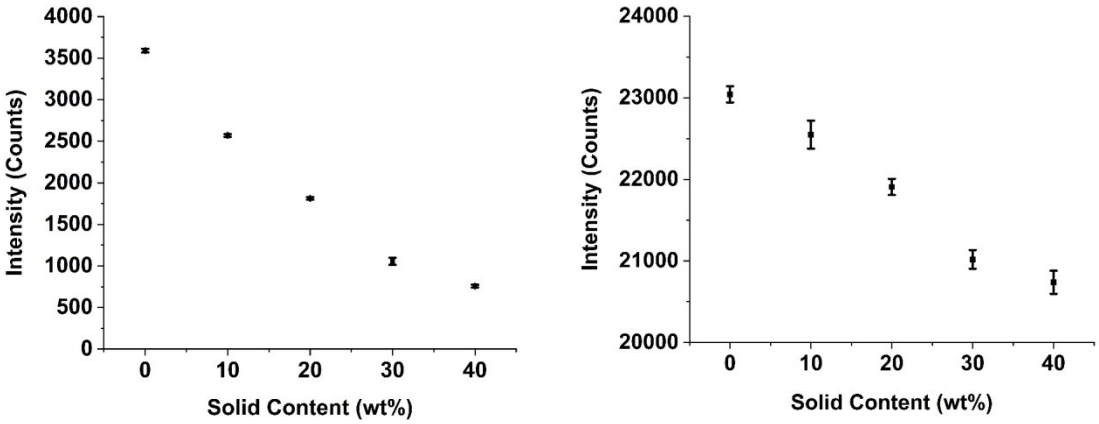

(a) 17.8 keV **(b) 59.5 keV**

Figure 3-11 – Measured 17.8 keV and 59.5 keV intensities for NRCAN kaolin using 10 µCi ^{241}Am

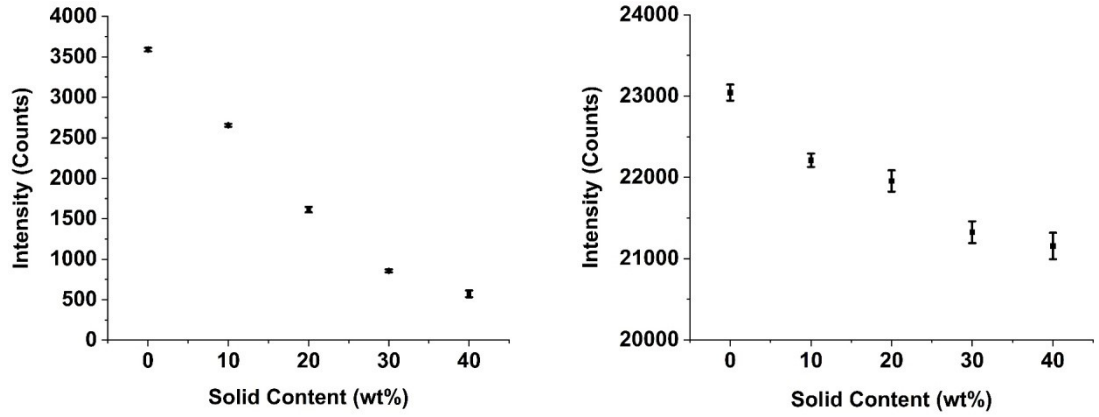

(a) 17.8 keV **(b) 59.5 keV**

Figure 3-12 – Measured 17.8 keV and 59.5 keV intensity for FFT-1 using 10 µCi ^{241}Am

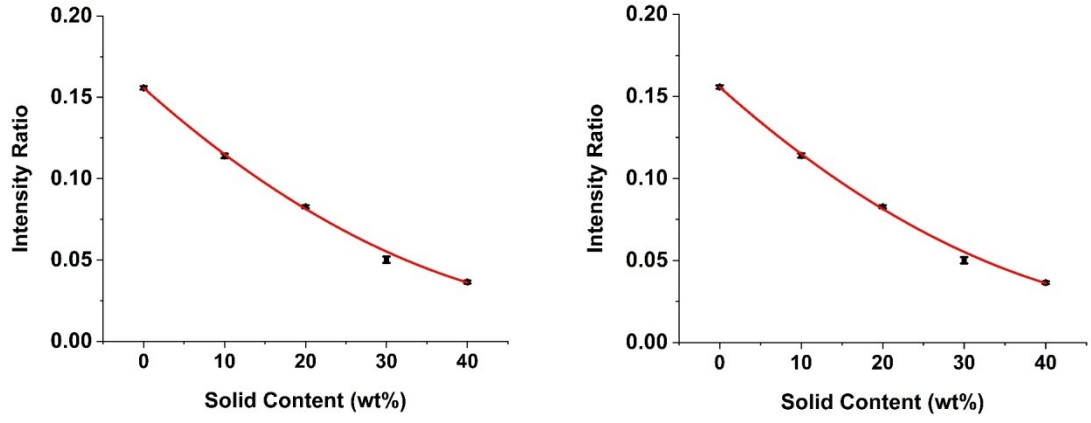

(a) NRCAN kaolin **(b) FFT-1**

Figure 3-13 – Measured intensity ratio of 17.8 keV and 59.5 keV for (a) NRCAN kaolin and (b) FFT-1 using 10 µCi ^{241}Am. The red solid lines are second polynomial fits of data points.

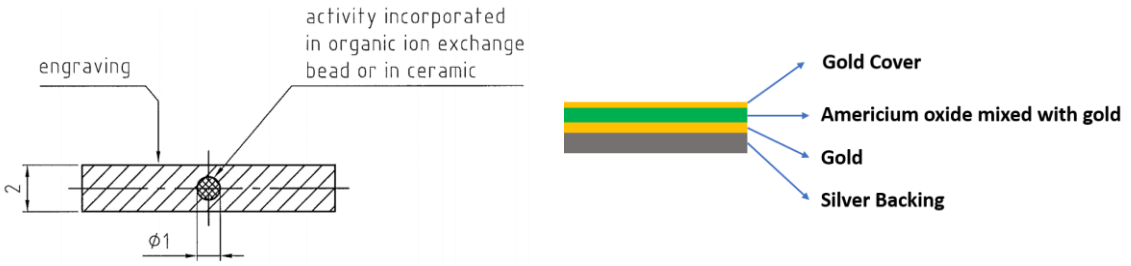

(a) **(b)**

Figure 3-14 – The structure schematic of (a) the commercial 10 µCi ^{241}Am source and (b) a general ^{241}Am source in smoke detectors

3.3.2 1 µCi ^{133}Ba Source

For the 1 µCi ^{133}Ba source good measurements of solid content were also possible. As shown in Figures 3-15 to 3-17. It demonstrates similar solid content resolution as the 10 µCi ^{241}Am does with a more than 4 times longer sample thickness, which enables measurements in practical environment that need more space to allow the samples to flow freely through the monitored region in real applications. The 43 mm container contains more samples than the 1 cm cuvette does, which also improves the homogeneity of the sample and the measurement accuracy. The intensity of 81 keV emission in main peak area is still low even though the measurement time is 30 minutes. The larger error bars will affect the comparison between the experimental and the simulation results, which will be shown and discussed in Chapter 5.

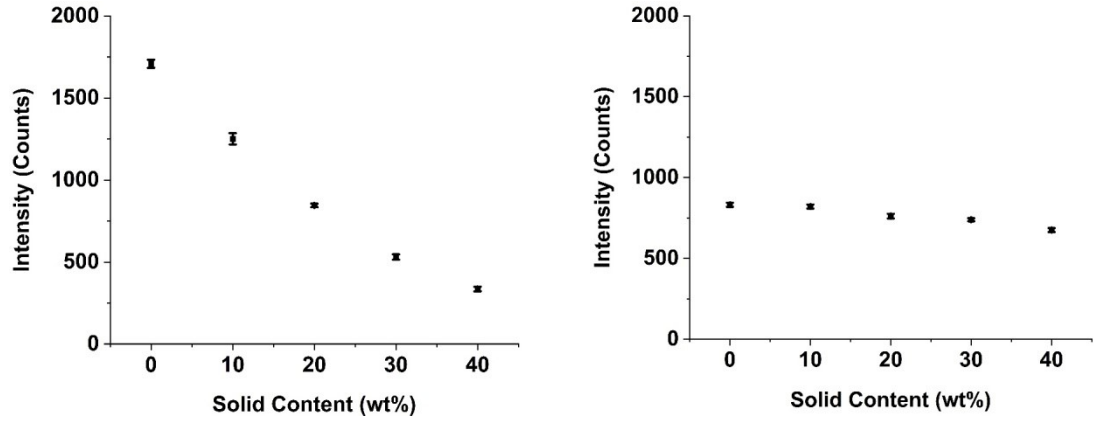

(a) 31 keV **(b) 81 keV**

Figure 3-15 – Measured intensity of (a) 31 keV and (b) 81 keV for G90 kaolin using 1 µCi ^{133}Ba in 30 minutes

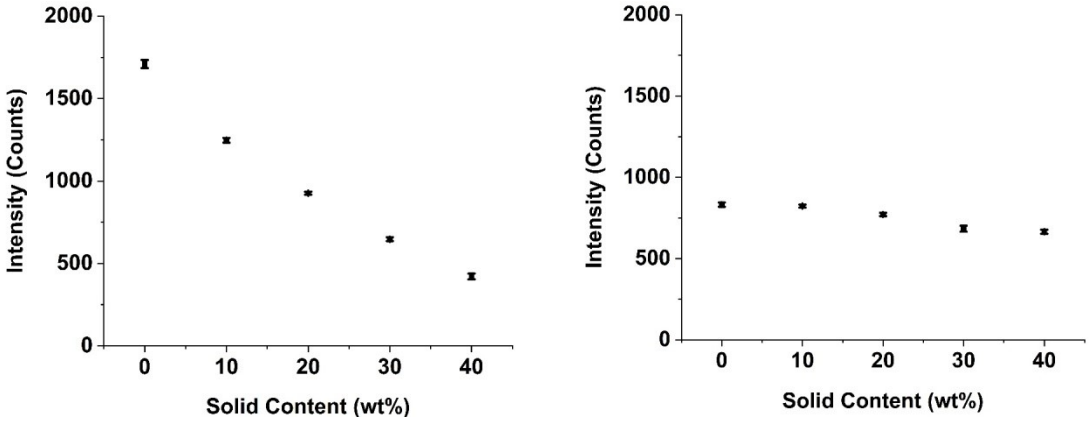

(a) 31 keV **(b) 81 keV**

Figure 3-16 – Measured intensity of (a) 31 keV and (b) 81 keV for FFT-1 using 1 µCi ^{133}Ba in 30 minutes

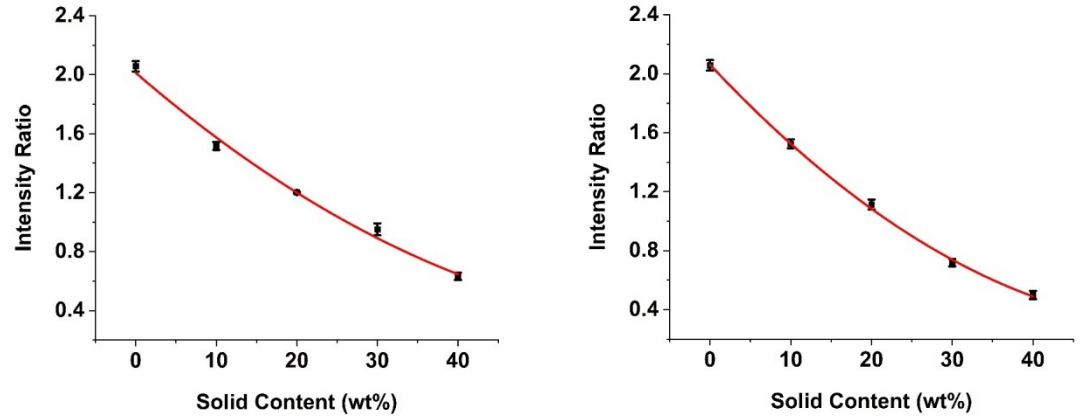

(a) G90 Kaolin **(b) FFT-1**

Figure 3-17 – Measured intensity ratio of 31 keV and 81 keV for (a) G90 kaolin and (b) FFT-1 using 1 µCi ^{133}Ba in 30 minutes. The red solid lines are second polynomial fits of data points.

3.3.3 Source Performance Comparison

Similar to the comparison of X-ray emission lines for ^{241}Am in the preliminary tests described above, the slope rate of the intensity ratio was also calculated, as shown in Figure 3-18. For kaolin and FFT-1 samples, below 25 wt%, the 0.9 µCi ^{241}Am source with 1 cm sample thickness provides a much higher slope rate than the 1 µCi ^{133}Ba configuration does. At 30 wt%, the performance of the two configurations are quite similar. Above 30 wt%, the 1 µCi ^{133}Ba shows better performance as the characterization peak energy, 31 keV, is higher than 17.8 keV. It is seen that the performance of these two sources are both acceptable, and the 0.9 µCi ^{241}Am configuration has better resolution on

lower solid content concentrations. However, one obvious advantage of using the 1 μCi ^{133}Ba configuration is that the sample thickness can be more than 4 times of that for ^{241}Am with similar radioactivity level, which improves the homogeneity of samples without losing much slope rate. The maximum strength of a ^{133}Ba source is 2.7 μCi in Canada, without requiring to go through a licensing process, which is 10 times the limit for ^{241}Am due to its higher atomic number and emission of alpha radiation.[43] ^{133}Ba provides more possibility for reducing measurement time and improving accuracy. Thus, the 1 μCi ^{133}Ba configuration was selected for further tests and optimization.

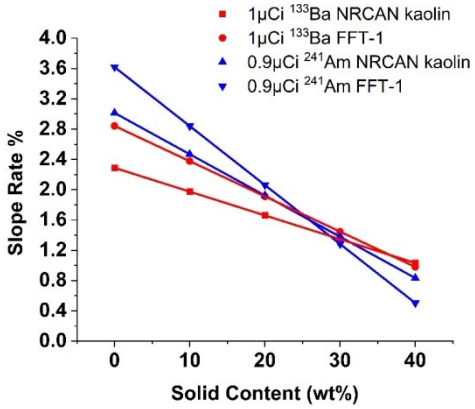

Figure 3-18 – Slope rate of intensity ratio versus sample concentration using 0.9 μCi ^{241}Am, and 1 μCi ^{133}Ba. All the solid curves were fitted by linear fit.

3.4 Summary

Two experimental setups were built for 0.9 μCi ^{241}Am and 1 μCi ^{133}Ba sources separately according to a similar general design. The performance of different X-ray peaks in ^{241}Am spectra were compared. The 17.8 keV peak was selected as the characterization peak for solid content because of its good sensitivity over a wide wt% range and high emission probability. The experimental results show it is possible to build a solid content sensor using a low activity radiation source such as 0.9 μCi ^{241}Am and 1 μCi ^{133}Ba and achieve a resolution of several wt%. The resolution performance of the two configurations were compared. The 1 μCi ^{133}Ba configuration was selected for further study due to its good resolution of solid content, increased penetration depth and ability to use at higher activities below the license limit.

4. Modeling

4.1 Mass Attenuation Calculation

Mass attenuation calculation provides a simple and fast estimation of X-ray or gamma ray attenuation through the samples. The attenuation is calculated based on the probability of a radiation photon interacting with an atom in an absorber. This probability depends on the cross-section of each interaction process. The interaction processes include photoelectrical absorption, coherent scattering (Rayleigh scattering), incoherent scattering (Compton scattering), and pair production. In photoelectric absorption, the photon disappears after interacting with a bound electron, and the total photon energy is transferred to this electron. A photoelectron is generated and ejected from the atom. Rayleigh scattering is an elastic scattering process without energy loss, and only the direction of the photon is changed. Compton scattering is an inelastic scattering process. Part of photon energy is transferred to the electron the photon interacts with, and the direction is changed. Pair production only occurs when photon energy is higher than 1022 keV, which is not considered here. [44]

The attenuation coefficients of all these effects can be obtained from the XCOM database [45], which is available on NIST (National Institute of Standards and Technology) website.

For an X-ray / γ-ray beam of mono-energetic photons, the change in intensity at some distance in a material can be expressed as Equation 4-1, where dI is the change in intensity; I is the initial intensity; n is the density of atoms (the number of atoms per unit volume); σ is interaction cross-section, which reflects the total probability of a photon being scattered or absorbed; dx is the incremental thickness of material traversed. When Equation 4-1 is integrated, it becomes Equation 4-2a. The density of atoms and interaction cross-section are usually combined to yield the linear attenuation coefficient (μ). Therefore, the equation becomes Equation 4-2b, where I is the transmitted intensity; I_0 is the initial intensity; μ is the linear attenuation coefficient (cm^{-1}); this in turn can be defined in terms of the mass absorption coefficient, μ_m, as defined in Equation 4-2c, where ρ is the mass density of the material; x is distance traveled. For calculation convenience, Equation 4-2b can be written in a form explicitly related to mass density

using mass attenuation coefficient, and I / I_0 is the calculated transmission, as shown in Equation 4-2d.

$$dI(x) = -I(x) \cdot n \cdot \sigma \cdot dx \quad \textbf{(4-1)}$$

$$I = I_0 e^{-n\sigma x} \quad \textbf{(4-2a)}$$

$$I = I_0 e^{-\mu x} \quad \textbf{(4-2b)}$$

$$\mu_m = \mu/\rho \quad \textbf{(4-2c)}$$

$$I / I_0 = e^{-\mu_m \rho x} \quad \textbf{(4-2d)}$$

The mass attenuation coefficients of diluted kaolin and FFT samples in this study can be calculated by using Equations 4-3 and 4-4, where μ_m is the mass attenuation coefficient of the solid content in kaolin or FFT; μ_{mi} and w_i wt% are the mass attenuation coefficient and wt% of the i_{th} constituent element in the solid content of kaolin or FFT; As shown in Equation 4-4, the diluted sample can be regarded as a homogeneous mixture of solid content and water. w_t wt% is the solid content wt% of the diluted solution. The container material was not considered in this calculation. The attenuation due to air with thicknesses of 1 cm and 43 mm is negligible. Thus, the initial transmission of empty containers in this calculation was assumed to be 1.

$$\mu_{m(\text{kaolin or FFT})} = \sum \frac{w_i \text{ wt\%}}{100 \text{ wt\%}} * \mu_{mi} \quad \textbf{(4-3)}$$

$$\mu_{m(\text{Diluted Sample})} = w_t \text{ wt\%} / 100 \text{ wt\%} * \mu_{m(\text{kaolin or FFT})} + (100 \text{ wt\%} - w_t \text{ wt\%})/100 \text{ wt\%} * \mu_{m(H_2O)} \quad \textbf{(4-4)}$$

4.2 GEANT4 Simulation

4.2.1 Geometry of the Simulation Setup

For the GEANT4 model, the ^{241}Am setup was built with two aluminum sheets at both sides of the cuvette in the X-ray / γ-ray transmitting direction and an aluminum block to form the same slot as that of the real experiment setup. Two holes were also created on the sheets with the same dimensions as the real setup. The material of the cuvette wall was defined as polystyrene. The height of the sample was defined to be 32 mm. Other geometry parameters were also obtained from the real setup and used as the simulation input, which ensures that the simulation setup recovers the real geometry as accurately as

possible. In the front of the detector, a Beryllium window with a thickness of 100 μm was built as described in the technical reference of the CdTe detector. For the ^{133}Ba source, the 43 mm thickness container simulation setup was also built using the same dimensions and material as those of the real setup, as shown in Figure 4-2. The bottoms of the two containers were not built as they are parallel to the X-ray / γ-ray transmitting direction and can be ignored.

4.2.2 Definition of Samples

The chemical compositions of 100% kaolin and FFT were defined in the calculation using Table 2-9. The diluted samples were defined as they were prepared. The wt% of each element in the original sample was multiplied by the wt% of the solution after dilution. Then, the wt% of the element in the final solution was obtained. An example on calculating the wt% of Aluminum in 10 wt% NRCAN kaolin solution is shown as Equation 4-5.

wt% of Al in 10 wt% NRCAN kaolin

= (10 wt% / 100 wt%) * (wt% of Al in original NRCAN kaolin / 100 wt%) * 100 wt%

= 2.20803 wt% **(4-5)**

The density of sample at each wt% was defined using the measured density shown in Table 2-8. The density defines the mass of sample per unit volume. The mass of each element in a unit volume can then be calculated using the wt% obtained from Equation 4-5. Then, the number of each type of atoms in unit volume can be calculated using relative atomic mass. This is how samples are defined by their density and wt%.

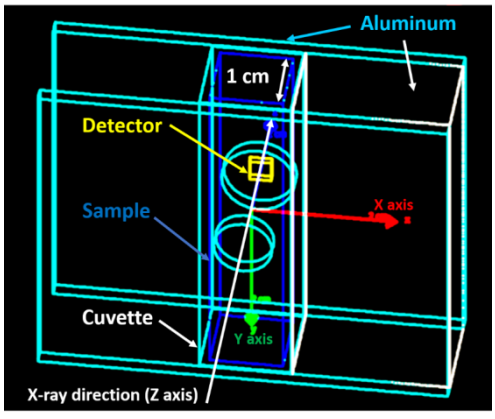

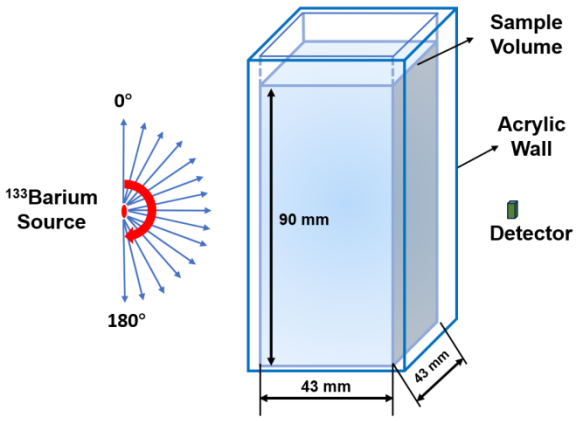

Figure 4-1 – GEANT4 simulation setup for ^{241}Am **Figure 4-2 – GEANT4 simulation setup for ^{133}Ba**

4.2.3 Definition of Sources

For the ^{241}Am setup, the source was defined as a point source as the area where the radioactive material is located subtends a very small angle when viewed from the point of observation. For the ^{133}Ba setup, the radiation source was defined in a plane circle shape with a radius of 3.175 mm as described in the information about the source. X-rays and γ-rays from the ^{241}Am point source were emitted with an "isotropic" distribution. From the ^{133}Ba source, they were emitted with a $\cos(\theta)$ distribution, where θ is the direction relative to normal. These settings ensure the flux of photons is the same when viewed at any position at the sample side. Monochromatic sources were used. The transmission of X-rays or gamma rays of each energy were simulated separately. The cone angle of the two sources was defined from 0 to 180 degrees to ensure that all the world space at the sample side will be illuminated by the radiation rays, which includes the scattered phenomenon occurring outside the cone angle formed by the source and the detection surface. Each run has 250,000,000 photons emitted.

4.2.4 Photon Counting and Output

The photon counting mechanism is same for both setups. The detection volume contains 1024 scorers with different energy intervals that form the same energy bins as the MCA8000A multi-channel analyzer. The interval of these energy bins was calculated based on the calibration information of real spectra measured by the empty cuvette or container using the Amptek detection system. Gamma filters were applied on the detector to shield high energy electrons. The scorer is set to be FlatSurfaceCurrent mode, which can capture all the photons passing through the detector surface towards -Z direction, so this detector was placed on the Z axis and the rays from the radiation source were directed to +Z direction. The counting parameter of this detector was set as " In ", which means that only photons coming into this detection volume will be counted. The incident photons will be classified according to their energy and form a spectrum after being accumulated in different energy bins. The output file is in .txt format and contains the number of photons in each energy bin. The raw output spectra of each simulated energy for container with air and water were plotted in Figure 4-3. It is seen that all the energies

have a main peak (the highest value) and a scattering tail. The main peak contains most of the detected photons including the transmitted photons without interactions with the material and scattered photons that experience Rayleigh scattering without energy loss. The scattering tails are caused by Compton scattering. The direction of the scattered photon is changed, and part of energy is lost. The main peak of each input energy for air is always higher than that of water. The intensity of the scattered tail for air is a little bit lower than that of water. It indicates that, compared with air, water attenuates more photons, and the Compton scattering is more observable.

To evaluate the error bars of the average, pseudo-random number generator was used to add random noise to the output results of the simulation. By changing the random seed, the simulation will generate results with additional random statistical noise with the same input parameters. Simulation for each concentration was repeated 5 times to obtain the average and the error bar.

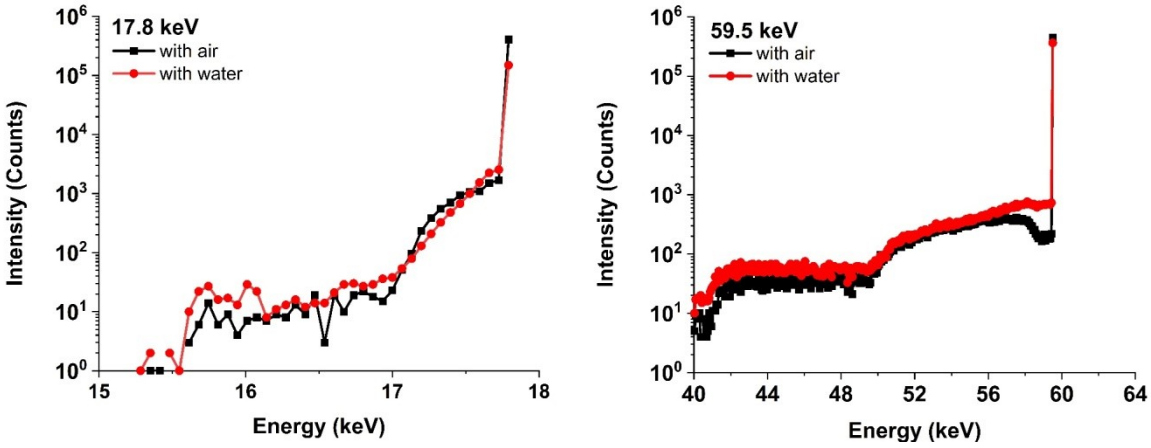

(a) **(b)**

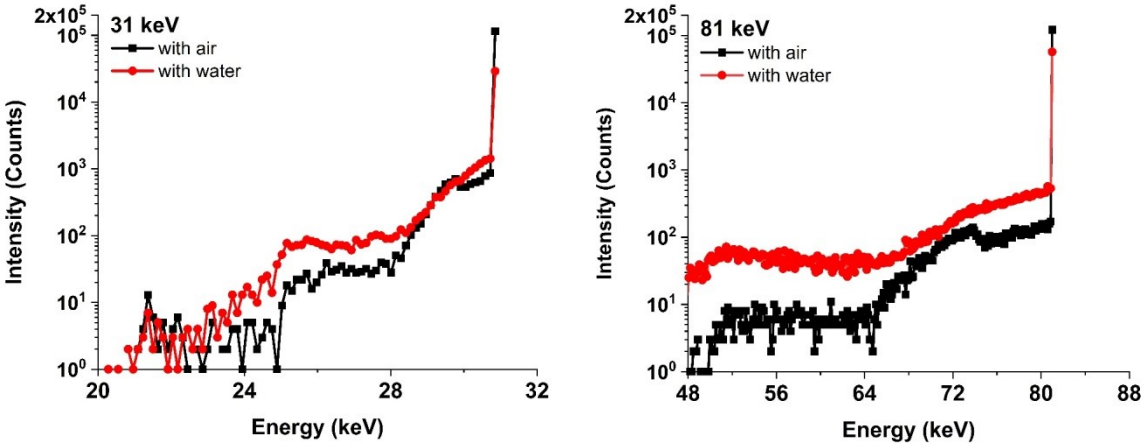

(c) (d)

Figure 4-3 Raw outputs of GEANT4 simulation of (a) 17.8 keV, (b) 59.5 keV, (c) 31 keV and (d) 81 keV for a sample container with air and water.

4.2.5 Simulation Data Processing and Analysis

The interactions inside the detector and the digitization process of the electronics system are too complicated to be simulated and it would cost too much computing resource. The aim of the simulation is to verify the experimental results based on Beer Lambert law and make prediction after a first-time calibration. It is not necessary to simulate all the details of the detector. As what was done to the experimental results, the normalized transmission values of all the simulated energies was obtained. The energy range that defines the peak area in the simulation data was determined by making the normalized transmission of water match the experimental result first. Then, simulated data for all the concentrations of kaolin and FFT-1 were processed using the same determined energy range. In the simulation results, the intensity ratios for all the concentrations were normalized by setting the value of the empty container to be 1. To compare with the experimental results, the normalized intensity ratios were multiplied by the average experimental intensity ratio from a set of five measurements using the empty container. The standard deviation and error bars of the average were also calculated according to the error propagation theory. The normalized transmission of 17.8 keV and 31 keV, and intensity ratios were fitted into 2nd order polynomial curves. For 59.5 keV and 81 keV, the fitting function is linear because the larger error bar of each data point leads to poorer results when a 2nd order fit applied.

4.3 Summary

This chapter introduced the principles of mass attenuation calculation, and derives the equations to calculate mass attenuation coefficients of different wt% samples using the mass attenuation coefficients of the main elements. The transmission for different energy and sample thickness can be calculated according to Beer-Lambert law. The configurations and analysis techniques of the GEANT4 simulation were also introduced. With these two powerful modeling tools, the experimental results can be compared with the modeling results for verification and prediction.

5. Modeling Results and Discussion

5.1 Mass Attenuation Calculation Results

5.1.1 Mass Attenuation Coefficient Results

The mass attenuation coefficients of each main element in the samples were calculated by interpolation according to NIST XCOM database, as shown in Table 5-1. The mass attenuation coefficients of samples at each concentration were calculated and shown in Table 5-2.

Element	Mass attenuation coefficients (Photoelectric absorption) μ_m in cm2/g			
	17.8 keV	**31 keV**	**59.5 keV**	**81 keV**
Al	5.0400E+00	8.2785E-01	9.9400E-02	3.6859E-02
Si	6.6200E+00	1.1022E+00	1.3400E-01	4.9889E-02
Fe	3.8800E+01	7.3850E+00	1.0100E+00	3.9593E-01
Ca	1.9800E+01	3.5440E+00	4.6000E-01	1.7547E-01
K	1.6600E+01	2.9304E+00	3.7600E-01	1.4309E-01
Ti	2.4100E+01	4.3959E+00	1.6300E+01	2.2375E-01
Mg	3.9748E+00	6.4378E-01	7.6407E-02	2.8195E-02
H	4.3600E-04	5.8360E-05	5.9000E-06	2.0489E-06
O	1.0200E+00	1.5559E-01	1.7500E-02	6.3277E-03

(a) Photoelectric absorption

Element	Mass attenuation coefficients (Total attenuation) μ_m in cm2/g			
	17.8 keV	**31 keV**	**59.5 keV**	**81 keV**
Al	5.4277E+00	1.0804E+00	2.8232E-01	2.0023E-01
Si	7.0489E+00	1.3735E+00	3.2650E-01	2.2084E-01
Fe	3.9500E+01	7.7895E+00	1.2426E+00	5.8403E-01
Ca	2.0421E+01	3.8878E+00	6.7596E-01	3.6008E-01
K	1.7130E+01	3.2530E+00	5.8280E-01	3.2057E-01
Ti	2.4659E+01	4.7366E+00	1.6851E+01	3.9855E-01
Mg	4.3444E+00	8.9280E-01	2.6061E-01	1.9378E-01
H	3.7254E-01	3.5605E-01	3.2648E-01	3.0837E-01
O	1.2924E+00	3.6775E-01	1.9183E-01	1.6726E-01

(b) Total attenuation

Table 5-1 – Mass attenuation coefficients of the main elements in kaolin and FFT-1 samples

Sample		Mass attenuation coefficients (Photoelectric absorption) $\mu_{m(Sample)}$ in cm^2/g			
	wt%	17.8 keV	31 keV	59.5 keV	81 keV
Water	0	9.0694E-01	1.3824E-01	1.5546E-02	5.6197E-03
NRCAN Kaolin	10	1.1650E+00	1.8236E-01	2.4377E-02	7.6852E-03
	20	1.4230E+00	2.2649E-01	3.3209E-02	9.7508E-03
	30	1.6811E+00	2.7062E-01	4.2040E-02	1.1816E-02
	40	1.9391E+00	3.1475E-01	5.0872E-02	1.3882E-02
G90 Kaolin	10	1.1631E+00	1.8200E-01	2.7412E-02	7.6686E-03
	20	1.4193E+00	2.2577E-01	3.9278E-02	9.7175E-03
	30	1.6755E+00	2.6953E-01	5.1144E-02	1.1766E-02
	40	1.9316E+00	3.1330E-01	6.3010E-02	1.3815E-02
FFT-1	10	1.2279E+00	1.9441E-01	2.9582E-02	8.3355E-03
	20	1.5489E+00	2.5058E-01	4.3619E-02	1.1051E-02
	30	1.8698E+00	3.0676E-01	5.7655E-02	1.3767E-02
	40	2.1908E+00	3.6293E-01	7.1691E-02	1.6483E-02

(a) Photoelectric absorption

Sample		Mass attenuation coefficients (Total attenuation) $\mu_{m(Sample)}$ in cm^2/g			
	wt%	17.8 keV	31 keV	59.5 keV	81 keV
Water	0	1.1892E+00	3.6648E-01	2.0695E-01	1.8305E-01
NRCAN Kaolin	10	1.4541E+00	4.1317E-01	2.1658E-01	1.8549E-01
	20	1.7191E+00	4.5985E-01	2.2622E-01	1.8793E-01
	30	1.9840E+00	5.0654E-01	2.3585E-01	1.9037E-01
	40	2.2490E+00	5.5322E-01	2.4549E-01	1.9280E-01
G90 Kaolin	10	1.4508E+00	4.1121E-01	2.1812E-01	1.8398E-01
	20	1.7125E+00	4.5595E-01	2.2930E-01	1.8490E-01
	30	1.9742E+00	5.0068E-01	2.4047E-01	1.8583E-01
	40	2.2358E+00	5.4542E-01	2.5165E-01	1.8676E-01
FFT-1	10	1.5162E+00	4.2395E-01	2.2045E-01	1.8474E-01
	20	1.8433E+00	4.8143E-01	2.3394E-01	1.8643E-01
	30	2.1704E+00	5.3891E-01	2.4744E-01	1.8812E-01
	40	2.4975E+00	5.9638E-01	2.6094E-01	1.8981E-01

(b) Total attenuation

Table 5-2 – Mass attenuation coefficients of kaolin and FFT-1 samples of different wt%

5.1.2 Peak Overlap Evaluation for ^{241}Am

In ^{241}Am spectra, the 17.8 keV peak has an overlap with its neighbor peak, 16.9 keV, as shown in Figure 2-3(a). A mass attenuation calculation (photoelectric absorption) was used to evaluate the effect of this peak overlap on measured transmission. The detailed results for this evaluation were attached in Appendix A. The peak area under each Gaussian curve excluding background can be calculated by integrating each function excluding the constant term in the peak area of 17.8 keV. Thus, one can figure out how much 16.9 keV contributes to the peak area of 17.8 keV. The results of the 10 μCi ^{241}Am source measured for 10 minutes were used for evaluation since the counting rate is high enough to form peaks with good Gaussian shapes. The attenuation of each peak varies with different sample concentrations and causes different overlap extent, so this evaluation was performed for all the concentrations of FFT-1 solutions. The highest error was found in the result of 30 wt% FFT-1. The average integrated intensity of the pure 17.8 keV peak of 5 measurements in the peak area is 920 ± 51. The average integrated intensity of the 16.9 keV peak is 15 ± 7. About 1.56 % ± 0.73 % of the 17.8 keV counts were actually 16.9 keV counts. The transmission through 1 cm 30 wt% FFT-1 calculated by using the spectra is evaluated to be decreased by 0.465 % ± 0.22 %. The results show that the left background of 17.8 keV caused by the overlap with 16.9 keV has only a minor effect on the transmission measurement of 17.8 keV.

5.1.3 Evaluation on the Effect of Residual Bitumen

The chemical composition of bitumen is very complicated. A chemical composition of Athabasca bitumen [46] was used for evaluating the effect of the residual bitumen on the X-ray / γ-ray attenuation results. The elemental composition of this bitumen contains 83.34 wt% C, 10.26 wt% H, 4.64 wt% S, 1.08 wt% O, 0.53 wt% N and 0.15 wt% others. The mass attenuation coefficients of bitumen at related energy values was calculated using the composition of the known elements, as shown in Table 5-3. The sum of the wt% of each known element was normalized to 1. The density of bitumen is between 1.01 ~ 1.06 g/cm^3. The X-ray / γ-ray attenuation property and density of water and bitumen are quite similar. It is assumed that the original FFT-1 (41.161 wt% solid content) sample contains 5 wt% residual bitumen. After being diluted, sample with 40 wt% solid content

has 4.86 wt% bitumen. The transmission of 17.8 keV and 59.5 keV through 1 cm thick 40 wt% FFT-1 with and without bitumen was calculated, as shown in Table 5-4 (a). The transmission of 31 keV and 81 keV through 43 mm thick 40 wt% FFT-1 with and without bitumen were calculated, as shown in Table 5-4 (b). It is seen that the calculated transmission results for all interested energy values of 40 wt% FFT-1 with or without bitumen show small differences. The residual bitumen has almost the same X-ray / γ-ray attenuation property as distilled water in the energy range of this study, so the residual bitumen has a minor effect on the modeling in this thesis.

Material	**Mass attenuation coefficients (Photoelectric absorption) $\mu_{m(Sample)}$ in cm^2/g**			
	17.8 keV	**31 keV**	**59.5 keV**	**81 keV**
Water	9.0694E-01	1.3824E-01	1.5546E-02	5.6197E-03
Bitumen	7.9078E-01	1.2735E-01	1.5123E-02	5.5914E-03

(a) Photoelectric absorption

Material	**Mass attenuation coefficients (Total attenuation) $\mu_{m(Sample)}$ in cm^2/g**			
	17.8 keV	**31 keV**	**59.5 keV**	**81 keV**
Water	1.1892E+00	3.6648E-01	2.0695E-01	1.8305E-01
Bitumen	1.0515E+00	3.4627E-01	2.0268E-01	1.8019E-01

(b) Total attenuation

Table 5-3 – Comparison on mass attenuation coefficients of water and bitumen for all the focused energy values in this thesis

Sample	**Photoelectric absorption**		**Total attenuation**	
	17.8 keV	**59.5 keV**	**17.8 keV**	**59.5 keV**
40 wt% FFT-1	0.06042	0.91225	0.04079	0.71587
40 wt% FFT-1 with Bitumen	0.06086	0.91228	0.04393	0.72515

(a) 1 cm sample thickness for 17.8 keV and 59.5 keV

Sample	**Photoelectric absorption**		**Total attenuation**	
	31 keV	**81 keV**	**31 keV**	**81 keV**
40 wt% FFT-1	0.13545	0.91321	0.03744	0.35150
40 wt% FFT-1 with Bitumen	0.13585	0.91321	0.03764	0.35177

(b) 43mm sample thickness for 31 keV and 81 keV

Table 5-4 – Comparison on calculated transmission of 40 wt% FFT-1 without bitumen and 40 wt% FFT-1 with 5 wt% bitumen for all the focused energy values and different sample thickness in this thesis.

5.1.4 Experimental and Calculated Results Comparison

As shown in the Figure 5-1 and Figure 5-2, the calculated results of X-ray / γ-ray transmission show considerable difference whether the scattering effect is included or not. The assumption considering only photoelectrical absorption always yield higher transmission values than the total attenuation one. This is because the former does not include the loss of photons in scattering process. However, the latter considers all scattered photons are lost, where in reality some are scattered back into the detector in a second scattering event. The two assumptions form a higher and a lower theoretical transmission limit. As the solid content wt% increases, the transmission values under different scattering assumptions both decrease. The experimental values of 59.5 keV are between the high and low limits, and follow the similar trend to the transmission limits. For 17.8 keV, the experimental values are very close to the upper limit, which indicates that most of the scattered photons were collected by the detector as the direction and energy change are relatively small in the scattering process. One discrepancy is that 10 wt% FFT-1 is a little bit out of the upper limit, which is possibly caused by the inhomogeneity of the sample. For 59.5 keV, the experimental values are close to the lower limit since the number of the captured scattered photons in the main peak area is low.

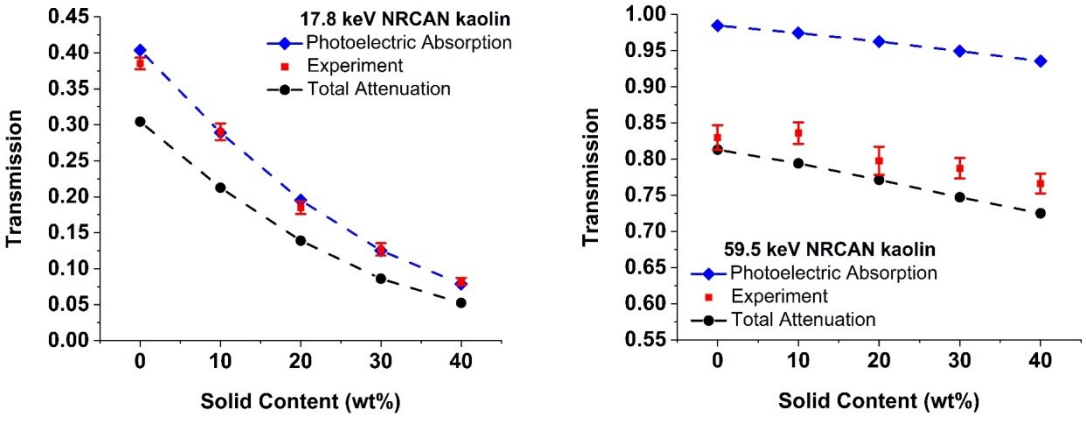

(a) 17.8 keV **(b) 59.5 keV**

Figure 5-1 – Measured normalized transmission of 17.8 keV and 59.5 keV and mass attenuation calculated transmission for NRCAN kaolin

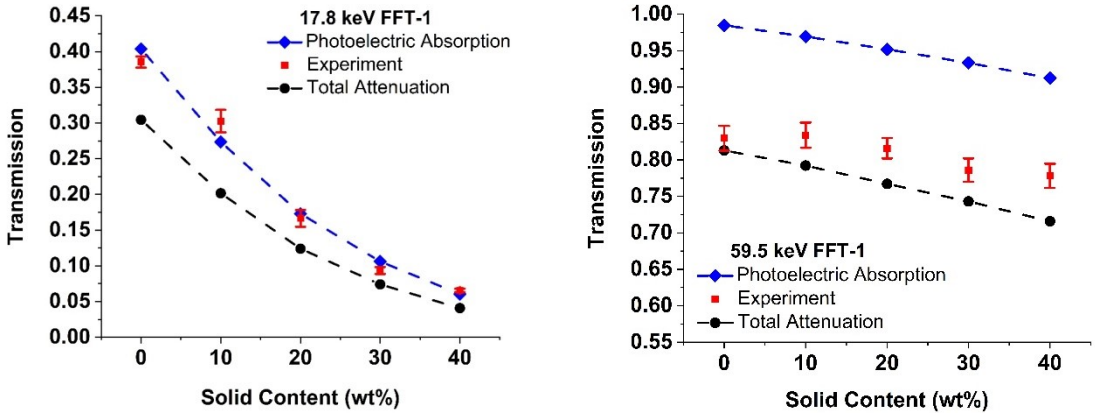

(a) 17.8 keV **(b) 59.5 keV**

Figure 5-2 – Measured normalized transmission of 17.8 keV and 59.5 keV and mass attenuation calculated transmission for FFT-1

Similar to ^{241}Am values, the experimental values of 31 keV and 81 keV are also between the upper and lower limits, and follow a similar trend with regards to the limit curves, as shown in Figure 5-3 and Figure 5-4. For 31 keV, the experimental values are close to the total attenuation limit, which indicates the scattering effect causes significant loss for the 31 keV counts. For 81 keV, the experimental values are close to the lower limit since the number of captured scattered photons is low in the main peak area.

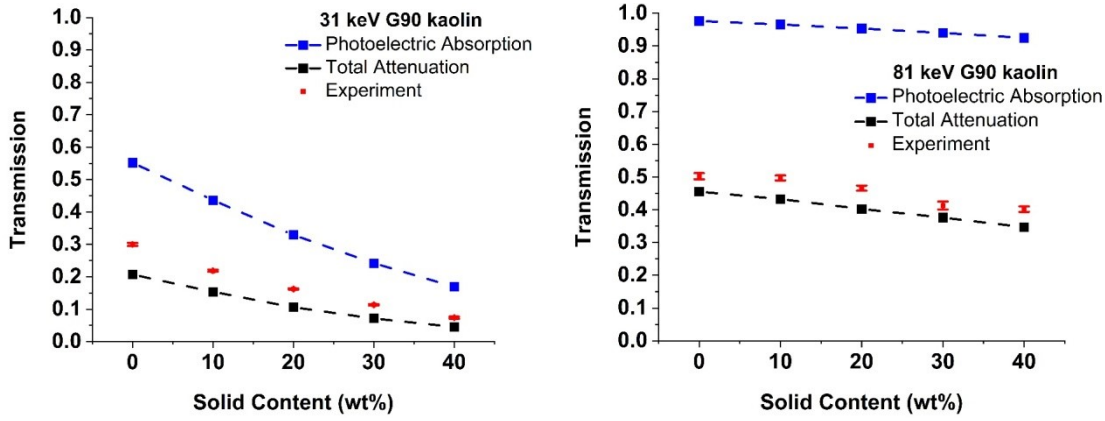

(a) 31keV **(b) 81keV**

Figure 5-3 – Measured normalized transmission of 31 keV and 81 keV and mass attenuation calculated transmission for G90 kaolin

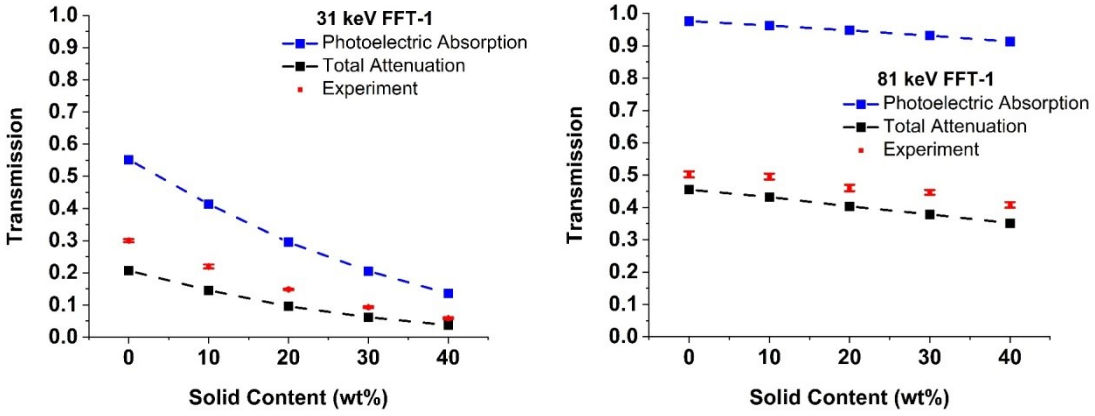

(a) 31keV **(b) 81keV**

Figure 5-4 – Measured normalized transmission of 31 keV and 81 keV and mass attenuation calculated transmission for FFT-1

5.2 GEANT4 Simulation Results and Discussion

5.2.1 Experimental and Simulated Results Comparison

Second order polynomial fits and linear fits were done for the normalized transmission and intensity ratios for the experimental results and simulated results calculated using GEANT4, as shown in Figure 5-5 for ^{241}Am and Figure 5-6 for ^{133}Ba. The simulated values of ^{241}Am show good agreement with experimental values of the 0.9 μCi ^{241}Am source. It can be seen that proper accounting of scattered X-ray / γ-ray photons and subtraction of background are required to obtain good agreement between the experimental and calculated values. For FFT-1 samples, some offset was seen at diluted concentrations, which is possibly caused by the inhomogeneity of sample solution as the sample thickness is only 1 cm. The big error bars are mainly caused by the low strength source, low emission probability of 17.8 keV and short measurement time. Compared with the 0.9 μCi ^{241}Am results, the emission probability for the ^{133}Ba source of 31 keV is much higher than that of the 17.8 keV, and the measurement time is increased to 30 minutes. So, the error of the average of the normalized transmission is relatively reduced, and agreement between the experimental and simulated results is improved, as shown in Figure 5-6.

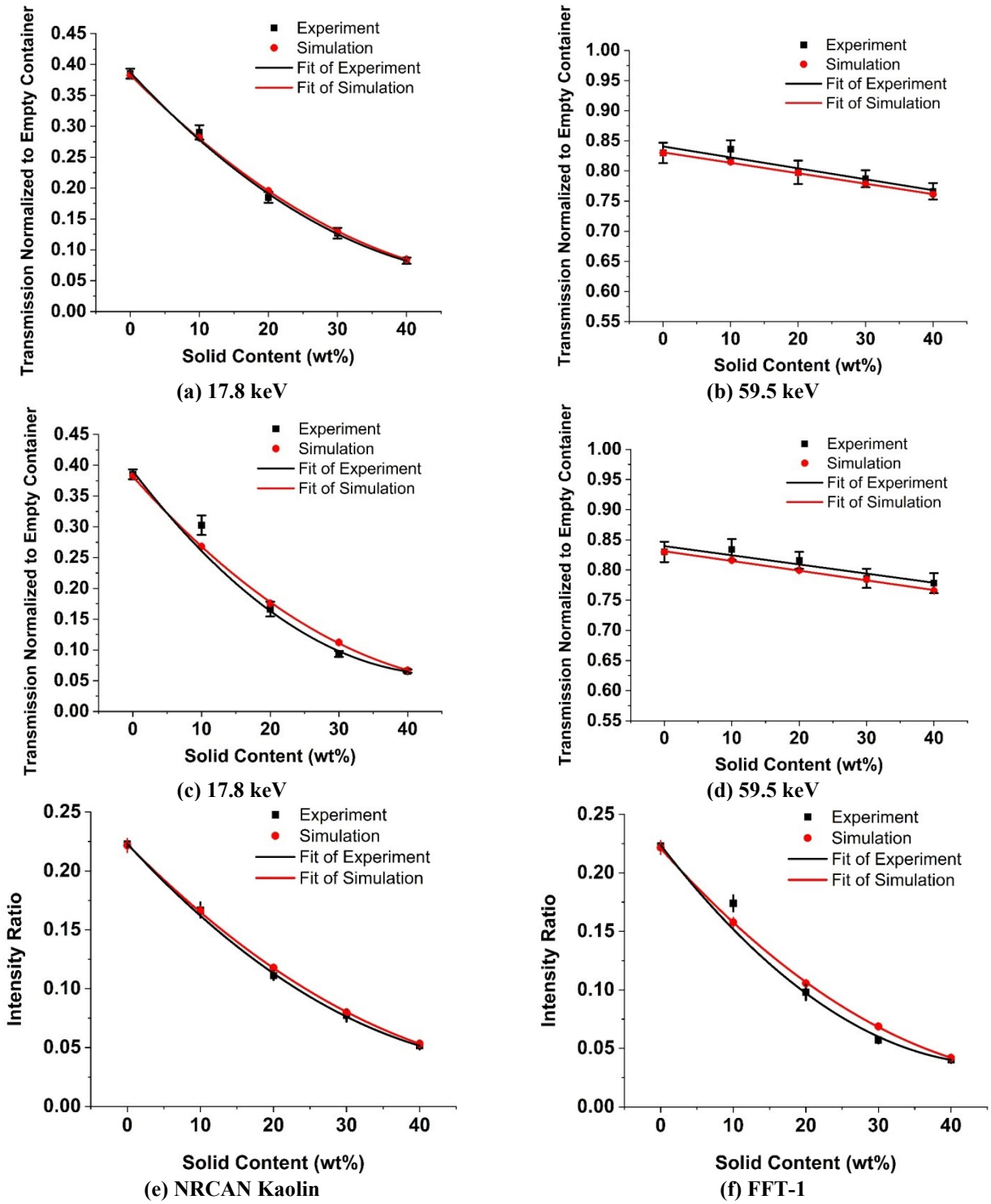

Figure 5-5 – Comparison between the experimental and simulated results for 0.9 µCi ^{241}Am. Normalized transmission of 17.8 keV for (a) NRCAN kaolin (c) FFT-1; Normalized transmission of 59.5 keV for (b) NRCAN kaolin (d) FFT-1; Intensity ratio of (e) NRCAN kaolin (f) FFT-1

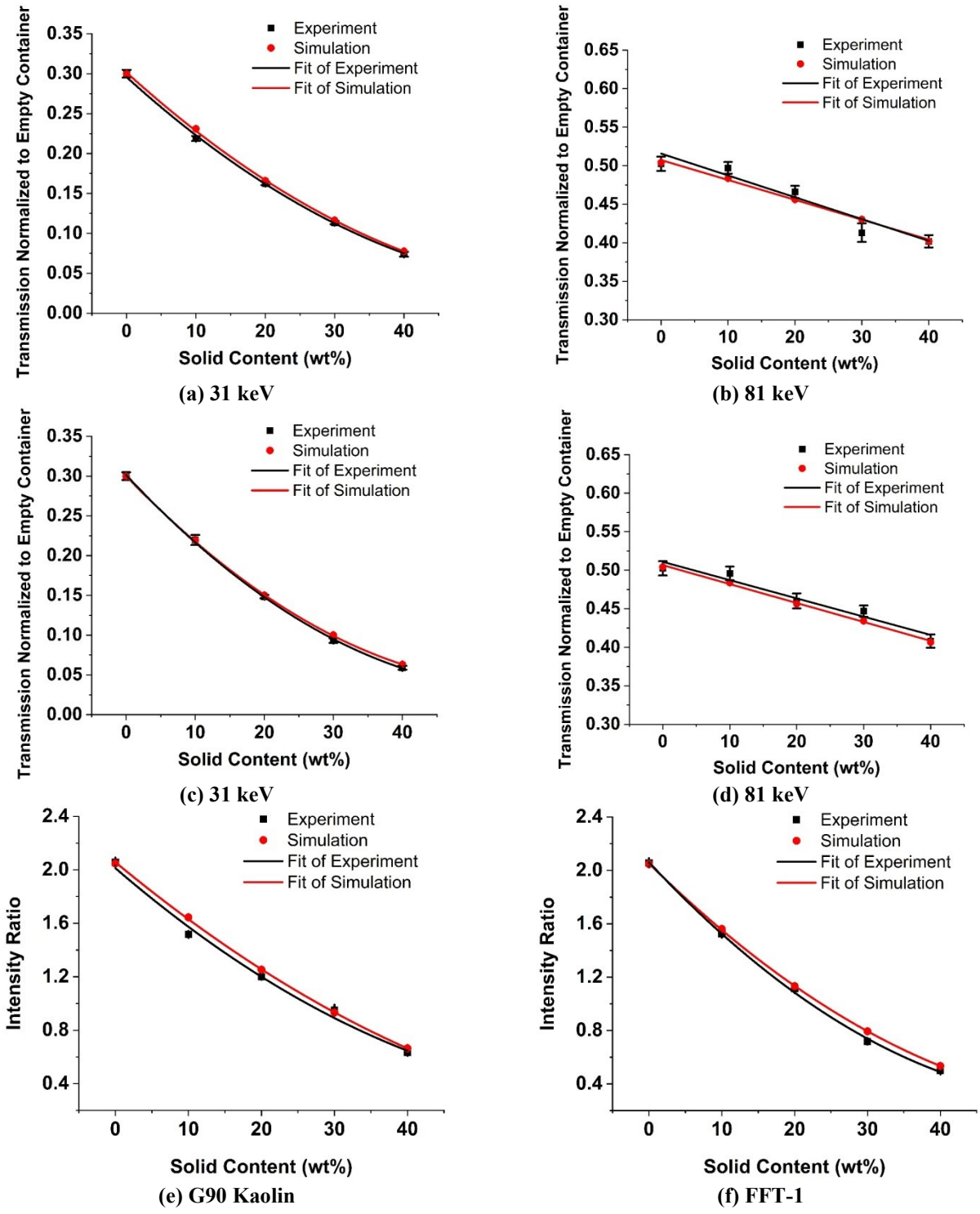

Figure 5-6 – Comparison between the experimental and simulated results for 1 µCi ^{133}Ba. Normalized transmission of 31 keV for (a) G90 kaolin and (c) FFT-1; Normalized transmission of 81 keV for (b) G90 kaolin and (d) FFT-1; Intensity ratio for (e) G90 kaolin and (f) FFT-1

5.2.2 Effect of ICP-MS Measurement Error

A key input parameter in this simulation is the chemical composition of the sample. The effect of the ICP-MS measurement error on the simulation results was evaluated. The upper and lower limits of chemical composition were calculated according to the relative standard deviation for each element estimated in 2.7.2, as shown in Table 5-5, and were used as the input of simulation. Each run was repeated 5 times with different random seeds to obtain the average and the error bar. The corresponding upper and lower limits of normalized transmission and intensity ratio for FFT-1 solutions were obtained and plotted in Figure 5-7. It is seen that the error of ICP-MS measurement causes more uncertainty on the simulated transmission of 31 keV than that of 81 keV since the lower energy is more sensitive to the variation of the chemical composition. According to the upper and lower limits shown in Figure 5-7 (e) and (f), each intensity ratio measured in experiment can lead to a corresponding solid content wt% variation range on the horizontal axis. The upper and lower limits of this range were calculated and are shown in Tables 5-6 and 5-7 for G90 kaolin and FFT-1 solutions. It is seen that the effective error due to errors in composition increases as the wt% of the solid content increases. However, the error is still within ± 2 wt% for samples from 0 wt% to 40 wt%. Thus, the ICP-MS sample composition error does not cause a serious effect on the accuracy of the simulation results, but it should be taken into consideration during the prediction of solid content wt% based on the intensity ratio curve. If the experimental intensity ratio data points match perfectly with the simulated curve, the variation calculated here will be the predicted range of solid content wt% in these samples. However, the variation should be larger since the real measurement situation is more complicated, possibly with variations in the composition of the clay particulates. A detailed prediction process in the following section will show how to determine the solid content wt% based on measured intensity ratios.

	Element	Al	Si	Fe	Ca	K	Ti	Mg	O	H
G90 kaolin	**Upper Limit**	21.246	22.710	0.686	0.356	0.138	0.441	0.023	52.918	1.482
	Lower Limit	19.349	21.481	0.617	0.172	0.124	0.376	0.020	56.286	1.576
FFT-1	**Upper Limit**	11.009	26.202	1.961	0.987	2.063	0.473	0.569	55.190	1.545

	Lower Limit	10.026	24.784	1.762	0.476	1.851	0.403	0.499	58.559	1.640

Table 5-5 – Upper and lower limits of the chemical compositions of G90 kaolin and FFT-1 (wt%) (Calculated according to Table 2-10.)

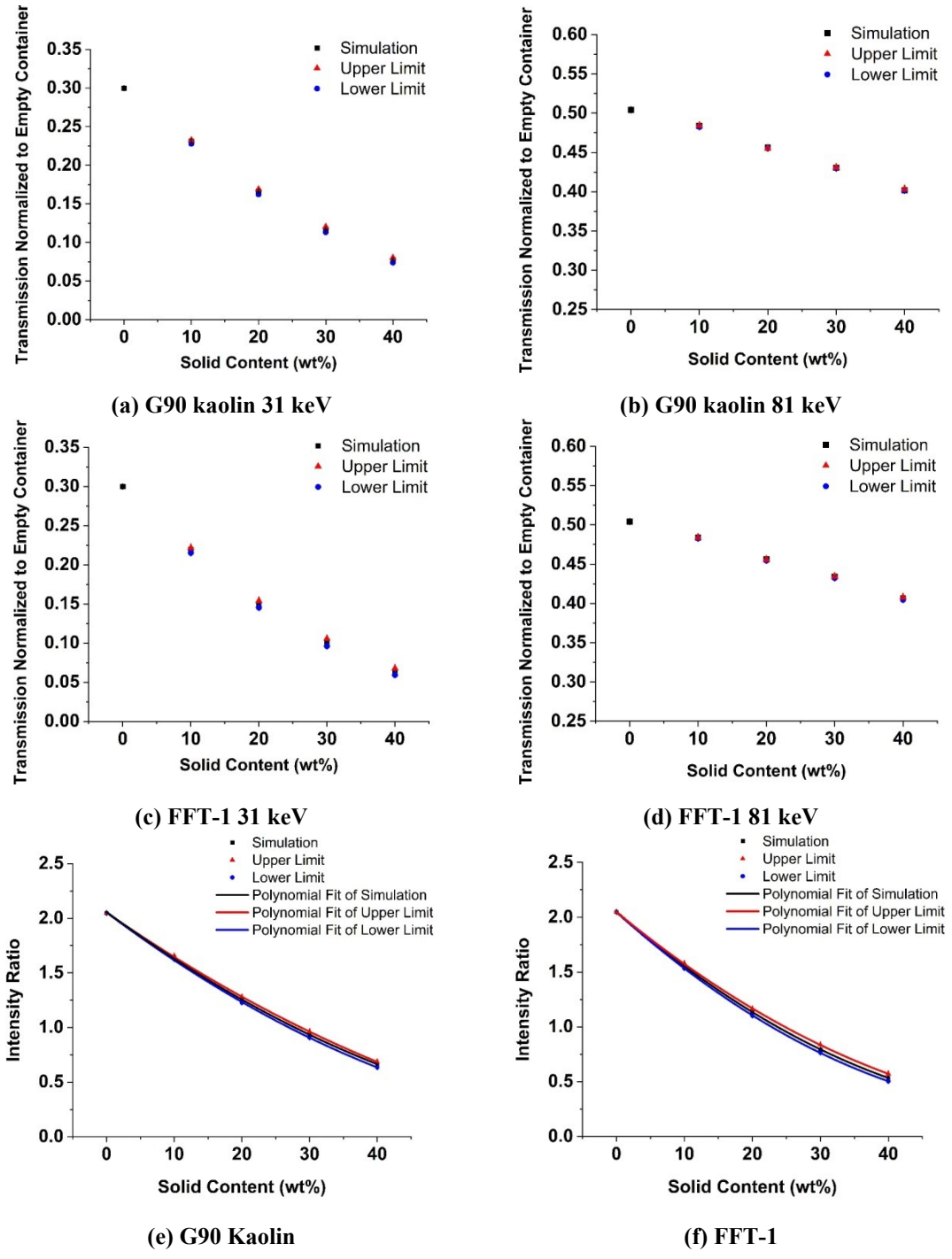

(a) G90 kaolin 31 keV **(b) G90 kaolin 81 keV**

(c) FFT-1 31 keV **(d) FFT-1 81 keV**

(e) G90 Kaolin **(f) FFT-1**

Figure 5-7 – Upper and lower limits of simulated normalized transmission of 31 keV: (a) G90 kaolin (c) FFT-1 and 81keV: (b) G90 kaolin (d) FFT-1; and simulated intensity ratio of 31 keV and 81 keV: (e) G90 kaolin and (f) FFT-1

	Solid Content wt% of G90 kaolin			
	10	**20**	**30**	**40**
Lower Limit	9.6409	19.3746	29.1002	38.8123
Upper Limit	10.391	20.7584	30.9366	40.8254

Table 5-6 – Variation of predicted solid content wt% of G90 kaolin caused by ICP-MS errors

	Solid Content wt% of FFT-1			
	10	**20**	**30**	**40**
Lower Limit	9.559	19.2477	28.9447	38.659
Upper Limit	10.4349	20.9253	31.364	41.6978

Table 5-7 – Variation of predicted solid content wt% of FFT-1 caused by ICP-MS errors

5.2.3 Prediction of Solid Content wt% of FFT

The solid content detector is designed for long-term use without frequent laboratory calibration. It is assumed that the chemical composition of the solid content in a large tailings pond will not vary much during the settling process. Before the implementation of the solid content sensor, ICP-MS measurement will be done for the sample from the tailings pond. The density of samples diluted in different wt% will also be measured. Then GEANT4 simulation will be done based on the chemical composition and measured density. After that, the prediction curve of intensity ratio versus solid content wt% such as Figure 5-7 (e) and (f) will be built, and the design of the solid content sensor can be finalized and packaged for installation in real tailings ponds. Once an intensity ratio is obtained by the sensor, the upper and lower limit curves can predict the possible wt% range for measured FFT. The experimental data of the 1 μCi ^{133}Ba for FFT-1 were plotted with the upper and lower limit curve of simulation in Figure 5-7 (f), to show an example in Figure 5-8. The average of intensity ratios can find a corresponding range in wt% using the two limits curves. The upper and lower limits of this range were shown in Table 5-8, which is the predicted solid content wt% results for the measured sample. It is seen that the prediction tends to overestimate the solid content wt%, which is caused by a difference between the experimental and simulation results, but the error is within the error bars. The highest error was seen at 30 wt% where the upper limit is 4.1 wt% higher than the real value. The errors of experiment, simulation and ICP-MS measurement were all considered in this prediction. It is seen that the prediction accuracy can be improved by reducing the experimental errors, increasing the accuracy of the chemical composition measurement, and optimizing the simulation codes to matching the experimental results. In the actual implementation, an inexpensive detection system will be developed using

lower resolution detectors. The model could be different, but the prediction procedures and key behavior are expected to be similar.

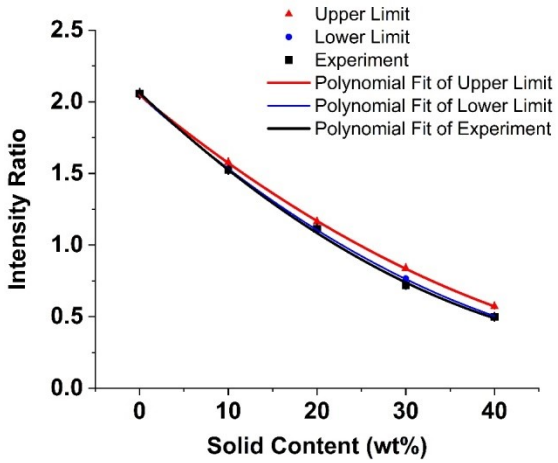

Figure 5-8 – An example on prediction of solid content wt% of FFT-1 using experimental results of the 1 µCi ^{133}Ba source measured for 30 minutes

Decision Range	Solid Content wt% of FFT-1				
	0	10	20	30	40
Lower Limit	-0.202	10.172	19.805	31.493	40.237
Upper Limit	-0.169	11.100	21.528	34.091	43.355

Table 5-8 – Decision range of solid content wt% of FFT-1 predicted based on measured intensity ratio

5.2.4 Simulations using Different Chemical Compositions of Clay

The prediction made by this technique is currently dependent on the accurate ICP-MS composition analysis and density measurement. An exploration was made to see how much each element in the FFT affects the attenuation and the sensitivity of the predicted results to the actual clay composition for two types of clay. GEANT4 simulations were run using the chemical compositions calculated according to the chemical formulas of kaolin and illite, as shown in Table 5-9. The density of samples at each wt% was assumed to be the same as the measured density of FFT-1 to compare the transmission difference caused by different chemical composition of clay. Each run was repeated 5 times with different random seeds to obtain average and the error bar. The main chemical composition of the clay group in FFT are kaolin and illite, but the wt% ratio of these two clays varies in different mining areas. Considering only kaolin and illite, two transmission limits were formed for 31 keV and 81 keV in the simulation results, as

shown in Figure 5-9. The calculated chemical compositions of these two clays and the ICP-MS results of FFT-1 were plotted in Figure 5-10 (a). The product of mass attenuation coefficient at 31 keV and the corresponding wt% of each element in the two formulas was plotted in Figure 5-10 (b). It is seen that some elements that are in low weight percent contribute a large portion of attenuation to X-rays / γ-rays, such as Fe and K, as their mass attenuation coefficients are relatively large. It indicates that the simulation results were highly dependent on the chemical composition of FFT especially elements with high atomic number, which limits the flexibility of this technique when it is applied to different tailings ponds with different FFT chemical compositions without ICP-MS and density measurement. Thus, for real applications it will be important to carry out an elemental analysis of the chemical composition of the FFT if model calculations are to be carried out for the instrument. Conversely, if the wt% is measured for a sample then the X-ray / γ-ray measurement can give a measure of the ratio of kaolin to illite in the FFT or oil sands samples based on the calculated attenuation curves.

Sample	Element						
	Al	Si	Fe	K	Mg	O	H
	wt%						
Kaolin	20.9029	21.7582	0	0	0	55.7770	1.56185
Illite	22.9734	15.9423	15.8501	5.54844	6.89830	31.7861	1.00133

Table 5-9 – Chemical compositions of kaolin and illite calculated according to chemical formulas

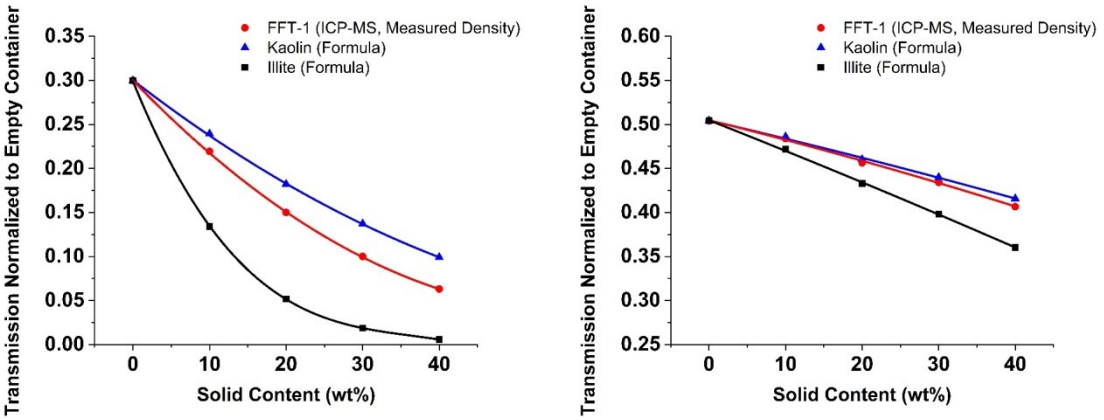

(a) 31 keV **(b) 81 keV**

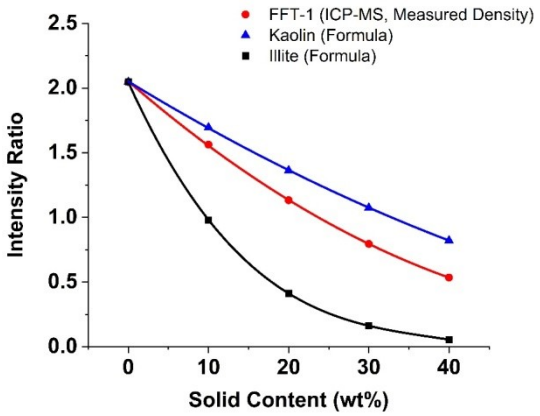

(c) Intensity Ratio

Figure 5-9 – GEANT4 simulation results for kaolin, FFT-1 and illite samples with different solid content wt%: The normalized transmission of (a) 31 keV and (b) 81 keV; (c) Intensity ratio. The chemical compositions of kaolin and illite were calculated by using the chemical formulas. For FFT-1, the ICP-MS result was used. The density of samples at each wt% was assumed to be the same with the measured density of FFT-1.

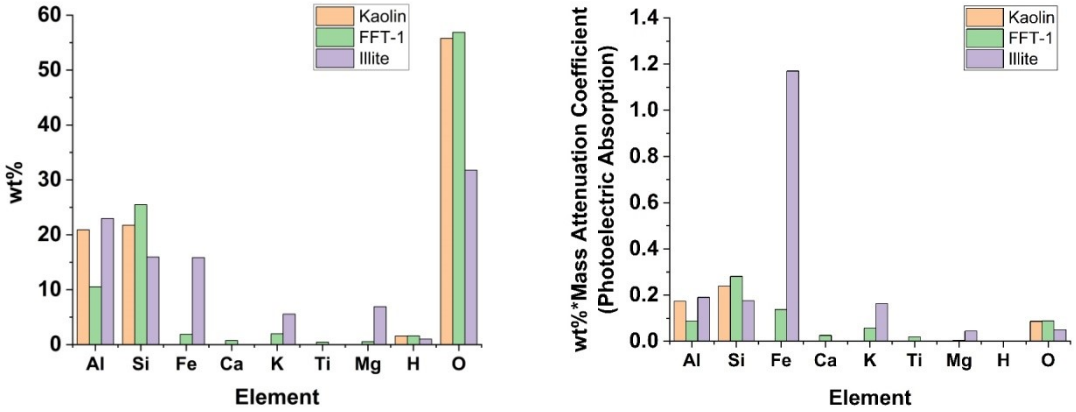

(a) **(b)**

Figure 5-10 – (a) Calculated chemical compositions of kaolin and illite, and the ICP-MS result of FFT-1; (b) Product of mass attenuation coefficient (Photoelectric absorption) at 31 keV and the corresponding wt% of each element in the chemical formulas of kaolin and illite, and in the ICP-MS result of FFT-1

5.3 Summary

Mass attenuation coefficients of the main elements in three samples at different concentrations were calculated based on the chemical composition results from ICP-MS measurement. The effects of ^{241}Am peak overlap and residual bitumen on X-ray / γ-ray attenuation results were evaluated to be small. The predicted transmission was calculated using two different limits of observing all photons transmitted through the sample or only observing the non-scattered photons reaching the detector, which formed upper and lower

limits on the measured signals. The experimental results were between these two limits. The scattering property of photons in these samples was observed. GEANT4 simulations were then used to further verify the experimental results by considering all the geometric factors. The simulated results for all the energy are in good agreement with the experimental results. It is also seen that proper accounting for scattered photons can improve the modeling accuracy. It has been shown that the variation of predicted solid content wt% based on the simulation results caused by ICP-MS errors is within ± 2 wt% from 0 wt% to 40 wt% for G90 kaolin and FFT-1 solutions. The results indicate that the ICP-MS measurement error has minor effect on accuracy of the predictions made by the simulation results. Predictions on solid content wt% were made using the experimental intensity ratios and the simulated upper and lower limit curves of ^{133}Ba. The highest error shown at 30 wt% FFT-1 is 4.1 wt% higher than the real value. However, simulations using the standard chemical formula of kaolin and illite show that composition measurements by ICP-MS are necessary for accurate modeling simulation before the implementation of the detector, and, in turn, this technique has the potential to distinguish tailings with different clay chemical compositions.

6. Observation in Settling Tank

6.1 LYSO Detection System

An inexpensive detector that consists of a Cerium-doped LYSO scintillator and an MPPC was built in the laboratory for implementation in the settling tank. The dimensions of the LYSO crystal (X-Z LAB, Inc.) are 5 mm × 5 mm × 1 mm. The light yield is 20 ~ 30 photons per keV. The emission peak is at 420 nm. An MPPC (S13360-6050CS, HAMAMATSU) was used to collect the scintillation. It is a type of silicon photomultipliers that consists of multiple Geiger mode avalanche pixels. The pixel inch is 50 μm. The effective photosensitive area is 6 mm × 6 mm. The main wavelength range of LYSO scintillation is between 400 nm and 500 nm [47]. In this range, the photo detection efficiency of this MPPC is between 35 % and 40 %, and 40 % is also the maximum efficiency it can reach [30]. The LYSO crystal and the MPPC were placed closely to each other to make a new detector, as shown in Figure 6-1. The thickness of the LYSO crystal along the X-ray / γ-ray transmitting direction is 1 mm. They were wrapped by Teflon tape, which increases the detection efficiency by collecting the photons traveling to other directions instead of the MPPC detection surface. The adhesive tape was used as a protection layer for the detector package.

The schematic of the detection system is shown in Figure 6-2. The operating voltage of the MPPC was set to be 54.3 V. A bias box was used to power the MPPC and pass the signal to the pulse shaper. The pulse shaper is the CR-160-R7 evaluation board with CR-200-8μs shaping amplifier module from Cremat Inc. It also needs a ± 12 V power supply. The shaping time is 8 μs, and the FWHM of the out pulse is 19 μs. When the LYSO crystal receives a radiation photon, the scintillation will be emitted, and then collected by the MPPC. The output of the MPPC is a voltage pulse. The pulse shaper will amplify this pulse and pass it to a multichannel analyzer, and then a count will be recorded in the spectrum. The multichannel analyzer was developed using the internal ADC of an STM32F334R8T6 microcontroller on the Nucleo development board (STMicroelectronics N.V.). Once a trigger threshold is reached, the data points in the duration of one pulse sampled by the internal ADC were added up to characterize the

pulse. The data were collected and sent to a laptop using a TTL to serial port converter, FT232RL (FTDI Chip).

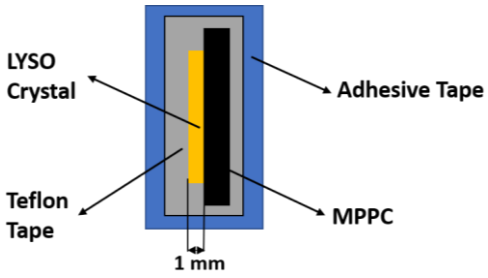

Figure 6-1 – Schematic of the LYSO detector

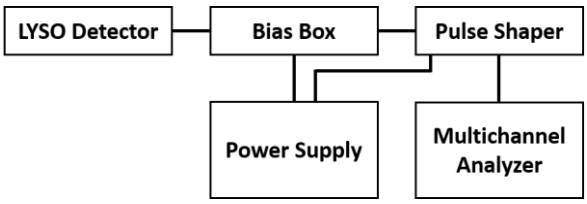

Figure 6-2 – Schematic of the LYSO detection system

6.2 Experiment Setup

A settling tank setup was built to simulate the detector implementation in the real tailings pond, as shown in Figure 6-3. The inner dimensions of the settling tank are Ø 30 cm × 30 cm. The same 1 μCi ^{133}Ba source was used for the calibration tests above. The source and LYSO detector were placed in plexiglass holders on two metal rods, and aligned according to the scale marked on the rods. The rods were placed in two plexiglass circular tubes which protrude down into the settling pond solution. The centers of the source and the detector are at the depth of 6.8 cm below the liquid surface. The wall thickness of the tube is 3.5 mm. The distance between the source and detector is 77 mm. The bottom of the tubes were sealed and fixed at the bottom of the settling tank. The detection zone between the tubes was filled with 20 wt% fast settling kaolin sample, ASP 802 (BASF SE). The minimum sample thickness between the two tubes is 41 mm.

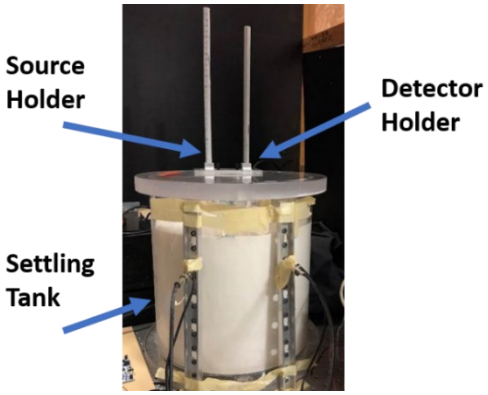

Figure 6-3 – Experiment setup built based on a large settling tank

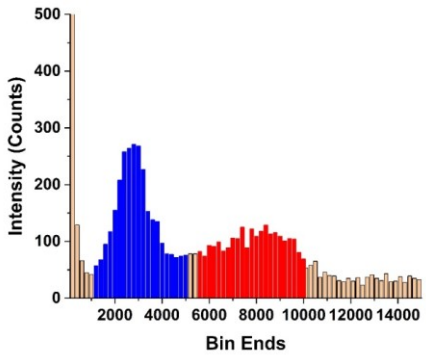

Figure 6-4 – ^{133}Ba spectrum of the first 10-minute measurement using the inexpensive LYSO detection system

6.3 Results and Discussion

The detection system was turned on right after the settling tank was filled by the kaolin sample. The data were saved every 10 minutes as an .xlsx file and split into a histogram with a fixed bin width, 200. The first 10-minute result is shown in Figure 6-4. Two peaks were found in the spectrum. The main component of the higher peak at bin number around 2800 should be the 31 keV emission according to the emission probability, but it also contains contributions from other peaks such as the smaller 35 keV peak and part of the 81 keV peak as the resolution of this detection system is very low. Another lower peak in the spectrum at around bin number 8000 is mainly formed by the 81 keV photons with some background from higher energy.

The intensity of the lower energy peak and higher energy peak were calculated by selecting fixed range of bin end number, shown as blue and red areas in Figure 6-4, and the results were plotted in Figure 6-5 (a) and Figure 6-5 (b). The intensity ratio of lower energy peak area divided by the higher energy peak area was calculated and plotted in Figure 6-5 (c). The intensity of the lower energy peak kept increasing in the first 4 hours and then reached a stable level. After 24 hours, no obvious change was observed. After 74 hours, the intensity of the two peaks were both lower than the previous values, which indicates a lower counting rate. This was possibly caused by the connection problem of the jumpers on the development board. The intensity ratio shows a constant increasing trend in 74 hours and then remains stable. The measurement results show good characterization for the settling process of the kaolin sample. The fluctuations shown in these figures show that the detection system still needs to be optimized to improve the repeatability of the results.

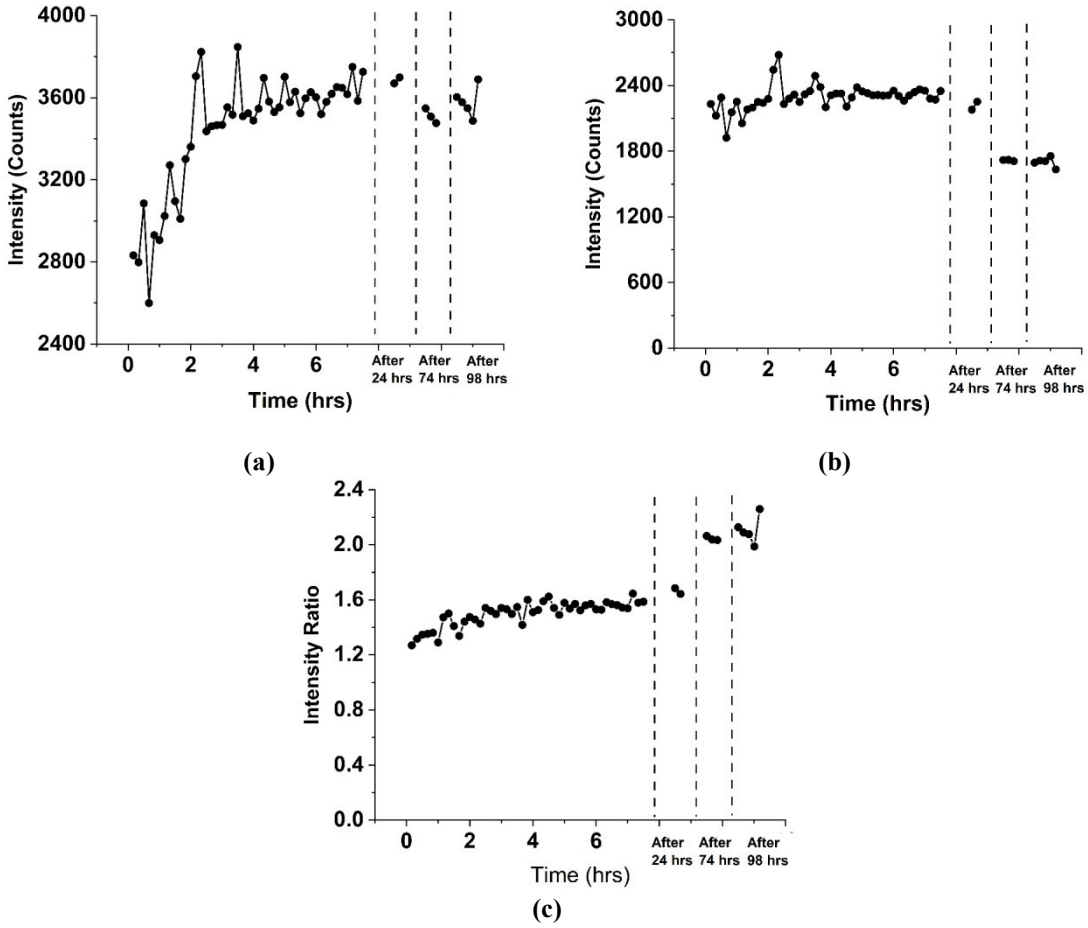

Figure 6-5 – LYSO detection system results for the settling tank filled with 20 wt% fast-settling kaolin (a) Lower energy peak intensity (b) Higher energy peak intensity (c) Intensity ratio of the lower energy peak divided by the higher energy peak

6.4 Summary

The settling tank experiment shows that the preliminary implementation of an inexpensive and portable detection system can characterize the settling process effectively in a working environment similar to the tailings ponds. As a preliminary design, the counting rate of the detection system is not stable due to the connection problem, so the repeatability of the experimental results is still poor. This homemade detection system still needs to be optimized and calibrated for real solid content measurements. However, it is shown that such a simple detector geometry is sensitive enough to measure the solid content in a settling pond type environment and is small enough to fit into measurement tubes inserted into settling ponds.

7. Conclusions & Future Directions

In this thesis, a study was carried out of a technique to measure solid content in fluid fine tailings using low level X-ray sources. An experimental setup based on an Amptek detection system was built to evaluate the performance of a 0.9 μCi ^{241}Am source and a 1 μCi ^{133}Ba source for use in settling pond measurements. In order to reduce sensitivity to varying source strengths and background conditions the ratio of transmission of a low energy X-ray line to a high gamma ray energy was used as the measurement indicator for solid density. Comparative studies were carried out using samples of kaolin clay and FFT samples from mining sites at various wt% mixtures in water. Using measurement times of 10 to 30 minutes, accurate and repeatable results were obtained verifying the feasibility of this technique in monitoring solid content in FFT. An accuracy of the order of 3 % in transmission ratio of X-ray and γ-ray was obtained leading to a good accuracy in solid content measurement.

In order to accurately predict the results numerical modeling of the exact measurement geometry is required due to the significant contribution of scattered X-rays / γ-rays to the measured signal, particularly at higher X-ray / γ-ray energies. Modeling was carried out using the GEANT4 simulation code. Good agreement was seen between the experimental, calculated, and simulated results.

Prediction of solid content in FFT using the simulation curves was performed. With properly measured sample density and ICP-MS calibration results, the largest error in measurement was 4.1 wt% for FFT samples over the range of 0 to 40 wt%. The average error in measurement was on the order of 2 wt%. It has been shown that this system can predict solid content wt% of FFT within several percent based on the measured intensity ratio. Solutions to common issues and discussion on key parameters in the experimental methodology were presented and can be generalized and applied to measurement systems with different sources and detection systems.

In the future, more details of the CdTe detector including the interactions between the X-ray / γ-ray photons and the detector material can be modeled by GEANT4 simulation, which would help improve the matching between experimental and simulated results to increase the prediction accuracy. A preliminary design of an inexpensive homemade

detection system based on LYSO scintillation crystals and MPPC detectors was developed. A preliminary initial test of this system was carried out and presented in the thesis. The counting rate and signal to noise ratio of this system still need improvement. More experiments and calibration measurements are required to characterize and optimize this detector system. A GEANT4 model of the detector system would also be very useful in order to model the experimental results and gain more understanding about this detector for further optimization. A compact electronic circuit including pulse amplifiers, shaper, and microprocessor on one board should be developed to make a robust system. Since the measurement accuracy is ultimately limited by photon counting statistics, with optimization, it is expected that such an inexpensive homemade detection system should be able to achieve comparable performance to those obtained here with the commercial CdTe detection system. This simplified detection system should be tested in a large-scale tailings tank for long-period tests and after further evaluation and optimization, it could be implemented in real tailings ponds.

Bibliography

[1]. Government of Alberta. " Oil sands facts and statistics ". Government of Alberta, 2019. [Online]. Available: https://www.alberta.ca/oil-sands-facts-and-statistics.aspx

[2]. British Petroleum Company. " BP Statistical Review of World Energy ". British P etroleum Company, June 2018. [Online]. Available: https://www.bp.com/content/dam/bp /business-sites/en/global/corporate/pdfs/energy-economics/statistical-review/bp-stats-revi ew-2018-full-report.pdf

[3]. Alberta Oil Sands Technology and Research Authority (AOSTRA). " A 15 Year P ortfolio of Achievement Edmonton ". Alberta Oil Sands Technology and Research Autho rity (AOSTRA), 1990, p.54

[4]. Alberta Energy Regulator. " Directive 085 ". Alberta Energy Regulator, October 2 017. [Online]. Available: https://aer.ca/documents/directives/Directive085.pdf

[5]. Li, Min, S. Lee Barbour, and Bing Cheng Si. " Measuring solid percentage of oil s ands mature fine tailings using the dual probe heat pulse method ". Journal of environmen tal quality 44.1 (2015): 293-298.

[6]. Skoog, Douglas; West, Douglas M; Holler, F James . "5: Gravimetric Analysis" in Fundamentals of Analytical Chemistry 7th Edition (Philadelphia: Saunders College Pub, 1996), 71-96.

[7]. Dean, E. W., and Stark, D. D. "A Convenient Method for the Determination of W ater in Petroleum and Other Organic Emulsions." Industrial & Engineering Chemistry 12. 5 (1920): 486-490.

[8]. Sella, A. "Classic Kit: Dean-Stark apparatus". Royal Society of Chemistry. [Onlin e]. Available: https:// https://www.chemistryworld.com/opinion/classic-kit-dean-stark-ap paratus/3004907.article

[9]. Li, An, and Zhenghe Xu. "Determination of clay content in Canadian oil sands usi ng x‐ray florescence spectroscopy for diagnosis of ore processability." The Canadian Jou rnal of Chemical Engineering 98, no. 1 (2020): 360-372.

[10]. Fahad, A. A. " A computer-controlled dual-gamma scanner for measurement of so il water content and bulk density ". International Journal of Radiation Applications and In strumentation. Part A. Applied Radiation and Isotopes 40.4 (1989): 340-342.

[11]. Alam, M. N., et al. " Attenuation coefficients of soils and some building materials of Bangladesh in the energy range 276–1332 keV ". Applied Radiation and Isotopes 54.6 (2001): 973-976.

[12]. Baytaş, A. Filiz, and Sevgi Akbal. " Determination of soil parameters by gamma-ray transmission ". Radiation Measurements 35.1 (2002): 17-21.

[13]. Appoloni, Carlos Roberto, and Walmir Eno Pottker. " Non-destructive porosity profile measurement of amorphous materials by gamma-ray transmission ". Applied Radiation and Isotopes 61.6 (2004): 1133-1138.

[14]. Kennedy, Gregory, Lincar Pedroni, and Michel Aubertin. " Density measurements during sedimentation of mine water treatment sludge and mine tailings using dual-source gamma-ray transmission ". Proceedings of the 12th Asian Pacific conference on Non-Destructive Testing. 2006.

[15]. De Groot, A. V., et al. " Sensitivity of in-situ γ-ray spectra to soil density and water content ". Nuclear Instruments and Methods in Physics Research Section A: Accelerators, Spectrometers, Detectors and Associated Equipment 600.2 (2009): 519-523.

[16]. Hendrickx, Roel, Staf Roels, and Koenraad Van Balen. " Measuring the water capacity and transfer properties of fresh mortar ". Cement and Concrete Research 40.12 (2010): 1650-1655.

[17]. Pease, Brad J., Gregor A. Scheffler, and Hans Janssen. " Monitoring moisture movements in building materials using X-ray attenuation: Influence of beam-hardening of polychromatic X-ray photon beams ". Construction and Building Materials 36 (2012): 419-429.

[18]. Al-Masri, M. S., et al. " Mass attenuation coefficients of soil and sediment samples using gamma energies from 46.5 to 1332 keV ". Journal of environmental radioactivity 116 (2013): 28-33.

[19]. Pires, L. F., and M. E. Medhat. " Different methods of mass attenuation coefficient evaluation: Influences in the measurement of some soil physical properties ". Applied Radiation and Isotopes 111 (2016): 66-74.

[20]. Taqi, Ali H., and Hero J. Khalil. " An investigation on gamma attenuation of soil and oil-soil samples ". Journal of radiation research and applied sciences 10.3 (2017): 252-261.

[21]. Priyada, P., M. Margret, and R. Ramar. " Intercomparison of gamma ray scatterin g and transmission techniques for fluid–fluid and fluid–air interface levels detection and density measurements ". Applied Radiation and Isotopes 70.3 (2012): 462-469.

[22]. Hanus, Robert, et al. " Identification of liquid-gas flow regime in a pipeline using gamma-ray absorption technique and computational intelligence methods". Flow Measur ement and Instrumentation 60 (2018): 17-23.

[23]. R.H. Petrucci, W.S. Harwood and F.G. Herring, General Chemistry 8th Edition (L ondon: Pearson, 2001), 1025-26

[24]. Bé, M. M., V. P. Chechev, and V. G. Khlopin. "Update of X Ray and Gamma Ra yDecay Data Standards for Detector Calibration and other Applications, Volume 2: Data Selection Assessment and Evaluation Procedures." (Vienna: International Atomic Energy Agency, 2007), 10.

[25]. Gilmore Gordon. Practical gamma-ray spectroscopy (Hoboken: John Wiley & So ns, 2011), 2.

[26]. Bé, M. M., V. P. Chechev, R. Dersch, O. A. M. Helene, R. G. Helmer, M. Herma n, S. Hlavác et al. "Update of x ray and gamma ray decay data standards for detector cali bration and other applications volume 1: recommended decay data, high energy gamma r ay standards and angular correlation coefficients." (Vienna: International Atomic Energy Agency, 2007), 3-10.

[27]. Michael F. L'Annunziata. " Chapter 4 - Alpha Radiation " in Introduction and Hist ory, from the Quantum to Quarks (Amsterdam: Elsevier, 2016), 191-231.

[28]. Ramaswamy, M. K., W. L. Skeel, and P. S. Jastram. "The decay energy of Ba133. " Nuclear Physics 19 (1960): 299-302.

[29]. Gilmore Gordon, " Semiconductor detectors for gamma-ray spectrometry " in Pra ctical gamma-ray spectroscopy (Hoboken: John Wiley & Sons, 2011), 39-59.

[30]. Hamamatsu Photonics K.K. " MPPC S13360 series ". Hamamatsu Photonics K.K. [Online]. Available:https://www.hamamatsu.com/resources/pdf/ssd/s13360_series_kapd 1052e.pdf

[31]. Knoll Glenn F. , " Scintillation Detector Principles " in Radiation detection and m easurement (Hoboken: John Wiley & Sons, 2000), 219-259.

[32]. Robert Redus. " AN-CdTe-1 Application Note ". Amptek Inc. [Online]. Available : https://www.amptek.com/internal-products/xr-100t-cdte-cadmium-telluride-detector-efficiency-application-note

[33]. Robert Redus. " Application Note ANCZT-2 Rev. 3 ". Amptek Inc., November 2017. [Online]. Available: https://www.amptek.com/internal-products/charge-trapping-in-xr-100t-cdte-cadmium-telluride-detectors-application-note

[34]. Amptek Inc. " Specifications of MCA-8000A Pocket Multi-Channel Analyzer ". Amptek Inc. [Online]. Available: https://www.amptek.com/-/media/ametekamptek/documents/resources/mca8000a.pdf?la=en

[35]. Amptek Inc. " MCA-8000D User Manual ". Amptek Inc. [Online]. Available: http://atomfizika.elte.hu/muszerek/Amptek/Documentation/User%20Manuals/MCA8000D%20User%20Manual.pdf

[36]. Gilmore Gordon. Practical gamma-ray spectroscopy. (Hoboken: John Wiley & Sons, 2011), 130.

[37]. Wilschefski, Scott C., and Matthew R. Baxter. " Inductively Coupled Plasma Mass Spectrometry: Introduction to Analytical Aspects". The Clinical Biochemist Reviews 40, no. 3 (2019): 115.

[38]. Syncrude Canada Ltd. " Tailings Management ". Syncrude Canada Ltd. , June 2018. [Online]. Available: https://www.syncrude.ca/environment/tailings-management/

[39]. Masliyah, J. H., J. Czarnecki, and Z. Xu. Handbook on theory and practice of bitumen recovery from Athabasca oil sands, volume 1: Theoretical basis (Canada: Kingsley Knowledge Publishing, 2011), 211-250.

[40]. Fan Chaojun, Joan Wu, Hongjie Xie, and Stuart Birnbaum. " Analysis of United States Geological Survey spectral library of silicate minerals: implication for remote sensing applications. " Journal of Applied Remote Sensing 6, no. 1 (2012): 063514.

[41]. Bearden, Joyce Alvin. "X-ray wavelengths." Reviews of Modern Physics 39, no. 1 (1967): 78.

[42]. Besra, L., D. K. Sengupta, and S. K. Roy. " Particle characteristics and their influence on dewatering of kaolin, calcite and quartz suspensions. " International Journal of Mineral Processing 59, no. 2 (2000): 89-112.

[43]. Canadian Nuclear Safety Commission. "Nuclear Substances and Radiation Device s Regulations. Ottawa." Nuclear Safety and Control Act: 2000-207.

[44]. Cunningham J. R. and Dance D. R. " Interactions of Radiation with Matter " in Di agnostic Radiology Physics: A Handbook for Teachers and Students (Vienna: Internation al Atomic Energy Agency, 2014), 11-32.

[45]. Berger, M. J., J. H. Hubbell, S. M. Seltzer, J. Chang, J. S. Coursey, R. Sukumar, D. S. Zucker, and K. Olsen. "XCOM: Photon Cross Sections Database, NIST Standard R eference Database 8 (XGAM)." [Online]. Available: https://www.physics.nist.gov/PhysR efData/Xcom/html/xcom1.html (2010).

[46]. Rahimi, Parviz M., and Thomas Gentzis. " The chemistry of bitumen and heavy oi l processing. " in Practical advances in petroleum processing (New York: Springer, 2006) , 597-634.

[47]. X-Z LAB, Inc. " LYSO(Ce) | Scintillation Crystal ". X-Z LAB, Inc. [Online]. Ava ilable: https://www.x-zlab.com/wp-content/uploads/2016/01/lyso-scintillation-x-z-lab201 6.pdf

Appendix A: Supplementary Data

This appendix includes the detailed calculated results for section 5.1.2 " Peak Overlap Evaluation for ^{241}Am ".

Spectrum	Peak Area		16.9 keV merged in 17.8 keV (%)		
	16.9 keV	17.8 keV		Average	Std
Water-1	148	3464	4.10		
Water-2	96	3484	2.68		
Water-3	74	3510	2.05	2.560	1.012
Water-4	95	3536	2.62		
Water-5	50	3644	1.35		
10M-1	69	2722	2.47		
10M-2	34	2579	1.29		
10M-3	37	2617	1.40	1.717	0.460
10M-4	46	2616	1.73		
10M-5	45	2584	1.70		
20M-1	10	1503	0.69		
20M-2	15	1596	0.93		
20M-3	24	1665	1.40	1.205	0.382
20M-4	27	1641	1.61		
20M-5	25	1752	1.40		
30M-1	10	929	1.10		
30M-2	14	990	1.39		
30M-3	11	919	1.22	1.559	0.735
30M-4	27	916	2.86		
30M-5	11	846	1.23		
40M-1	6	624	0.98		
40M-2	16	631	2.48		
40M-3	7	751	0.86	1.276	0.832
40M-4	10	568	1.72		
40M-5	2	561	0.34		

Table A-1 Peak area of 16.9 keV and 17.8 keV calculated by integrating fitted Gauss curves; Percentage of 16.9 keV area merged in selected area of 17.8 keV

wt%	Calculated Transmission (Photoelectric absorption)			Decrease	%	Std. (%)
	16.9 keV	17.8 keV	17.8keV with merged 16.9 keV			
0	0.348032	0.403756	0.402329	0.001426767	0.353373	0.13972
10	0.221965	0.27344	0.272556	0.000883995	0.323286	0.086585
20	0.130793	0.172929	0.172421	0.000507834	0.293667	0.093019
30	0.074395	0.106054	0.10556	0.000493587	0.465412	0.219378
40	0.038865	0.060421	0.060146	0.000274999	0.455141	0.29696

Table A-2 Mass attenuation calculation (Photoelectric absorption) results of 1 cm FFT-1 samples for 16.9 keV, 17.8 keV and 17.8 keV with merged 16.9 keV; Decrease of the transmission of 17.8 keV caused by the overlap with 16.9 keV

Appendix B: Drawings

This appendix includes drawings of the aluminum measuring block and holders for 0.9 µCi ^{241}Am and 10 µCi ^{241}Am sources.

Drawings of ^{241}Am Experiment Setup

Measurement Holder Block (Material: Aluminum; Unit: mm)

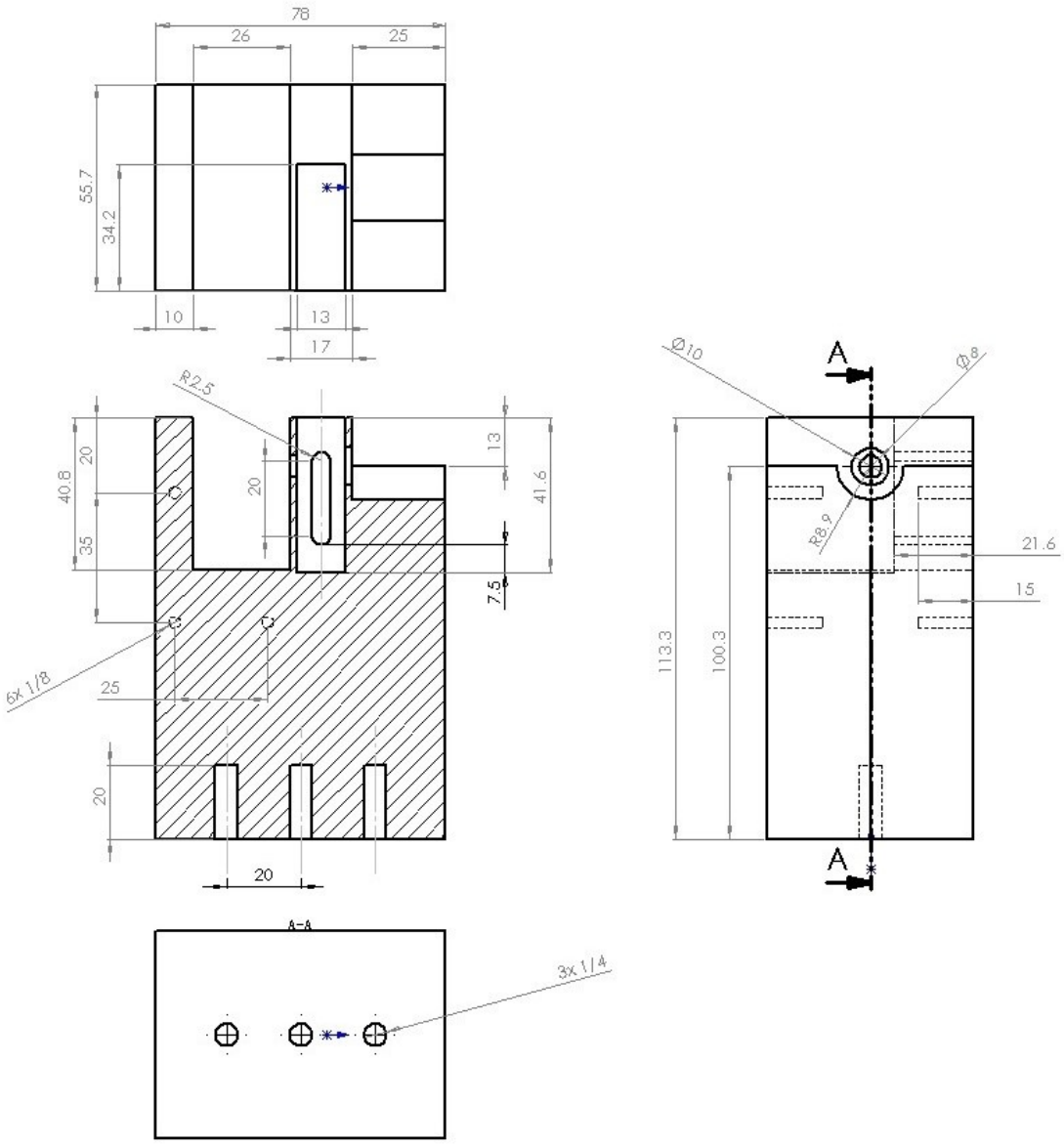

Base of Measurement Block (Material: Aluminum; Unit: mm)

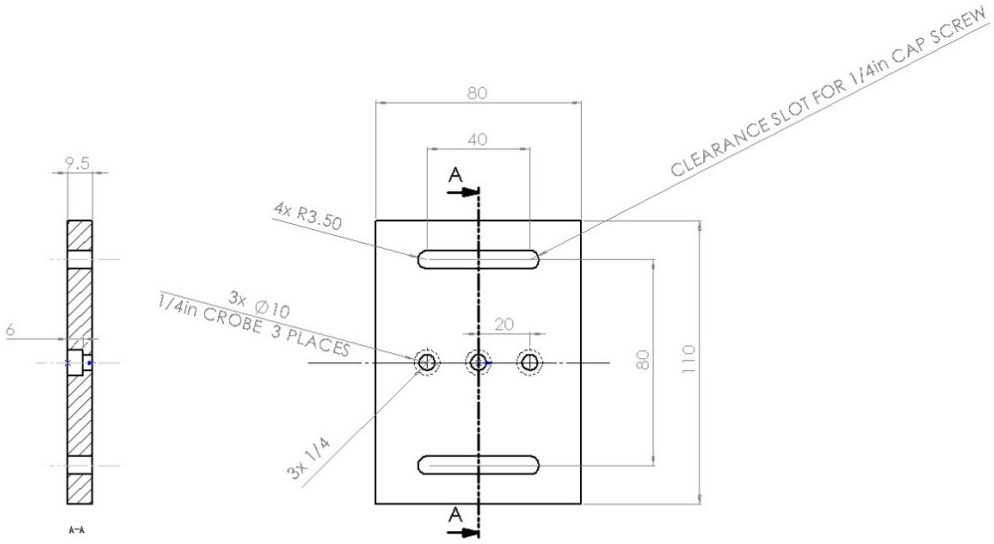

Side Wall of Measurement Block (Material: Aluminum; Unit: mm)

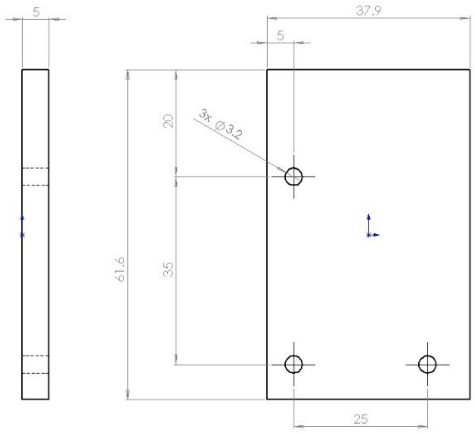

Holder (Front) for 0.9 μCi ^{241}Am source (Material: PVC; Unit: mm)

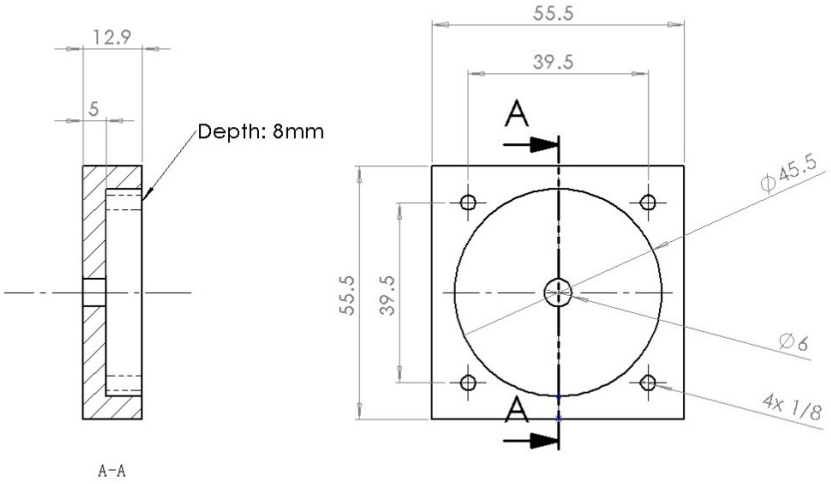

Holder (Back) for 0.9 µCi ^{241}Am source (Material: PVC; Unit: mm)

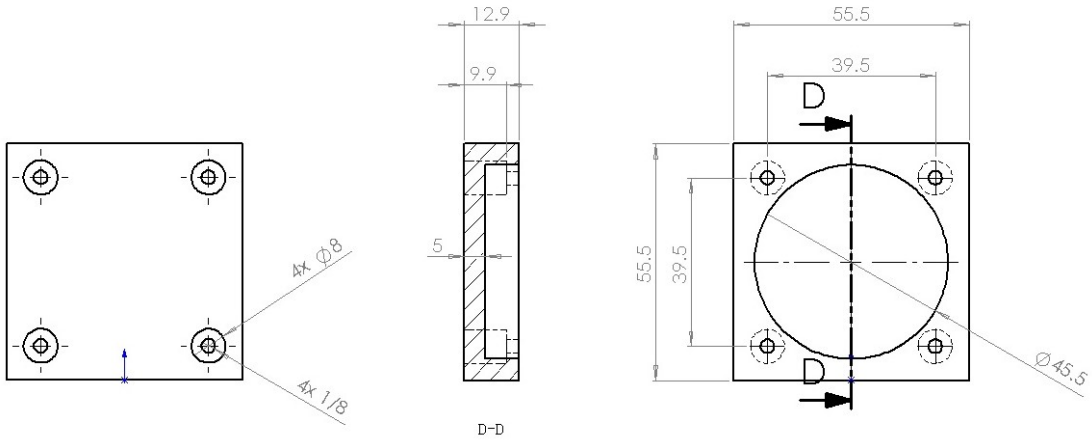

Holder (Front) for 10 µCi ^{241}Am source (Material: PVC; Unit: mm)

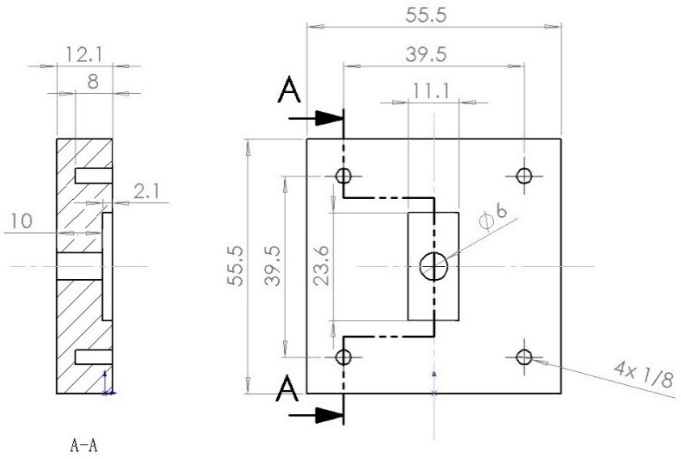

Holder (Back) for 10 µCi ^{241}Am source (Material: PVC; Unit: mm)

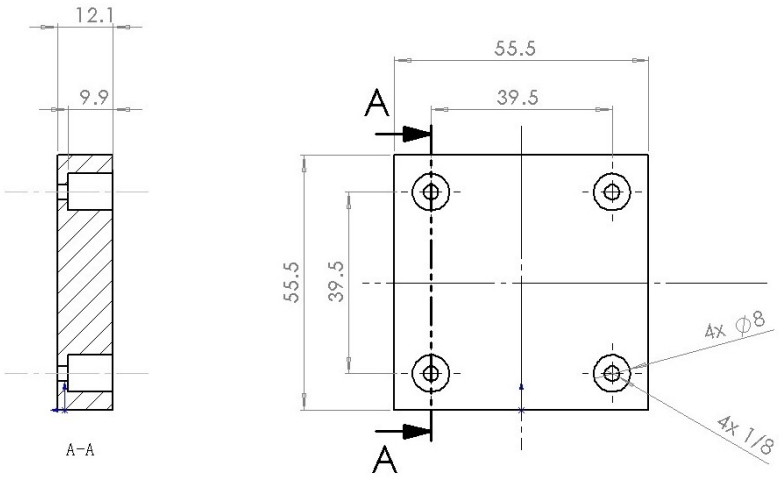

Appendix C: Codes

This appendix includes the Python code for processing the spectra, the C++ code for running GEANT4 simulations, and the C code generated by STM32CubeIDE for programming the internal ADC of the STM32F334R8T6.

Python Code for Data Processing

```
import math
import glob
import errno
import mcareader as mca
import os
import matplotlib.pyplot as plt
import numpy as np
from scipy.integrate import simps
from numpy import trapz
from scipy.interpolate import UnivariateSpline as spline
import time
from scipy.signal import argrelextrema
import pandas as pd
from astropy import modeling
from scipy.stats import norm

# Record the start time
start = time.time()
# Insert the path of the spectrum file here
path = " "
# Insert how many files are under the path
n = 1
count = 0
tcount = 0
# Save all data to csv
df_2 = pd.DataFrame([])
df_2_local = pd.DataFrame([])
# Add file type as ".mca" here
files = sorted(glob.glob(path + '\*.mca'))
for name in files:
    try:
        with open(name) as f:
            pass
            s = mca.Mca(name)
            x, y = s.get_points(calibration_method=None, trim_zeros=False, background=None)
            # Energy Range and Background Channel Number
            ini_l_1=491
            ini_r_1=610
            bg1_l_1=611
            bg1_r_1=620
            # Adjustment for the numbering of arrays
            x1=x[ini_l_1:ini_r_1+1]
            y1=y[ini_l_1:ini_r_1+1]

            x_bg1_1=x[bg1_l_1:bg1_r_1+1]
```

```
            y_bg1_1=y[bg1_l_1:bg1_r_1+1]
            # Plotting the spectrum
            plt.figure()
            plt.plot(x1, y1)

            plt.xlim([ini_l_1,ini_r_1])
            plt.ylim([0,100])

            plt.ylabel('counts')
            plt.xlabel('Channels')

            plt.ylabel('counts')
            plt.xlabel('Channels')

            if count == 0:
               df_2_local = pd.DataFrame([])
               df_3_local = pd.DataFrame([])
            #  Calculate the Background per Channel
            area_bg1_1 = y_bg1_1.sum()
            area_bg1_1_csv=[]
            area_bg1_1_csv.append(area_bg1_1)
            bgpc_1_1=area_bg1_1/(bg1_r_1-bg1_l_1+1)
            area_l = y1.sum()-(bgpc_1_1)*(ini_r_1-ini_l_1+1)
            area_l_csv=[]
            area_l_csv.append(area_l)
            print('Background1_1',bgpc_1_1,'Counts per Channel')
            # Save the Peak Area
            df_2[os.path.basename(name)[:-4]] = area_l_csv
            df_2_local[os.path.basename(name)[:-4]] = area_l_csv
            # Print Peak Area
            print ('areal','No.',count+1,':',area_l)
            # Record the number of file
            count = count + 1
            tcount = tcount + 1
            # Calculate the Mean and Std of all the data
            if count >= n:
               mean = df_2_local.mean(axis=1).values
               std = df_2_local.std(axis=1).values
               df_2[os.path.basename(name)[:-6] + "area_l Mean"] = mean
               df_2[os.path.basename(name)[:-6] + "area_l Dev"] = std
               df_2[os.path.basename(name)[:-6] + "area_l dp %"] = std/mean*100
            # Print the Mean and Std of all the data
               print ('area_l','Ave:',mean)
               print ('area_l','Std:',std)
               print ('area_l','%:',std/mean*100)
               count = 0

      except IOError as exc:
         if exc.errno != errno.EISDIR:
            raise
df_2.to_csv(path+'\\'+"area_l.CSV")
end = time.time()

print('Elapsed {} seconds'.format(end-start))
```

GEANT4 Simulation Code

PrimaryGeneratorAction.cc

```
#include "PrimaryGeneratorAction.hh"
#include "G4Event.hh"
#include "G4ParticleGun.hh"
#include "G4ParticleTable.hh"
#include "G4ParticleDefinition.hh"
#include "G4GeneralParticleSource.hh"
#include "G4SystemOfUnits.hh"
#include "Randomize.hh"

PrimaryGeneratorAction::PrimaryGeneratorAction()
: G4VUserPrimaryGeneratorAction(),
  fParticleGun(0)
{
   fParticleGun = new G4GeneralParticleSource();
}

PrimaryGeneratorAction::~PrimaryGeneratorAction()
{
   delete fParticleGun;
}

void PrimaryGeneratorAction::GeneratePrimaries(G4Event* event)
{
   fParticleGun->GeneratePrimaryVertex(event);
}
```

PhysicsList.cc

```
#include "PhysicsList.hh"
#include "G4DecayPhysics.hh"
#include "G4EmStandardPhysics.hh"
#include "G4RadioactiveDecayPhysics.hh"

PhysicsList::PhysicsList()
: G4VModularPhysicsList(){
  SetVerboseLevel(1);
  RegisterPhysics(new G4DecayPhysics());
  RegisterPhysics(new G4EmStandardPhysics());
  RegisterPhysics(new G4RadioactiveDecayPhysics());
}

PhysicsList::~PhysicsList()
{}

void PhysicsList::SetCuts()
{
  G4VUserPhysicsList::SetCuts();
}
```

EventAction.cc

```
#include "EventAction.hh"
#include "BeetleRunAction.hh"
```

```
#include "G4Event.hh"
#include "G4RunManager.hh"

EventAction::EventAction(BeetleRunAction* runAction)
: G4UserEventAction(),
  fRunAction(runAction)
{}

EventAction::~EventAction()
{}

void EventAction::BeginOfEventAction(const G4Event*)
{
}

void EventAction::EndOfEventAction(const G4Event*)
{
}
```

DetectorConstruction.cc

```
#include "DetectorConstruction.hh"
#include "G4FieldManager.hh"
#include "G4TransportationManager.hh"
#include "G4Mag_UsualEqRhs.hh"
#include "G4AutoDelete.hh"
#include "G4NistManager.hh"
#include "G4Box.hh"
#include "G4Tubs.hh"
#include "G4LogicalVolume.hh"
#include "G4PVPlacement.hh"
#include "G4PVParameterised.hh"
#include "G4PVReplica.hh"
#include "G4UserLimits.hh"
#include "G4SubtractionSolid.hh"
#include "G4SDManager.hh"
#include "G4VisAttributes.hh"
#include "G4Colour.hh"
#include "G4MultiFunctionalDetector.hh"
#include "G4PSPassageCellCurrent.hh"
#include "G4PSEnergyDeposit.hh"
#include "G4PSDoseDeposit.hh"
#include "G4PSPassageCellFlux.hh"
#include "G4PSSphereSurfaceCurrent.hh"
#include "G4PSFlatSurfaceCurrent.hh"
#include "G4VPrimitiveScorer.hh"
#include "G4SDParticleWithEnergyFilter.hh"
#include "G4PhysicalConstants.hh"
#include "G4ios.hh"
#include "G4SystemOfUnits.hh"

/********This part is the definition of dimensions, materials, and geometry of the detector
and the containers*******/

DetectorConstruction::DetectorConstruction()
: G4VUserDetectorConstruction(),
   fWorldLogical(0),
```

```
   fWorldPhysical(0),
   fDetectorLogical(0),
   fVisAttributes()
{}

DetectorConstruction::~DetectorConstruction()
{
///Delete all the visattributes
   for (G4int i=0; i<G4int(fVisAttributes.size()); ++i){
     delete fVisAttributes[i];
  }
}
G4VPhysicalVolume* DetectorConstruction::Construct()
{
   // Construct materials
   ConstructMaterials();
   G4Material* air = G4Material::GetMaterial("G4_AIR");
   G4Material* water = G4Material::GetMaterial("G4_WATER");
   G4Material* CdTe = G4Material::GetMaterial("G4_CADMIUM_TELLURIDE");
   G4Material* kaolinwater = G4Material::GetMaterial("KaolinWater");
   G4Material* Quartz = G4Material::GetMaterial("Quartz");
   G4Material* Polystyrene = G4Material::GetMaterial("Polystyrene");
   G4Material* fftwater = G4Material::GetMaterial("Fftwater");
   G4Material* Acrylic = G4Material::GetMaterial("Acrylic");
   G4Material* SiO2solution = G4Material::GetMaterial("SiO2solution");
   G4Material* Beryllium = G4Material::GetMaterial("Beryllium");

   G4bool checkOverlaps = true;

   G4ThreeVector worldSize = G4ThreeVector(300*mm, 300*mm, 300*mm);
   G4VSolid* worldSolid
     = new G4Box("world", worldSize.x()/2., worldSize.y()/2., worldSize.z()/2.);
   fWorldLogical
     = new G4LogicalVolume(worldSolid,air,"fWorldLogical");
   fWorldPhysical
     = new G4PVPlacement(0,G4ThreeVector(),fWorldLogical,"worldPhysical",0,
                   false,0,checkOverlaps);

// 1 cm Polystyrene Cuvette
   /*
      G4Box* outsideBox = new G4Box("outsideBox",6.25*mm, 22.5*mm, 6.25*mm);

      G4Box* insideBox  = new G4Box("insideBox", 5.*mm, 22.5*mm, 5.*mm);

      G4SubtractionSolid* cuvetteSolid
        = new G4SubtractionSolid("Hollow Box",outsideBox,insideBox);

      G4LogicalVolume* cuvetteLogical
        = new G4LogicalVolume(cuvetteSolid,Polystyrene,"cuvetteLogical");

      new G4PVPlacement(0,G4ThreeVector(),cuvetteLogical,
                   "cuvettePhysical",fWorldLogical,
                   false,0,checkOverlaps);
   */

// 43 mm Acrylic Container
```

```
    /*
    G4Box* outsideBox = new G4Box("outsideBox",24.5*mm, 50.*mm, 24.5*mm);
    G4Box* insideBox  = new G4Box("insideBox", 21.5*mm, 50.*mm, 21.5*mm );
    G4SubtractionSolid* cuvetteSolid
      = new G4SubtractionSolid("Hollow Box",outsideBox,insideBox);
    G4LogicalVolume* cuvetteLogical
      = new G4LogicalVolume(cuvetteSolid,Acrylic,"cuvetteLogical");
    new G4PVPlacement(0,G4ThreeVector(),cuvetteLogical,
                    "cuvettePhysical",fWorldLogical,
                    false,0,checkOverlaps);
    */

  // Sample Volume for 1 cm Polystyrene Cuvette
     /*
    G4ThreeVector sampleSize = G4ThreeVector(10.*mm, 45.*mm, 10.*mm);

    G4VSolid* sampleSolid
      = new G4Box("sample",sampleSize.x()/2., sampleSize.y()/2., sampleSize.z()/2.);

    G4LogicalVolume* sampleLogical
      = new G4LogicalVolume(sampleSolid,mftwater,"sampleLogical");

    new G4PVPlacement(0,G4ThreeVector(0, 0.*mm, 0.*mm),sampleLogical,
                    "samplePhysical",fWorldLogical,
                    false,0,checkOverlaps);
   */

  // Aluminum Sheets
     /*
    G4Box* LeftAluminumSheet
         = new G4Box("LeftAluminumSheet",28.*mm,22.5*mm,1.*mm);
    G4Box* RightAluminumSheet
         = new G4Box("RightAlluminumSheet",28.*mm,22.5*mm,1.*mm);
    */

  // Left Hole and Right Hole on the Sheets
     /*
    G4Tubs* LeftHole
      = new G4Tubs("LeftHole",0,4.*mm,2.*mm,0.*deg,360.*deg);
    G4Tubs* RightHole
      = new G4Tubs("RightHole",0,5.*mm,2.*mm,0.*deg,360.*deg);

    G4SubtractionSolid* LeftAlWithHoleSolid
      = new G4SubtractionSolid("LeftAlWithHole",LeftAluminumSheet,LeftHole);

    G4SubtractionSolid* RightAlWithHoleSolid
      = new G4SubtractionSolid("RightAlWithHole",RightAluminumSheet,RightHole);


    G4LogicalVolume* LeftWithHoleLogical
      = new G4LogicalVolume(LeftAlWithHoleSolid,Aluminum,"LeftAlWithHoleLogical");
    G4LogicalVolume* RightWithHoleLogical
      = new G4LogicalVolume(RightAlWithHoleSolid,Aluminum,"RightAlWithHoleLogical");

    new G4PVPlacement(0,G4ThreeVector(0, 0.*mm, -7.5*mm),LeftWithHoleLogical,
                    "LeftWithHolePhysical",fWorldLogical,
```

```
                false,0,checkOverlaps);

    new G4PVPlacement(0,G4ThreeVector(0, 0.*mm, 7.5*mm),RightWithHoleLogical,
                "LeftWithHolePhysical",fWorldLogical,
                false,0,checkOverlaps);
       */

// Block for Making a Slot
    /*
    G4Box* UpperBlock
        = new G4Box("UpperBlock",10.75*mm,22.5*mm,6.5*mm);
    G4LogicalVolume* UpperBlockLogical
        = new G4LogicalVolume(UpperBlock,Aluminum,"UpperBlockLogical");
       new G4PVPlacement(0,G4ThreeVector(17.25*mm,0,0),UpperBlockLogical,
                  "UpperBlockPhysical",fWorldLogical,
                  false,0,checkOverlaps);
    */

// Sample Volume for 43 mm Acrylic Container
    /*
    G4ThreeVector sampleSize = G4ThreeVector(43.*mm,90.*mm, 43.*mm);
    G4VSolid* sampleSolid
      = new G4Box("sample",sampleSize.x()/2., sampleSize.y()/2., sampleSize.z()/2.);
    G4LogicalVolume* sampleLogical
      = new G4LogicalVolume(sampleSolid,kaolinwater,"sampleLogical");
    new G4PVPlacement(0,G4ThreeVector(0, -5.*mm, 0.*mm),sampleLogical,
                "samplePhysical",fWorldLogical,
                false,0,checkOverlaps);
    */

// Beryllium Window
    G4VSolid* BeWindowSolid
      = new G4Tubs("BeWindowSolid",0,6.985*mm,0.1*mm,0.*deg,360.*deg);
    G4LogicalVolume* BeWindowLogical
      = new G4LogicalVolume(BeWindowSolid,Beryllium,"BeWindowLogical");
    new G4PVPlacement(0,G4ThreeVector(0,-5.*mm,32.05*mm),BeWindowLogical,
                "BeWindowPhysical",fWorldLogical,
                false,0,checkOverlaps);

// Detector Element
    G4VSolid* detectorSolid
      = new G4Box("detectorBox",1.5*mm, 1.5*mm, 0.5*mm);
    fDetectorLogical
      = new G4LogicalVolume(detectorSolid,CdTe,"DetectorLogical");
    new G4PVPlacement(0,G4ThreeVector(0, -5.*mm, 32.7*mm),fDetectorLogical,
                "DetectorPhysical",fWorldLogical,
                false,0,checkOverlaps);

    ConstructSDandField();

// Line Color for Visualization for 43 mm Container Setup
    /*
    G4VisAttributes* visAttributes = new G4VisAttributes(G4Colour(1.0,1.0,1.0));
       visAttributes->SetVisibility(false);
       fWorldLogical->SetVisAttributes(visAttributes);
       fVisAttributes.push_back(visAttributes);
```

```
        visAttributes = new G4VisAttributes(G4Colour(0.9,0.9,0.0));
        fDetectorLogical->SetVisAttributes(visAttributes);
        fVisAttributes.push_back(visAttributes);

        G4Colour blue(0.,0.,0.8888);
        G4VisAttributes attribs2(blue);
        sampleLogical->SetVisAttributes(attribs2);

        G4Colour clay(0.,1.0,1.0);
        G4VisAttributes attribs3(clay);
        cuvetteLogical->SetVisAttributes(attribs3);

        G4Colour red(0.,1.0,1.0);
        G4VisAttributes attribs4(red);
        LeftWithHoleLogical->SetVisAttributes(attribs4);

        G4VisAttributes attribs5(red);
        RightWithHoleLogical->SetVisAttributes(attribs5);

        //G4VisAttributes attribs6(red);
        //BeWindowLogical->SetVisAttributes(attribs6);

        return fWorldPhysical;
    */

// Line Color for Visualization for 1 cm Cuvette Setup
    /*
    G4VisAttributes* visAttributes = new G4VisAttributes(G4Colour(1.0,1.0,1.0));
    visAttributes->SetVisibility(false);
    fWorldLogical->SetVisAttributes(visAttributes);
    fVisAttributes.push_back(visAttributes);

    visAttributes = new G4VisAttributes(G4Colour(0.9,0.9,0.0));
    fDetectorLogical->SetVisAttributes(visAttributes);
    fVisAttributes.push_back(visAttributes);

    G4Colour blue(0.,0.,0.8888);
    G4VisAttributes attribs2(blue);
    sampleLogical->SetVisAttributes(attribs2);

    G4Colour clay(0.,1.0,1.0);
    G4VisAttributes attribs3(clay);
    cuvetteLogical->SetVisAttributes(attribs3);

    return fWorldPhysical;
    */
}
        /**************This part is the definition of energy scale of the output spectra************/

// Spectra energy scale for 241Am
/*
void DetectorConstruction::ConstructSDandField()
{
  G4MultiFunctionalDetector* mFDet
     = new G4MultiFunctionalDetector("MyDetector");
```

```
  G4SDManager* manager = G4SDManager::GetSDMpointer();
   manager->AddNewDetector(mFDet);
   fDetectorLogical->SetSensitiveDetector(mFDet);
  G4int nEnergyBins = 1024;
  G4int i(0);
  for (i=0; i<nEnergyBins; i++){
    char name[17];
    std::sprintf(name,"MyScorer%i", i);
    G4PSFlatSurfaceCurrent* MyScorer
      = new G4PSFlatSurfaceCurrent(name,1);
  //create a filter
    G4SDParticleWithEnergyFilter* filter
      = new G4SDParticleWithEnergyFilter("GammaFilter");
    G4double minEnergy = (i*0.065931-0.5984747)*keV;
    G4double maxEnergy = (i*0.065931-0.5325437)*keV;
    filter->add("gamma");
    filter->SetKineticEnergy(minEnergy, maxEnergy);
    MyScorer->SetFilter(filter);
    MyScorer->DivideByArea(false);
    //G4cout<<"Created scorer with name "<<name;
    //G4cout<<", covering energy range "<<minEnergy*MeV;
    //G4cout<<" : "<<maxEnergy*MeV<<"MeV"<<G4endl;
    mFDet->RegisterPrimitive(MyScorer);
  }
 }
 */

 // Spectra energy scale for 133Ba
 /*
 void DetectorConstruction::ConstructSDandField()
 {
  G4MultiFunctionalDetector* mFDet
     = new G4MultiFunctionalDetector("MyDetector");
  G4SDManager* manager = G4SDManager::GetSDMpointer();
   manager->AddNewDetector(mFDet);
   fDetectorLogical->SetSensitiveDetector(mFDet);
  G4int nEnergyBins = 1024;
  G4int i(0);
  for (i=0; i<nEnergyBins; i++){
    char name[17];
    std::sprintf(name,"MyScorer%i", i);
    G4PSFlatSurfaceCurrent* MyScorer
      = new G4PSFlatSurfaceCurrent(name,1);
    G4SDParticleWithEnergyFilter* filter
      = new G4SDParticleWithEnergyFilter("GammaFilter");
    G4double minEnergy = (i*0.135781-1.826690)*keV;
    G4double maxEnergy = (i*0.135781-1.690909)*keV;
    filter->add("gamma");
    filter->SetKineticEnergy(minEnergy, maxEnergy);
    MyScorer->SetFilter(filter);
    MyScorer->DivideByArea(false);
    mFDet->RegisterPrimitive(MyScorer);
  }
 }
 */
```

```
        /********This part is the definition of elements that is possible used in the simualtion*******/
void DetectorConstruction::ConstructMaterials()
{
  G4NistManager* nistManager = G4NistManager::Instance();
     nistManager->FindOrBuildMaterial("G4_AIR");
     nistManager->FindOrBuildMaterial("G4_WATER");
     nistManager->FindOrBuildMaterial("G4_CADMIUM_TELLURIDE");

  G4String symbol,name;
  G4double z,a;
  G4double density;
  G4int ncomponents;
  G4double fractionmass;
  G4int nel, natoms;

  G4Element* N = new G4Element("Nitrogen", symbol="N", z=7., a=14.01*g/mole);
  G4Element* O = new G4Element("Oxygen",   symbol="O", z=8., a=16.00*g/mole);
  G4Element* C = new G4Element("Carbon",   symbol="C", z=6., a=12.011*g/mole);
  G4Element* H = new G4Element("Hydrogen",  symbol="H", z=1., a=1.00795*g/mole);
  G4Element* Si = new G4Element("Silicon",   symbol="Si", z=14., a=28.09*g/mole);
  G4Element* Al = new G4Element("Aluminum",  symbol="Al", z=13., a=26.98*g/mole);
  G4Element* Fe = new G4Element("Iron",  symbol="Fe", z=26., a=55.845*g/mole);
  G4Element* Ca = new G4Element("Calcium", symbol="Ca", z=20., a=40.078*g/mole);
  G4Element* K = new G4Element("Kalium",  symbol="K", z=19., a=39.0983*g/mole);
  G4Element* Ti = new G4Element("Titanium",  symbol="Ti", z=22., a=47.867*g/mole);
  G4Element* Mg = new G4Element("Magnesium",  symbol="Mg", z=12., a=24.305*g/mole);

  new G4Material("liquidArgon", z=18., a= 39.95*g/mole, density= 1.390*g/cm3);
  new G4Material("Carbon"     , z=6.,  a= 12.01*g/mole, density= 2.267*g/cm3);
  new G4Material("Aluminium"  , z=13., a= 26.98*g/mole, density= 2.700*g/cm3);
  new G4Material("Silicon"    , z=14., a= 28.09*g/mole, density= 2.330*g/cm3);
  new G4Material("Germanium"  , z=32., a= 72.61*g/mole, density= 5.323*g/cm3);
  new G4Material("Beryllium"  , z=5., a= 9.01*g/mole, density= 1.85*g/cm3);

// Chemical Compositions of NRCAN kaolin ICP-MS results, Upper and lower limit; G90 kaolin ICP-MS
Results, Upper and lower limit; Calculated by using kaolin formula; Calculated by using FFT-1 formula.
  //FFT
   G4double FFTwt = 0.4; //0.1;0.2;0.3;0.4
   G4double FFTdensity;
   FFTdensity = 1.281;//1.056,1.133,1.200,1.281

   G4Material* fftwater = new G4Material("FFtwater", density= FFTdensity*g/cm3, ncomponents=9);

   // FFT-1 ICP-MS Results); // Upper Limit); // Lower Limit);
   /*
   fftwater->AddElement(Al, fractionmass = FFTwt*0.105178);//0.110093);//0.100263);
   fftwater->AddElement(Si, fractionmass = FFTwt*0.254928);//0.262017);//0.247839);
   fftwater->AddElement(Fe, fractionmass = FFTwt*0.0186135);//0.0196072);//0.0176198);
   fftwater->AddElement(Ca, fractionmass = FFTwt*0.00731621);//0.00987432);//0.00475810);
   fftwater->AddElement(K, fractionmass = FFTwt*0.0195710);//0.0206316);//0.0185104);
   fftwater->AddElement(Ti, fractionmass = FFTwt*0.00438089);//0.00473067);//0.00403111);
   fftwater->AddElement(Mg, fractionmass = FFTwt*0.00534096);//0.00569402);//0.00498790);
   fftwater->AddElement(H, fractionmass = FFTwt*0.0159260+(1-FFTwt)*0.112);//0.0154541+(1-
FFTwt)*0.112);//0.0163976+(1-FFTwt)*0.112);
   fftwater->AddElement(O, fractionmass = FFTwt*0.568746+(1-FFTwt)*0.888);//0.551898+(1-
FFTwt)*0.888);//0.585593+(1-FFTwt)*0.888);
```

```
  */

  //Kaolin Density

  G4double kaolinwt = 0.4; //kaolin mass fraction
  G4double kwdensity;
  kwdensity = 1.332;
  // NRCAN measured density 1.065,1.148,1.236,1.310
  // Calculated kaolin 1.066,1.142,1.230,1.332
  //G90 kaolin (Measured): 1.059;1.145;1.224;1.319
  //FFT-1 (Measured):1.056,1.133,1.200,1.281

  G4Material* kaolinwater = new G4Material("KaolinWater", density= kwdensity*g/cm3,
ncomponents=4);

  // NRCAN kaolin ICP-MS Results
  /*
  kaolinwater->AddElement(Al, fractionmass = kaolinwt*0.220803);
  kaolinwater->AddElement(Si, fractionmass = kaolinwt*0.233973);
  kaolinwater->AddElement(Fe, fractionmass = kaolinwt*0.00520250);
  kaolinwater->AddElement(Ca, fractionmass = kaolinwt*0.00396126);
  kaolinwater->AddElement(K, fractionmass = kaolinwt*0.00410898);
  kaolinwater->AddElement(Ti, fractionmass = kaolinwt*0.00212448);
  kaolinwater->AddElement(Mg, fractionmass = kaolinwt*0.00115035);
  kaolinwater->AddElement(H, fractionmass = kaolinwt*0.0115365+(1-kaolinwt)*0.112);
  kaolinwater->AddElement(O, fractionmass = kaolinwt*0.413349+(1-kaolinwt)*0.888);
  */

  // Kaolin Calculated Formula
  /*
  kaolinwater->AddElement(Al, fractionmass = kaolinwt*0.209029);
  kaolinwater->AddElement(Si, fractionmass = kaolinwt*0.217582);
  kaolinwater->AddElement(H, fractionmass = kaolinwt*0.0156185+(1-kaolinwt)*0.112);
  kaolinwater->AddElement(O, fractionmass = kaolinwt*0.557770+(1-kaolinwt)*0.888);
  */

  // Illite Calculated Formula
  /*
  kaolinwater->AddElement(Al, fractionmass = kaolinwt*0.229734);
  kaolinwater->AddElement(Si, fractionmass = kaolinwt*0.159423);
  kaolinwater->AddElement(Fe, fractionmass = kaolinwt*0.158501);
  kaolinwater->AddElement(K, fractionmass = kaolinwt*0.0554844);
  kaolinwater->AddElement(Mg, fractionmass = kaolinwt*0.0689830);
  kaolinwater->AddElement(H, fractionmass = kaolinwt*0.0100133+(1-kaolinwt)*0.112);
  kaolinwater->AddElement(O, fractionmass = kaolinwt*0.317861+(1-kaolinwt)*0.888);
  */

  // G90 kaolin ICP-MS Results); // Upper Limit); // Lower Limit);
/*
  kaolinwater->AddElement(Al, fractionmass = kaolinwt*0.202974);//0.193489;//0.212458;);
  kaolinwater->AddElement(Si, fractionmass = kaolinwt*0.220959);//0.214814;//0.227104);
  kaolinwater->AddElement(Fe, fractionmass = kaolinwt*0.00651316);//0.00686086);//0.00616546);
  kaolinwater->AddElement(Ca, fractionmass = kaolinwt*0.00264105);//0.00356449);//0.00171761);
  kaolinwater->AddElement(K, fractionmass = kaolinwt*0.00130686);//0.00137768);//0.00123604);
  kaolinwater->AddElement(Ti, fractionmass = kaolinwt*0.00408370);//0.00440975);//0.00375765);
  kaolinwater->AddElement(Mg, fractionmass = kaolinwt*0.000217410);//0.000231781);//0.000203037);
```

```
  kaolinwater->AddElement(H, fractionmass = kaolinwt*0.0152894+(1-kaolinwt)*0.112);//0.0148179+(1-
kaolinwt)*0.112);//0.0157609+(1-kaolinwt)*0.112);
  kaolinwater->AddElement(O, fractionmass = kaolinwt*0.561305+(1-kaolinwt)*0.888);//0.543994+(1-
kaolinwt)*0.888);// 0.578617+(1-kaolinwt)*0.888);
 */

  //Polystyrene
  G4double PSdensity = 1.032;
  G4Material* Polystyrene = new G4Material("Polystyrene", density= PSdensity*g/cm3, nel=2);
  Polystyrene->AddElement(C, natoms=8);
  Polystyrene->AddElement(H, natoms=8);

  //Arcrylic
  G4Material* Acrylic = new G4Material("Acrylic",density= 1.18*g/cm3, ncomponents=3);
       Acrylic->AddElement(C, natoms=5);
       Acrylic->AddElement(H, natoms=8);
       Acrylic->AddElement(O, natoms=2);
  //Quartz
  G4Material* Quartz = new G4Material("Quartz",density= 2.32*g/cm3, ncomponents=2);
            Quartz->AddElement(Si, natoms=1);
            Quartz->AddElement(O , natoms=2);

  G4cout << G4endl << "The materials are : " << G4endl << G4endl;
  G4cout << *(G4Material::GetMaterialTable()) << G4endl;
}
```

STM32F334R8T6 Code (Automatically generated by using STM32CubeIDE with key parameters)

main.c

```
#include "main.h"
#include <stdio.h>
#ifdef __GNUC__
#define PUTCHAR_PROTOTYPE int __io_putchar(int ch)
#else
#define PUTCHAR_PROTOTYPE int fputc(int ch, FILE *f)
#endif
PUTCHAR_PROTOTYPE
{
HAL_USART_Transmit(&husart1, (uint8_t *)&ch, 1, 0xFFFF);
return ch;
}
void SystemClock_Config(void);
static void MX_GPIO_Init(void);
static void MX_ADC1_Init(void);
static void MX_USART1_Init(void);
uint32_t ADC_SUM, ADC_DATA,t_count;
int main(void)
{
 /* Reset of all peripherals, Initializes the Flash interface and the Systick.*/
 HAL_Init();
 /* Configure the system clock */
 SystemClock_Config();
 /* Initialize all configured peripherals */
```

```
  MX_GPIO_Init();
  MX_ADC1_Init();
  MX_USART1_Init();

  HAL_ADC_Start(&hadc1);
  HAL_ADC_PollForConversion(&hadc1, 0);
while(HAL_IS_BIT_SET(HAL_ADC_GetState(&hadc1),HAL_ADC_STATE_REG_EOC))
            {
                        ADC_DATA=HAL_ADC_GetValue(&hadc1);
                              if (ADC_DATA>0){
                                 ADC_SUM += ADC_DATA;
                              }else if(ADC_SUM>0){
                                 printf("%ld\n",ADC_SUM);
                                       ADC_SUM = 0;
                              }
}
}
/**
  * @brief System Clock Configuration
void SystemClock_Config(void)
{
  RCC_OscInitTypeDef RCC_OscInitStruct = {0};
  RCC_ClkInitTypeDef RCC_ClkInitStruct = {0};
  RCC_PeriphCLKInitTypeDef PeriphClkInit = {0};
  /** Initializes the CPU, AHB and APB busses clocks
  */
  RCC_OscInitStruct.OscillatorType = RCC_OSCILLATORTYPE_HSI;
  RCC_OscInitStruct.HSIState = RCC_HSI_ON;
  RCC_OscInitStruct.HSICalibrationValue = RCC_HSICALIBRATION_DEFAULT;
  RCC_OscInitStruct.PLL.PLLState = RCC_PLL_ON;
  RCC_OscInitStruct.PLL.PLLSource = RCC_PLLSOURCE_HSI;
  RCC_OscInitStruct.PLL.PLLMUL = RCC_PLL_MUL16;
  if (HAL_RCC_OscConfig(&RCC_OscInitStruct) != HAL_OK)
  {
    Error_Handler();
  }
  /** Initializes the CPU, AHB and APB busses clocks
  */
  RCC_ClkInitStruct.ClockType = RCC_CLOCKTYPE_HCLK|RCC_CLOCKTYPE_SYSCLK
                              |RCC_CLOCKTYPE_PCLK1|RCC_CLOCKTYPE_PCLK2;
  RCC_ClkInitStruct.SYSCLKSource = RCC_SYSCLKSOURCE_PLLCLK;
  RCC_ClkInitStruct.AHBCLKDivider = RCC_SYSCLK_DIV1;
  RCC_ClkInitStruct.APB1CLKDivider = RCC_HCLK_DIV2;
  RCC_ClkInitStruct.APB2CLKDivider = RCC_HCLK_DIV1;
  if (HAL_RCC_ClockConfig(&RCC_ClkInitStruct, FLASH_LATENCY_2) != HAL_OK)
  {
    Error_Handler();
  }
  PeriphClkInit.PeriphClockSelection = RCC_PERIPHCLK_USART1|RCC_PERIPHCLK_ADC12;
  PeriphClkInit.Usart1ClockSelection = RCC_USART1CLKSOURCE_PCLK1;
  PeriphClkInit.Adc12ClockSelection = RCC_ADC12PLLCLK_DIV1;
  if (HAL_RCCEx_PeriphCLKConfig(&PeriphClkInit) != HAL_OK)
  {
    Error_Handler();
  }
}
```

```
/**
  * @brief ADC1 Initialization Function
  */
static void MX_ADC1_Init(void)
{
  ADC_MultiModeTypeDef multimode = {0};
  ADC_ChannelConfTypeDef sConfig = {0};
  /** Common config
  */
  hadc1.Instance = ADC1;
  hadc1.Init.ClockPrescaler = ADC_CLOCK_ASYNC_DIV1;
  hadc1.Init.Resolution = ADC_RESOLUTION_12B;
  hadc1.Init.ScanConvMode = ADC_SCAN_DISABLE;
  hadc1.Init.ContinuousConvMode = ENABLE;
  hadc1.Init.DiscontinuousConvMode = DISABLE;
  hadc1.Init.ExternalTrigConvEdge = ADC_EXTERNALTRIGCONVEDGE_NONE;
  hadc1.Init.ExternalTrigConv = ADC_SOFTWARE_START;
  hadc1.Init.DataAlign = ADC_DATAALIGN_RIGHT;
  hadc1.Init.NbrOfConversion = 1;
  hadc1.Init.DMAContinuousRequests = DISABLE;
  hadc1.Init.EOCSelection = ADC_EOC_SINGLE_CONV;
  hadc1.Init.LowPowerAutoWait = DISABLE;
  hadc1.Init.Overrun = ADC_OVR_DATA_PRESERVED;
  if (HAL_ADC_Init(&hadc1) != HAL_OK)
  {
    Error_Handler();
  }
  /** Configure the ADC multi-mode
  */
  multimode.Mode = ADC_MODE_INDEPENDENT;
  if (HAL_ADCEx_MultiModeConfigChannel(&hadc1, &multimode) != HAL_OK)
  {
    Error_Handler();
  }
  /** Configure Regular Channel
  */
  sConfig.Channel = ADC_CHANNEL_12;
  sConfig.Rank = ADC_REGULAR_RANK_1;
  sConfig.SingleDiff = ADC_SINGLE_ENDED;
  sConfig.SamplingTime = ADC_SAMPLETIME_1CYCLE_5;
  sConfig.OffsetNumber = ADC_OFFSET_NONE;
  sConfig.Offset = 0;
  if (HAL_ADC_ConfigChannel(&hadc1, &sConfig) != HAL_OK)
  {
    Error_Handler();
  }
}
/**
  * @brief USART1 Initialization Function
static void MX_USART1_Init(void)
{
  husart1.Instance = USART1;
  husart1.Init.BaudRate = 256000;
  husart1.Init.WordLength = USART_WORDLENGTH_8B;
  husart1.Init.StopBits = USART_STOPBITS_1;
  husart1.Init.Parity = USART_PARITY_NONE;
```

```
  husart1.Init.Mode = USART_MODE_TX_RX;
  husart1.Init.CLKPolarity = USART_POLARITY_LOW;
  husart1.Init.CLKPhase = USART_PHASE_1EDGE;
  husart1.Init.CLKLastBit = USART_LASTBIT_DISABLE;
  if (HAL_USART_Init(&husart1) != HAL_OK)
  {
    Error_Handler();
  }
}
static void MX_GPIO_Init(void)
{
  GPIO_InitTypeDef GPIO_InitStruct = {0};
  /* GPIO Ports Clock Enable */
  __HAL_RCC_GPIOC_CLK_ENABLE();
  __HAL_RCC_GPIOF_CLK_ENABLE();
  __HAL_RCC_GPIOA_CLK_ENABLE();
  __HAL_RCC_GPIOB_CLK_ENABLE();
  /*Configure GPIO pin Output Level */
  HAL_GPIO_WritePin(LD2_GPIO_Port, LD2_Pin, GPIO_PIN_RESET);
  /*Configure GPIO pin : B1_Pin */
  GPIO_InitStruct.Pin = B1_Pin;
  GPIO_InitStruct.Mode = GPIO_MODE_IT_FALLING;
  GPIO_InitStruct.Pull = GPIO_NOPULL;
  HAL_GPIO_Init(B1_GPIO_Port, &GPIO_InitStruct);
  /*Configure GPIO pins : USART_TX_Pin USART_RX_Pin */
  GPIO_InitStruct.Pin = USART_TX_Pin|USART_RX_Pin;
  GPIO_InitStruct.Mode = GPIO_MODE_AF_PP;
  GPIO_InitStruct.Pull = GPIO_NOPULL;
  GPIO_InitStruct.Speed = GPIO_SPEED_FREQ_HIGH;
  GPIO_InitStruct.Alternate = GPIO_AF7_USART2;
  HAL_GPIO_Init(GPIOA, &GPIO_InitStruct);
  /*Configure GPIO pin : LD2_Pin */
  GPIO_InitStruct.Pin = LD2_Pin;
  GPIO_InitStruct.Mode = GPIO_MODE_OUTPUT_PP;
  GPIO_InitStruct.Pull = GPIO_NOPULL;
  GPIO_InitStruct.Speed = GPIO_SPEED_FREQ_LOW;
  HAL_GPIO_Init(LD2_GPIO_Port, &GPIO_InitStruct);
}
void Error_Handler(void)
{
}
#ifdef  USE_FULL_ASSERT
void assert_failed(char *file, uint32_t line)
{
}
#endif /* USE_FULL_ASSERT */
```